ISRSSP 2014

Fourth International Symposium on Radio Systems and Space Plasma

Proceedings

Ruse, Bulgaria, 30-31 October 2014

Organized by

Under the auspices of

Cooperating Organizations

ISRSSP 2014

Proceedings of the
Fourth International Symposium on
Radio Systems and Space Plasma

Ruse, Bulgaria
30-31 October 2014

Organized by
IICREST - Interdisciplinary Institute for Collaboration and Research on Enterprise Systems and Technology

In Cooperation with
AUTH - Aristotle University of Thessaloniki
AMAKOTA Ltd.

Under the Auspices of
URSI - International Union of Radio Science

Edited by Blagovest Shishkov

Graphics Production by Canka Petrova

Printed in Bulgaria

ISBN: 978-619-90124-2-0

http://www.isrssp.org

secretariat@iicrest.org

Sofia 2014

BRIEF CONTENTS

KEYNOTE SPEAKER

Andon Lazarov

Burgas Free University

Bulgaria

CHAIR AND PROGRAM COMMITTEE

Symposium Committee

Chair

Blagovest Shishkov, Bulgarian Academy of Sciences, Bulgaria

PROGRAM COMMITTEE

Jorgen Bach ANDERSEN, Aalborg University, Denmark

A.K.M. BAKI, Independent University of Bangladesh, Bangladesh

Maurice BELLANGER, CNAM, France

Jun CHENG, Doshisha University, Japan

Damyan DAMYANOV, Technical University - Sofia, Bulgaria

Peter DAVIS, ATR, Kyoto, Japan

Filip FILIPOV, Technical University - Sofia, Bulgaria

Hristo KABAKCHIEV, Sofia University St. Kliment Ohridski, Bulgaria

Pierre KAUFMANN, Mackenzie Presbyterian University, Brazil

Hirotsugu KOJIMA, Kyoto University, Japan

Andon LAZAROV, Burgas Free University, Bulgaria

François LEFEUVRE, LPCE/CNRS, France

Frank LITTLE, Texas A & M University, USA

Vladimir LYUBCHENKO, Russian Academy of Sciences, Russia

Marin NENCHEV, Technical University - Sofia, Bulgaria

Yoshiharu OMURA, Kyoto University, Japan

Petko PETKOV, Technical University - Sofia, Bulgaria

Michel PARROT, LPCE/CNRS, France

Bodo REINISCH, University of Massachusetts - Lowell, USA

PROGRAM COMMITTEE (CONT.)

Michael RUDERMAN, University of Sheffield, UK

Tapan SARKAR, Syracuse University, US

Naoki SHINOHARA, Kyoto University, Japan

Alexander SHMELEV, Radiotechnical Institute, Moscow, Russia

Angela SLAVOVA, BAS, Bulgaria

Tadashi TAKANO, Nihon University, Japan

Hideyuki USUI, Kobe University, Japan

Madalina VLAD, Association EURATOM/MEdC, Romania

Andrzej WERNIK, Polish Academy of Sciences, Poland

BEST PAPERS SELECTION

The authors of around two selected papers presented at ISRSSP `14
will have the privilege to submit invited papers to a special session of
ICTRS 2015 - the Fourth International Conference on
Telecommunications and Remote Sensing

FOREWORD

We warmly welcome you to ISRSSP 2014 – the Fourth International Symposium on Radio Systems and Space Plasma, held in Ruse, Bulgaria on 30–31 October 2014.

The symposium has been organized by the Interdisciplinary Institute for Collaboration and Research on Enterprise Systems and Technology (IICREST) under the auspices of the International Union of Radio Science (URSI), in cooperation with Aristotle University of Thessaloniki and AMAKOTA Ltd

The Proceedings of ISRSSP 2014 consists of 7 selected research and experience papers that have not been published previously, including the paper of the Keynote Speaker.

The symposium is focusing on Radio Systems and Space Plasma, considering the following research areas:

(i) Radio Communication Systems and Signal Processing;
(ii) Satellite Space Observations;
(iii) Trans-Ionospheric Propagation;
(iv) Space Plasma, Waves, and Particles;
(v) Solar Power Satellite (SPS) Systems,

as announced in the ISRSSP"14 Call for Papers. These areas are relevant to the work in several URSI Commissions, namely: Commission C- (i), Commission G – (ii), Commission F (iii) and Commission H(iv).The papers in the current proceedings are mainly in the areas (i), (ii), (iii) and (v).

We are inspired to go forward with this event, contributing to the dissemination of radio science -related knowledge.

With regard to ISRSSP'14, the quality of the program is enhanced by the Keynote Lecture, delivered by Prof. Dr. Andon Lazarov, who is an outstanding representative of the Bulgarian URSI Community as well as by informal discussions complementing the paper presentations. It is seen as well that since the start in 2007 well until now, we have been successful in establishing a small but focused community of experienced researchers and practitioners who are inspiring the ISRSSP developments.

Further, the authors of around two selected papers presented at ISRSSP `14 will have the privilege to submit invited papers to a special session of ICTRS 2015 - the Fourth International Conference on Telecommunications and Remote Sensing (www.ictrs.org)

Building a successful program for the symposium required the dedicated efforts of many people. We would like to express our thanks, first of all, to the authors of the technical papers presented of the symposium. Next, we would like to thank all the members of the Program Committee and reviewers, who helped us with their expertise, dedication and time.

FOREWORD (CONT.)

Furthermore, special thanks to IICREST and AMAKOTA for taking care of the organization. Naturally, words of appreciation for the work of the secretariat whose diligence and patience are to be mentioned.

We wish you an inspiring symposium and enjoyable stay in the beautiful city of Ruse. We look forward to seeing you at the Fifth International Symposium on Radio Systems and Space Plasma, details of which will be made available at http://www.isrssp.org

Blagovest Shishkov
Bulgarian Academy of Sciences
President of Bulgarian URSI Committee
Chair of ICTRS 2014

CONTENTS

KEYNOTE SPEAKER

BISTATIC SAR SISTEMS WITH GPS AND DVB-S ASTRA TRSNSMITTERS OF OPPORTUNITY

Andon Lazarov
Burgas Free University, San Stefano Str. 62, Burgas Bulgaria
lazarov@bfu.bg

Keywords: Bistatic SAR, GPS and DVB-S transmitters of opportunity, BSAR image reconstruction algorithms.

Abstract: Orbital parameters and radio emission's signal structure of space-based carriers as communication satellite system Astra and global positioning and navigation systems and their application in BSAR system with non cooperative transmitter are described. The orbital parameters of potential targets as ballistic missiles are presented. The structure of GPS waveforms as C/A and P phase codes and DVB-T OFDM waveform as a model of DVB-S signal is discussed. BSAR geometry and signal models, basic analytical equations of image reconstruction algorithm, illustrated with results of numerical experiments are also presented. The application of compressed sensing approach to remove frequency gabs in DVB-T signal and improve range resolution of the DVB-T BSAR image is illustrated. Field experiments conducted by the team from Birmingham University are shown. The results illustrate functional capabilities of BSAR system with space-based transmitter of opportunity to detect and recognize stationary target, placed on the earth.

1 INTRODUCTION

Synthetic Aperture Radar (SAR) and Inverse Synthetic Aperture Radar (SAR) are coherent instruments for target imaging. SAR utilizes movement of the radar carrier while ISAR utilizes displacement of the target in order to realize azimuth resolution. To realize a high range resolution both of systems use signals with wide bandwidth. In case the radar carrier and target are moving simultaneously it can be referred to as Generalized ISAR (GISAR) system.

If the transmitter and receiver are placed on different position the system can be referred to bistatic radar instruments (Whitewood, 2007). In case one or both of transmitter and receiver are moving the system can be referred to Bistatic Synthetic Aperture Radar (BSAR). If the target is moving the system can be regarded as Bistatic Inverse Synthetic Aperture Radar (BISAR). In case the object is on or close to the line "transmitter-receiver" it can be referred to Forward Scattering Synthetic Aperture Radar (FSAR).

In the space there exist many satellites with radio emission with different applications as communications, navigations, radio broadcasting and TV retransmission. The emitted signals of these systems can be employed for monitoring and imaging objects by applying SAR methods and algorithm. It can help reducing the complexity and cost of observation and implement secrecy of observation. Bistatic SAR systems with space-based transmitters of opportunity can be used to detect stationary and moving objects in the Space, Air and on Earth surface.

The aim of this study is survey and analysis of all components, signals and imaging algorithms of BSAR system with satellite-based transmitters of opportunity, and to illustrate its functionality trough numerical and real experimental results. The paper is organized as follows. In Section 2 orbital and signal parameters of Astra communications satellite and GNSS satellites are presented. In section 3 BSAR geometry satellite transmitter's waveforms, signal models and image reconstruction algorithms are illustrated. In section 4 results from field

experiments conducted by the team of Prof. M. Cherniakov from Birmingham University are presented and discussed. In section 5 conclusions are made.

2 BSAR SATELLITE BASED TRANASMITTERS OF OPPORTUNITY

There exist different types of BSAR topologies in dependence on satellite carriers of transmitters of opportunity, position and carriers of the receiver and type and kinematics of the objects. The BSAR topology includes Global Positioning system (GPS), Global Navigation Satellite Systems (GNSS), or communication DVB-S satellite system as transmitter of opportunity, moving or stationary target and a receiver placed on the ground or on a board of flying carrier (Fig. 1) (Cherniakov, 2007).

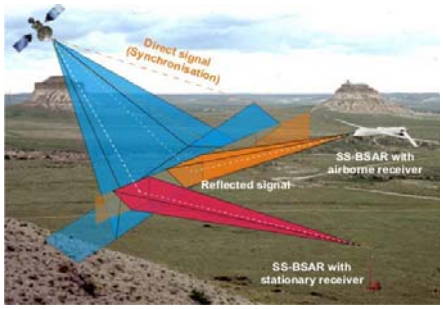

Figure 1: This BSAR scenario with satellite transmitter of opportunity and receivers placed on the earth and UMA vehicle.

2.1 Astra Communication System

Astra is a system of communications satellites that provides digital television (DVB-S), DTH (Direct-To-Home) telecast, cable, multimedia and interactive services, and corporate networks to central Europe. The satellite provides two broadcast beams, of horizontal and vertical polarization, across two footprints that covered essentially the same areas of Europe – principally the countries of central Europe.

Astra orbital parameters: Reference system: Geocentric reference system, geostationary regime of movement: Longitude 23.5° East; Perigee 35,771 km; Apogee 35,811 km; Inclination 0.06 degrees; Period 1436.03 min. Footprint of Astra 3B satellite system is presented in Fig.2 (https://es.ses-astra.com/18579930/3A-footprint-fact-sheet.pdf).

Transponders: Band 52 K_U band, 4 K_A band; Bandwidth 33/36 MHz; Traveling Wave Tube Amplifiers (TWTA) power: 140 W; Equivalent Isotropic Radiated Power (EIRP): 52 dBW.

Geostationary regime of functionality guaranties all time availability of the Astra satellite on the area of interest and application of BISAR principle for imaging of moving targets.

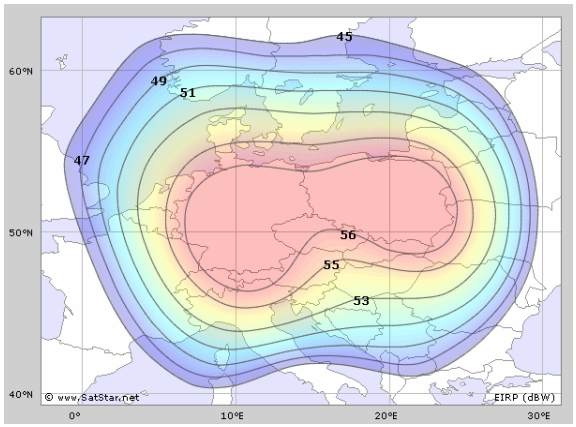

Figure 2: Footprint of Astra-3B satellite transmitting antenna system.

Geostationary regime of functionality guaranties all time availability of the Astra satellite on the area of interest and application of BISAR principle for imaging of moving targets.

2.1.1 Structure of DVB-S Signals

There are two satellite standards: DVB-S and DVB-S2. The original DVB-S system specifies the use of QPSK modulation along with various tools for channel error correction coding. Further additions were made with the emergence of DVB-DSNG (Digital Satellite News Gathering), for example allowing the use of 8PSK and 16QAM modulation. DVB-S2 is a digital satellite transmission system of second generation using latest modulation and coding techniques. DVB-S2 has four modulation modes: QPSK, 8PSK, 16APSK and 32APSK; FEC (Forward Error Correction) scheme, a key factor in allowing the achievement of excellent performance in the presence of high levels of noise and interference - the FEC system is based on concatenation of BCH (Bose-Chaudhuri-Hcquengham) with LDPC (Low Density Parity Check) inner coding; ACM (Adaptive Coding and Modulation) allowing the transmission parameters to be changed on a frame by frame basis depending on the particular conditions of the delivery path for each individual user; optional backwards compatible modes that use hierarchical modulation to allow

legacy DVB-S receivers to continue to operate (ETSI EN 302 307 V1.2.1 (2009-08)).

DVB-S2 allows excellent performance, coming close to the Shannon limit, the theoretical maximum information transfer rate in a channel for a given noise level. It can operate at carrier-to-noise ratios from -2dB (i.e., below the noise floor) with QPSK, through to +16dB using 32APSK.

2.2 Global Positioning System (GPS)

GPS is a space-based satellite navigation system that provides location and time information in all weather conditions, anywhere on or near the Earth where there is an unobstructed line of sight to four or more GPS satellites. The system provides critical capabilities to military, civil and commercial users around the world. It is maintained by the US government and is freely accessible to anyone with a GPS receiver (http://en.wikipedia.org). The signals transmitted by GPS satellites encode a variety of information including satellite positions, the state of the internal clocks, and the condition of the network. The signals are transmitted on two carrier frequencies. Two different encodings are used: a public encoding that enables lower resolution navigation, and an encrypted encoding used by the U.S. military.

Each GPS satellite continuously broadcasts a navigation message on L1 C/A and L2 P/Y frequencies at a rate of 50 bit/s. Each complete message takes 750 seconds (12 1/2 minutes) to complete. The message structure has a basic format of a 1500-bit-long frame made up of five subframes, each subframe being 300 bits (6 seconds) long. Subframes 4 and 5 are subcommutated 25 times each, so that a complete data message requires the transmission of 25 full frames. Signals are encoded using code division multiple access (CDMA) allowing messages from individual satellites to be distinguished from each other based on unique encodings for each satellite (that the receiver must be aware of). Two distinct types of CDMA encodings are used: the coarse/acquisition (C/A) code, which is accessible by the general public, and the precise (P(Y)) code, which is encrypted so that only the U.S. military can access it.

2.3 GLONASS System

GLONASS is a Russian global satellite navigation system, providing real time position and velocity determination for military and civilian users. The satellites are located in middle circular orbit at 19,100 km altitude with a 64.8 degree inclination and a period of 11 hours and 15 minutes. GLONASS orbit makes it especially suited for usage in high latitudes (north or south), where getting a GPS signal can be problematic. The constellation operates in three orbital planes, with 8 evenly spaced satellites on each. A fully operational constellation with global coverage consists of 24 satellites, while 18 satellites are necessary for covering the territory of Russia. To get a position fix the receiver must be in the range of at least four satellites (http://en.wikipedia.org/wiki/GLONASS).

2.3.1 GLONASS System FDMA Structure

A Russian military GLONASS satellites combined with GLONASS/GPS receiver, transmit two types of signal: open standard-precision signal L1OF/L2OF, and obfuscated high-precision signal L1SF/L2SF. The signals use similar DSSS encoding and binary phase-shift keying (BPSK) modulation as in GPS signals. All GLONASS satellites transmit the same code as their standard-precision signal; however each transmits on a different frequency using a 15-channel frequency division multiple access (FDMA) technique spanning either side from 1602.0 MHz, known as the L1 band (http://en.wikipedia.org/wiki/GLONASS).

The center frequency is 1602 MHz + n × 0.5625 MHz, where n is a satellite's frequency channel number (n=−7,−6,−5,...0,...,6). Signals are transmitted in a 38° cone, using right-hand circular polarization, at an EIRP between 25 to 27 dBW (316 to 500 watts). The L2 band signals use the same FDMA as the L1 band signals, but transmit straddling 1246 MHz with the center frequency 1246 MHz + n×0.4375 MHz, where n spans the same range as for L1. A combined GLONASS/GPS Personal Radio BeaconThe open standard-precision signal is generated with modulo-2 addition (XOR) of 511 kbit/s pseudo-random ranging code, 50 bit/s navigation message, and an auxiliary 100 Hz meander sequence (Manchester code), all generated using a single time/frequency oscillator. The pseudo-random code is generated with a 9-stage shift register operating with a period of 1 ms (http://en.wikipedia.org/wiki/GLONASS).

The navigational message is modulated at 50 bit/s. The superframe of the open signal is 7500 bits long and consists of 5 frames of 30 seconds, taking 150 seconds (2.5 min.) to transmit the continuous message. Each frame is 1500 bits long and consists of 15 strings of 100 bits (2 seconds for each string), with 85 bits (1.7 seconds) for data and check-sum bits, and 15 bits (0.3 seconds) for time mark. Strings

1-4 provide immediate data for the transmitting satellite, and are repeated every frame; the data include ephemeris, clock and frequency offsets, and satellite status. Strings 5-15 provide non-immediate data (i.e. almanac) for each satellite in the constellation, with frames I-IV each describing 5 satellites, and frame V describing remaining 4 satellites.

The ephemerides are updated every 30 min. using data from the Ground Control segment; they use Earth Centred Earth Fixed (ECEF) Cartesian coordinates in position and velocity, and include lunisolar acceleration parameters. The almanac uses modified Keplerian parameters and is updated daily.

The more accurate high-precision signal is available for authorized users, such as the Russian Military, yet unlike the US P(Y) code which is modulated by an encrypting W code, the GLONASS restricted-use codes are broadcast in the clear using only 'security through obscurity'. The details of the high-precision signal have not been disclosed. The modulation (and therefore the tracking strategy) of the data bits on the L2SF code has recently changed from unmodulated to 250 bit/s burst at random intervals. The L1SF code is modulated by the navigation data at 50 bit/s without a Manchester meander code.

2.3.2 Subtitle GPS/GLONASS Satellite Availability and Observation Time

Based on the movement of the satellite (4 km/s) the bistatic radar imaging system can be regarded as a classical BSAR system in case of stationary targets or general BSAR system in case of a moving target. Approximately 6-8 satellites are simultaneously visible at a particular point on the Earth, at any time (Cherniakov, 2009). . Achievable observation time is defined as the amount of time that a target on the Earth is within the beam of a satellite (assuming it is always within the beam of the receiver). Even though the beam of the GNSS satellites covers a large part of the Earth's surface, the observation time may vary significantly from one satellite to another because of their position with respect to the target. As an example, Fig. 3 shows the results of Keplerian modeling (Zuo, 2007).

2.3.3 BSAR Azimuth Resolution

Within an interval of one day, 22 satellites are visible in a nearly quasi-monostatic mode, with observation times varying from 12 minutes to 3 hours. These values allow for very long integration times due to satellites' wide beam. It provides fine azimuth resolutions, and enhances power budget of the system. The maximum azimuth resolution that can be achieved for data in Fig. 3(a) is shown in Fig. 3(b). The resolution is calculated through Doppler bandwidth of the associated GPS azimuth signals, and dividing with the average speed of the satellite towards the observed target. The figure shows that extremely high azimuth resolutions can be potentially achieved if the full observation time is processed. Even for an observation time of 12 minutes the resolution is reasonable (Cherniakov, 2009).

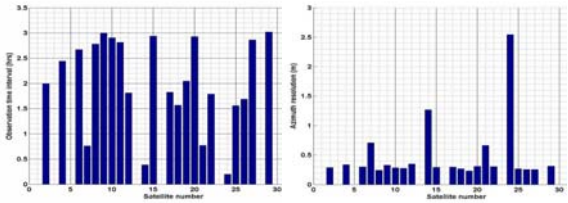

(a) (b)

Figure 3: Observation time (a) azimuth resolution (b).

These values allow for very long integration times due to satellites' wide beam. It provides satisfactory azimuth resolutions, and enhances power budget of the system.

2.3.4 BSAR Power Budget

Since GNSS satellites exhibit a low signal power density on the Earth's surface, long observation times will essentially enhance the signal-to-noise ratio (SNR) at the output of the image formation algorithm used (Cherniakov, 2009). Assuming full target signal compression in both range and azimuth, the SNR is defined as

$$\left(\frac{S}{N}\right) = \frac{P_D G_R \lambda^2 \sigma T_{\text{int}} T_{obs}}{(4\pi)^2 R_R^2 k T_S (\Delta u)} \qquad (1)$$

where P_D is the signal power density of the GNSS satellites on the Earth, G_R is the gain of the receiving antenna, λ is the radar wavelength, σ is the target radar cross section, R_R is the receiver-to-target range, k is Boltzmann's constant, T_S is the receiver noise temperature, T_{int} is the integration time in the range direction (equal to the length of the transmitted GNSS code sequence), T_{obs} is the observation time and Δu is the azimuth sample spacing. The exemplary parameters in case of Galileo, its E_5 signal and receiver are as follows: $P_D = 3.0628 \times 10^{-14}$ W/m^2, G_R =10 dB, λ = 0.25 m, R_R = 100-1000 m, T_S = 410 K, T_{int} = 1 ms, T_{obs} =12 min, Δu = 1 ms, σ = 5, 10, 25 m^2.

2.4 BSAR Potential Targets

Orbital parameters of ballistic missile velocity and apogee made them most appropriate for targets of BSAR with satellite based transmitters of opportunity. The level of the reflected power from the targets is sufficient enough to be detected and tracked on a great distance.

Orbital parameters of ballistic missile are as follows:(http://www.alternatewars.com/BBOW/ABM/BM_Classes.htm): **Battlefield Ballistic Missiles**: Range 1-149 km, Apogee 0.25 – 37 km, T_{Fl} = 14-171 s, ΔV= 0.09-1.1 km/s; **Short-Range Ballistic Missiles**: Range 150-799 km, Apogee 38 - 200 km, T_{Fl} = 171-396 s, ΔV=1.1-2.54 km/s; **Medium Range Ballistic Missiles**: Range 800-2,399 km, Apogee 200-600 km, T_{Fl} = 396-686 s, ΔV=2.55-4.41 km/s; **Intermediate-Range Ballistic Missiles**: Range 2,400 - 5,499 km, Apogee 600-1,375 km, T_{Fl} = 686-1,038 s, ΔV=4.41-6.67 km/s; **Intercontinental Ballistic Missiles**: Range 2,400 - 5,499 km, Apogee 1,375-4,993 km, T_{Fl} = 61,038-1,978 s, ΔV= 0.67-12.72 km/s.

All kind of aircrafts, helicopters and launch rockets, UMA vehicles, moving and stationary objects on earth and at sea are also considered as potential targets of BSAR systems with non-cooperative transmitters.

3 GEOMETRY, SIGNALS, AND IMAGE RECONSTRUCTION ALGORITHMS

3.1 Principle Bistatic Radar Geometry

Bistatic radar geometry is presented in Fig. 4, where $R_T(t)$ is the distance between the transmitter and target, $R_R(t)$ is the distance between the target and receiver, θ is the bistatic angle.

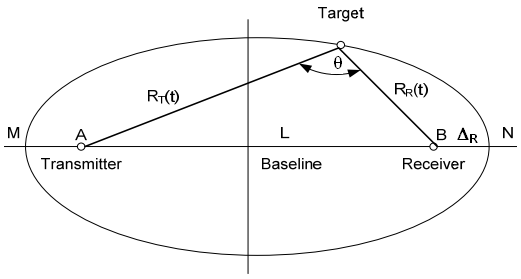

Figure 4: Principle bistatic radar geometry.

The contours of the constant bistatic range are ellipses with transmitter and receiver as the two foci are described by the equation

$$R_T(t) + R_R(t) = L + 2.i.\Delta_R, \quad (2)$$

where i = 1, 2, …is the number of equal range ellipse, L = AB is the baseline, Δ_R is the monostatic SAR range resolution.

3.2 Vector Model of Real BSAR Topology

In case of real BSAR topology assume a GPS transmitter, stationary receiver located on the land, and a moving target all situated in Cartesian coordinate system *Oxyz*. The target presented as an assembly of point scatterers is depicted in its own Cartesian coordinate system *OXYZ*. The generalized vector geometry of BSAR scenario is illustrated in Fig. 5. The vector $\mathbf{R}^s(p)$ is the current vector position of the transmitter. The vector $\mathbf{R}_{ijk}$ is the position vector of *ijk*th point scatterer in the coordinate system *OXYZ* and the vector $\mathbf{R}_{00'}(p)$ is the current vector position of the mass center of the target in discrete time instant p. The vector $\mathbf{R}^r$ is the stationary vector position of the receiver. The vector $\mathbf{R}^s_{0'}(p)$ is the distance vector from the transmitter to the mass center of the target (Lazarov, 2013).

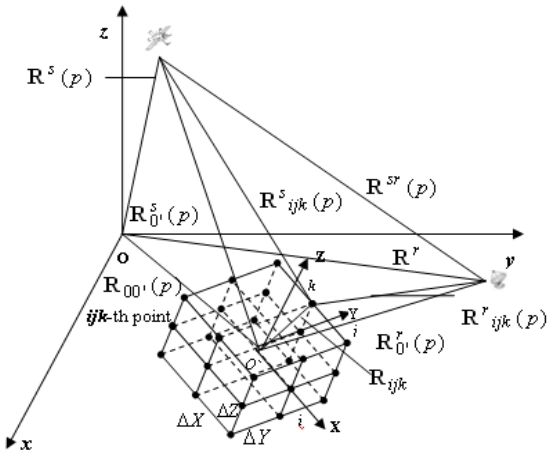

Figure 5: Real vector BSAR topology.

The module of the vector distance transmitter-*ijk*th target point scatterer-receiver is defined by the expression

$$R_{ijk}(p) = \left|\mathbf{R}^{s}{}_{ijk}(p)\right| + \left|\mathbf{R}^{r}{}_{ijk}(p)\right|. \qquad (3)$$

Equation (3) is used while modeling BSAR signals.

3.3 BSAR Signal Model

The GPS transmitter emits phase modulated continuous waves (CW) illuminating a target and traveling directly towards a GPS receiving antenna. In the receiving antenna an interference of reflected delayed and Doppler modulated from the moving target waves and none impacted by the target waves occurs. The resulting signal carries information regarding two-dimensional (2-D) geometry of the target. Delays of the signals reflected from the point scatterers of the object is referred to as range dimension and can be extracted by conventional correlation procedure called range compression. Doppler shifts of the received signal are referred to as azimuth dimension and can be extracted by standard fast Fourier procedure applied over the range compressed signal.

3.3.1 Phase Code Modulated Transmitted Waveform

During aperture synthesis GPS and/or DVB-S transmitters illuminate targets by phase-code modulated waveform described by the expression

$$S(t) = a.\exp\{-j[\omega(t) + \pi b(t) + \varphi_0]\}, \qquad (4)$$

where a is the amplitude of the transmitted pulses, $\omega = 2\pi c/\lambda$ is the signal angular frequency, φ_0 is the initial phase, λ is the wavelength, c is the speed of light, $b(t)$ is the binary parameter of the phase-code modulated sequence.

The direct waveform from the GPS transmitter is used as a reference signal for phase demodulation and range compression by correlation in fast time domain.

The deterministic components of the SAR signal return, reflected by all point scatterers of the object are derived by (Lazarov, 2014)

$$S(p,t) = \sum_{ijk} a_{ijk}\mathbf{exp}\{-j[\omega(t - t_{ijk}(p)) + \pi b(t)]\}, \qquad (5)$$

where a_{ijk} is the image function $t_{ijk}(p) = \dfrac{R_{ijk}(p)}{c}$ is round trip delay transmitter-*ijk*th target point-receiver.

3.3.2 GPS C/A Phase Code Construction

GPS C/A phase code modulated CW waveforms for BSAR purposes is defined by parameters: carrier frequency $f = 1.57.10^9$ Hz, registration time interval (segment repetition period) $T_p = 2.2.10^{-3}$ s, chip rate 1.023 MHz, segment timewidth $T = 10^{-3}$ s, C/A phase pulse timewidth $\Delta T = 0.9775.10^{-6}$, full number of chips $K = 1023$, number of transmitted segments during aperture synthesis $N = 1024$. Two TFSRs (Tapped Feedback Shift Registers) are used to generate a sequence of "0"s and "1"s of the phase parameter $b(t)$ at the clock rate of 1.023 MHz each generating a Gold Codes by polynomials:

$1 + X^3 + X^{10}$ (code G_1),

$1 + X^2 + X^3 + X^6 + X^8 + X^9 + X^{10}$ (code G_2).

There are 36 unique codes that can be generated in such a manner.

3.3.3 GPS P Phase Code Construction

Consider a GPS transmitter illuminating a target with a segment of K chips (phase pulses) of GPS P phase code modulated waveform. Each P phase code modulated segment can be expressed by equation (5), where $T = 13/(10.23\times10^6)$ s is the time duration of the segment, $b(t)$ is the binary time sequence that modulates the phase of the GPS signal, in case of a segment of K=13 chips, $b(t)$ can accept sequence of binary values: 1001001001000.

The GPS P phase code modulated waveform for BSAR purpose is characterized by the following parameters: carrier frequency L1=1575.42 MHz, measurement segment with K=13 chips, segment timewidth $T = 13/(10.23\times10^6)$ s, chip rate 10.23×10^6, period of 6.1871×10^{12} chips. P code is generated by four 12-bit shift registers designated by polynomials X1A, X1B, X2A, and X2B, as follows (Farmer, 1993):

X1A:$1 + X^6 + X^8 + X^{11} + X^{12}$;
X1B:$1 + X^1 + X^2 + X^5 + X^8 + X^9 + X^{10} + X^{11} + X^{12}$;
X2A:$1 + X^1 + X^3 + X^4 + X^5 + X^7 + X^8 + X^9 + X^{10} + X^{11} + X^{12}$;
X2B:$1 + X^2 + X^3 + X^4 + X^8 + X^9 + X^{12}$

Initial states of the registers: X1A: 001001001000; X1B: 010101010100; X2A: 100100100101; X2B: 010101010100.

3.3.4 DVB-T waveform Construction

The DVB-T waveform can be presented as an adjacent sum of multiplications of complex exponential functions as follows (Lazarov, *IRS*-2014)

$$s(t) = \mathrm{Re}\left[\exp(j2\pi f_c t) \sum_{m,l,n} c_{m,l,k} . \psi_{m,l,k}(t) \right] \quad (6)$$

where $m = \overline{0,\infty}$ is the index that stands for the number of frame of the DVB-T signal and accepts value in the interval $m = \overline{0,\infty}$, is the index that stands for the number of the OFDM (Orthogonal Frequency Division Multiplexing) symbol and accepts value in the interval $l = \overline{0,67}$, $k = \overline{-\frac{K}{2}+1, K}$ is the index that stands the number of frequency and accepts value in the interval, $K = 6817$ is the number of transmitted carriers. $c_{m,l,k}$ is the complex symbol for carrier k of the data symbol number l in frame number m (the modulation of the complex signal $c_{m,l,k}$ is Quadrature Phase Shift Keying (QPSK), Quadrature Amplitude Modulation (QAM) - 16-QAM or 64-QAM) [8], the exponential function $\psi_{m,l,k}(t)$ is defined as follows. In case the time parameter accepts values $t = \overline{(l+68.m).T_S, (l+68.m+1).T_S}$ with step interval Δt, then

$$\psi_{m,l,k}(t) = \exp\left[j2\pi.k.\left(\frac{1}{T_S}\right).(t - \Delta - l.T_S - 68.m.T_S) \right] \quad (7)$$

where $t = (l+68.m).T_S + k.\Delta t$ for $k = \overline{-\frac{K}{2}+1, \frac{K}{2}}$, $T_S = 896\times10^{-6}$ s is the symbol duration, $\Delta = 224\times10^{-6}$ s is the guard interval, $\Delta t = \frac{T_S}{K} = 0.131\times10^{-6}$ s is the DVB-S sample duration, $\left(\frac{1}{T_S}\right) = 1.116$ kHz is the carrier spacing, $\Delta f = \frac{1}{\Delta t} = \frac{K}{T_S} = 7.61\times10^{6}$ Hz is the frequency bandwidth of the time sample Δt Otherwise the complex function accepts value $\psi_{m,l,k}(t) = 0$.

3.3.5 Image reconstruction algorithm

Main steps of image reconstruction algorithm are as follows.

Phase correction of the BSAR signal accomplished by multiplication of the phase demodulated BSAR signal with an exponential phase correction function, i.e.

$$\widetilde{S}(p,k) = \hat{S}(p,k).\mathbf{exp}(j\Phi(p,k) \quad (8)$$

Range compression accomplished by correlating of the phase corrected SAR signal $\widetilde{S}(p,k)$ with reference function complex conjugated of the transmitted phase code modulated signal $\mathbf{exp}[j\pi b((k-\hat{k}+1)\Delta T)]$, i.e.

$$\widetilde{S}(\hat{p},\hat{k}) = \sum_{k=\hat{k}}^{\hat{k}+K-1} \widetilde{S}(p,k)\mathbf{exp}[j\pi b((k-\hat{k}+1)\Delta T)] \quad (9)$$

$p = \overline{1,N}$, $\hat{k} = \overline{1,L}$

Azimuth compression and complex image extraction accomplished by Fourier transformation of the range compressed SAR data, i.e.

$$a_{ijk}(\hat{p},\hat{k}) = \sum_{p=\overline{1,N}} \widetilde{S}(p,\hat{k})\mathbf{exp}\left\{ j\left[\frac{2\pi}{N}\hat{p}.p \right] \right\}. \quad (10)$$

Final image extraction by modulo operation

$$a_{ijk}(\hat{p},\hat{k}) = \left| \sum_{p=\overline{1,N}} \widetilde{S}(p,\hat{k})\mathbf{exp}\left\{ j\left[\frac{2\pi}{N}\hat{p}.p \right] \right\} \right|. \quad (11)$$

3.4 Numerical Experiments

3.4.1 BSAR with GPS C/A PCM Waveform

Assume a target, flying helicopter (Fig. 6), moves rectilinearly in a coordinate system of observation (Fig. 5). GPS transmitter illuminates a target by a C/A code waveform.

Coordinates of the GPS satellite are: $x^s(0) = -50$ m, $y^s(0) = 0$ m, and $z^s(0) = 20.10^6$ m. GPS satellite velocity: $v_x^s = 3819.206$ m/s, $v_y^s = 3819.206$ m/s, $v_z^s = 0$ m/s. Coordinates of the stationary GPS receiver: $x^r = 55$ m, $y^r = 45$ m and $z^r = 30$ m. The trajectory parameters of the target: velocity $V = 80$ m/s; velocity guiding angles

$\alpha = -\pi$, $\beta = -\frac{\pi}{2}$, and $\gamma = \frac{\pi}{2}$; coordinates of the target mass-centre: $x_{00'}(0) = 20$ m, $y_{00'}(0) = 10$ m, $z_{00'} = 100$ m.

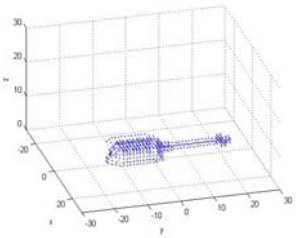

Figure 6: BSAR target.

Real part and imaginary parts of a BSAR signal are presented in Figs 7(a), and (b), respectively.

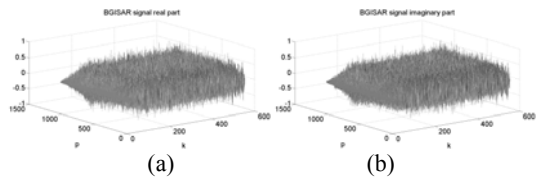

(a) (b)

Figure 7: BSAR signal: real (a) and imaginary (b) parts.

The final BSAR image, module of the complex image in isometric projection (a) and pseudo color map (b) of the flying helicopter is depicted in Fig. 8.

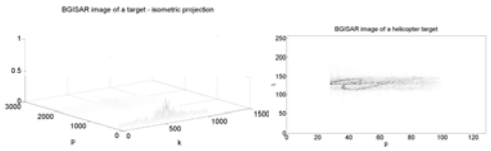

Figure 8: BSAR image of the helicopter in isometric projection (a) and pseudo colour map (b).

The quality of imaging is no satisfactory, which can be regarded as illustration of bad range resolution capabilities of GPS C/A code in its BSAR application. The GPS C/A code can be used only for target detection and preliminary recognition.

3.4.2 BSAR with GPS P PCM Waveform

Assume a target, flying helicopter (Fig.6), is moving rectilinearly in a coordinate system of observation (Fig. 5). Coordinates of the GPS satellite: $x^s = 1{,}5.10^4$ m, $y^s = 2.10^4$ m; $z^s = 2.10^5$ m. Coordinates of GPS satellite vector velocity: $v_x^s = 3819.206$ m/s, $v_y^s = 3819.206$ m/s, $v_z^s = 0$ m/s. Coordinates of the stationary GPS receiver: $x^r = 970$ m, $y^r = 10^3$ m and $z^r = 30$ m. Trajectory parameters of the target: module of the vector velocity $V = 80$ m/s; guiding angles $\alpha = \pi/4$, $\beta = \pi/4$, $\gamma = 3\pi/2$; coordinates of the target's mass-centre in the moment of imaging $p = N/2$: $x_{00'} = 20$ m, $y_{00'} = 10$ m, $z_{00'} = 150$ m. Parameters of the GPS P phase code waveform: wavelength $\lambda = 19{,}1.10^{-2}$ m, carrier frequency $f = 1.57.10^9$ Hz, number of GPS P chips in the segment $K = 13$, range sample number 256, number GPS P phase code segments during aperture synthesis $N = 512$, segment repetition period $T_p = 10^{-2}$ s.

The real and imaginary pats of a BSAR signal are presented in Fig. 9 (a) and (b), respectively

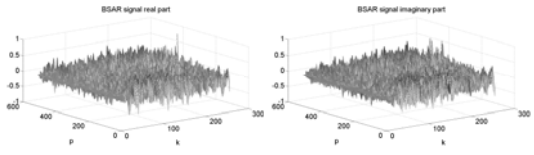

(a) (b)

Figure 9: BSAR signal: real (a) and imaginary (b) parts.

Fig. 10 presents the unfocused (a) and focused (b) BSAR images of the helicopter. The quality of the of unfocused image is satisfactory, which can be regarded as illustration of range resolution capabilities of a GPS P phase code waveform in BSAR application.

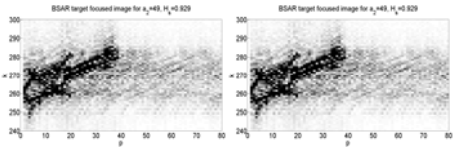

(a) (b)

Figure 10: BSAR unfocused (a) and focused (b) images.

As can be noticed in Fig. 10 (b) the target's image quality is improved. Details of the helicopter construction are seen clearly. The results of the numerical experiment prove theoretically that the GPS P phase code waveform can be applied in BSAR scenario in order to obtain an image of moving targets illuminated by GPS transmitter of

opportunity and stationary GPS receiver hardware modified for BSAR application.

3.4.3 BSAR with DVB-T Waveform

Assume a target is moving rectilinearly in a 3-D Cartesian coordinate system of observation $Oxyz$. Coordinates of the transmitter: $x^s = -250$ m; $y^s = 0$ m; $z^s = 150$ m. Coordinates of the receiver: $x^r = 3000$ m; $y^r = 110$ m; $z^r = 12$ m. target parameters are: module of the vector velocity $V = 10$ m/s; $\alpha = \pi/4$; $\beta = \pi/4$; $\gamma = \pi/2$. The coordinates of the mass-center at the moment $p = N/2$: $x_{00}(0) = 25$ m; $y_{00}(0) = 50$ m; $z_{00}(0) = 2$ m. Stepped frequency (SF) DVB-T segment's parameters: pulse repetition period $T_p = 7 \times 10^{-3}$ s, SF DVB-T segment width $T = 896.10^{-6}$ s, number of samples of LFM transmitted signal $K = 6817$, carrier frequency $f = 0.86 \times 10^9$ Hz, SF DVB-T sampling period $\Delta T = T/K = 0.13 \times 10^{-6}$ s, bandwidth of SF DVB-T $\Delta F = 7.61 \times 10^6$ Hz, number of transmitted stepped frequency modulated pulses $N = 256$.
Real and imaginary parts of DVR-T BSAR signal are presented in Figs. 11 (a) and (b) respectively.

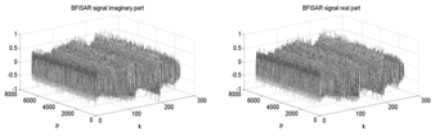

(a) (b)

Figure 11: BSAR signal: real (a) and (b) imaginary part.

An isometric image and pseudo colour map image of a ship target obtained by DVB-T BSAR technique are presented in Fig. 12(a) and (b), respectively.

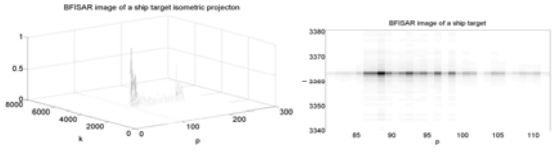

(a) (b)

Figure 12: DVB-T BSAR isometric image (a) and pseudo color map image (b), respectively.

As can be seen the azimuth rezolution is satisfactory whereas range resolution is poor. The latter is due to not necessary wide frequency bandwidth of the DVB-T signal, $\Delta F = 7.61 \times 10^6$ Hz.

3.5 BSAR Signal Formation by Compressed Sensing

The lower bandwidth of certain television channel does not guarantee good range resolution. To reach the desired range resolution, multiple DVB-T channels can be coherently adjoined to form a wideband signal. DVB-T channels are spectrally separated by frequency gabs. Such gaps lead for degradations of the ISAR image, when classical Fourier techniques, such as the Range-Doppler (RD) technique, are used to form the image of the target. Based on sparsety of BSAR image, composed of few prominent scattering centers, the Compressed Sensing (CS) theory is applied to address the problem of forming an ISAR image when spectrally separated DVB-T channels are available. As the spectrum of a stepped frequency modulated signal well approximates the spectrum of the DVB-T signal that is constant within the signal bandwidth SF waveform is used to model the emitted signal (Qiu, 2013).

Assume that measurement and object coordinate plane coincide. The BSAR signal reflected by the whole object is a geometry sum of BISAR signals reflected from all point scatterers, placed on the target surface and can be written as

$$S(p,k) = \sum_{\hat{p}=0}^{P-1} \sum_{\hat{k}=0}^{Q-1} a_{\hat{p},\hat{k}} \exp\left[j(2\pi . \hat{f} \hat{t}_{\hat{p},\hat{k}}) \right], \qquad (12)$$

where $\hat{f} = (f_0 + k.\Delta f)$,

$\hat{t}_{\hat{p},\hat{k}} = \left(t_{\hat{p},\hat{k}\min}(p) + k\Delta T - t_{\hat{p},\hat{k}}(p) \right)$,

$p = \overline{0, N-1}$, $k = \overline{0, K-1}$ are indexes of azimuth and range measurements, respectively, $\hat{p} = \overline{0, P-1}$, $\hat{k} = \overline{0, Q-1}$ are the unknown discrete coordinates of the point of imaging of particular target's point scatterer with magnitude $a_{\hat{p},\hat{k}}$, P and Q is the full number of imaging points on two coordinate axes, N and K are the full number of measurements on azimuth and range direction, respectively, ΔT is the time sample on range direction, Δf is the frequency sample, $t_{p,k}(p) = \dfrac{R_{p,k}(p)}{c}$ is the round trip time delay transmitter-($\hat{p}\hat{k}$)th point scatterer – receiver,

where $R_{p,k}(p) = R_{T,\hat{p}\hat{k}}(p) + R_{R,\hat{p}\hat{k}}(p)$ is time and velocity dependent current distance between transmitter – ($\hat{p}\hat{k}$)th point scatterer – receiver, where $R_{p,k}(p) = R_{T,\hat{p}\hat{k}}(p) + R_{R,\hat{p}\hat{k}}(p)$ is time and velocity dependent current distance between transmitter ($\hat{p}\hat{k}$)th point scatterer – receiver. First order two dimensional Taylor expansion of the phase term of $S(p,k)$ on p and k in the vicinity of the imaging point with discrete coordinates $\hat{p}$ and $\hat{k}$ yields (Qiu, 2013)

$$S(p,k) = \sum_{\hat{p}=0}^{P-1}\sum_{\hat{k}=0}^{Q-1} a_{\hat{p},\hat{k}} \mathbf{exp}\left[-j\left(2.\pi\frac{p.\hat{p}}{N}\right)\right]\times \mathbf{exp}\left[-j\left(2.\pi\frac{k.\hat{k}}{K}\right)\right] + n(p,k) \quad (13)$$

which can be rewritten in matrix form as follows

$$\mathbf{S} = \hat{\mathbf{P}}\mathbf{A}\hat{\mathbf{K}}^H + \mathbf{N} \quad (14)$$

where $\mathbf{S}(N\times K)$ is the measurement matrix, $\mathbf{A}(P\times Q)$ is the BISAR image matrix, $\hat{\mathbf{P}}(N\times P)$ and $\hat{\mathbf{K}}(K\times Q)$ are overcomplete partial Fourier dictionaries in the range and azimuth domains, $\mathbf{N}(N\times K)$ is the noise matrix. Matrices $\hat{\mathbf{P}}$ and $\hat{\mathbf{K}}$ can be rewritten as (Qiu, 2013)

$$\hat{\mathbf{P}} = [\mathbf{p}_0, \mathbf{p}_1, ...\mathbf{p}_{\hat{p}}, ..., \mathbf{p}_{P-1}], \quad (15)$$

$$\hat{\mathbf{K}} = [\mathbf{k}_0, \mathbf{k}_1, ...\mathbf{k}_{\hat{k}}, ..., \mathbf{p}_{Q-1}], \quad (16)$$

where

$$\mathbf{p}_{\hat{p}} = \left[e^{-j2\pi.\hat{p}.0/P}, e^{-j2\pi.\hat{p}.1/P}, ..., e^{-j2\pi.\hat{p}.(N-1)/N}\right]^T$$

$$\mathbf{k}_{\hat{k}} = \left[e^{-j2\pi.\hat{k}.0/P}, e^{-j2\pi.\hat{k}.1/P}, ..., e^{-j2\pi.\hat{k}.(K-1)/K}\right]^T$$

$\hat{p} = \overline{0, P-1}$, $\hat{k} = \overline{0, Q-1}$.

Each non-zero $\hat{p}\hat{k}$ th point scatterer of **A** represents one point scatterer. Generally, the whole non-zero pixels occupy only a small part of the image plane, which motivates the CS approach to reconstruct **A** from **S**. In case of additive noise, the BSAR imaging problem is written as (Qiu, 2013)

$$\min\|\mathbf{A}\|_0 \text{ s.t. } \left\|\mathbf{S} - \mathbf{P}\mathbf{A}K^H\right\|_F^2 < \varepsilon. \quad (17)$$

where $\|.\|$ denotes the number of non-zero components in **A,** $\|..\|_F^2$ represents the Frobenius norm of a matrix, and ε is a small constant.

Based on the frequency gabs in DVB-T signals, the matrix **P** is modified by replacing the rows corresponding to the gaps with 0. This new matrix is marked as **P′**. An identity Gaussian matrix is used as sensing matrix. Then **S** can be reconstructed by using 2D-SL0 algorithm, where the matrix **P** should be replaced by the matrix **P′**. The 2D-SL0 algorithm uses a Gaussian function to approximate the l_0 norm (Qiu, 2013), i.e.

$$\|\mathbf{A}\|_0 = PQ - \sum_{\hat{p}=0}^{P-1}\sum_{\hat{q}=1}^{Q-1} \exp\left\{-\frac{\|\mathbf{A}(\hat{p},\hat{k})\|}{\sigma}\right\} \quad (18)$$

The 2D-SL0 algorithm can solve (17) using a projective steepest ascent approach. After obtaining estimation of **A**, and by using the known dictionaries **P** and **Q**, the full band measurement $\hat{\mathbf{S}}$ is defined by

$$\hat{\mathbf{S}} = \mathbf{P}.\hat{\mathbf{A}}.\mathbf{K}^H \quad (18)$$

where $\hat{\mathbf{A}}$ is the estimation of **A**.

Then a 2D-FT transform is applied to $\hat{\mathbf{S}}$ in order to obtain a BSAR image which is comparable with that one obtained by applying the RD techniques to the original data **S**.

3.5.6 Numerical experiment

Numerical experiments are carried out to test the CS algorithm using simulated DVB-T. The target is composed of 35 scatterers with the dimensions similar to a Boing 747 [14]. The cases of adjacent channels and non-adjacent channels are considered to verify the approach. To evaluate the quality of the BSAR image an image entropy function is applied. Results in case of adjacent channels are presented in Fig. 13.

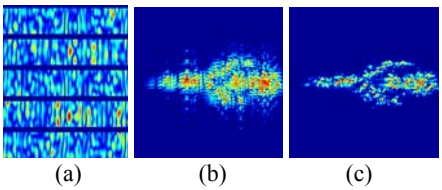

(a) (b) (c)

Figure 13: Spectrum of adjacent channels (a), BSAR image before filling the gaps(b), after filling the gaps (c).

In Fig.13 (a) a DVB-T signal composed of adjacent channels is depicted. Fig. 14 (b) shows the BSAR image after applying 2D-FT to the

incomplete data. This image is affected by grating lobes. Fig.13 (c) depicts the BSAR image using 2-D FT after applying the CS algorithm. Visibly, the grating lobes are eliminated effectively.

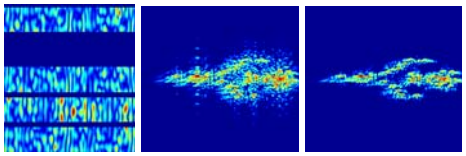

(a) (b) (c)

Figure 14: Spectrum of non-adjacent channels (a), BSAR image before filling the gaps(b), after filling the gaps (c).

Results in case of non-adjacent channels (channels 1, 3, 4, and 5) are presented in Fig. 14. In Fig.14 (a) the DVB-T signal considered here is composed of channels 1,3,4 and 5. Fig. 14 (b) shows the BSAR image after applying the 2D-FT to the incomplete data. This image is seriously affected by grating lobes. Fig. 14 (c) depicts the BSAR image using 2-D FT after applying the CS algorithm. Visibly, the grating lobes are eliminated effectively. Entropy of these two images is 9.31 and 8.65, respectively, indicating that the image is improved.

4 FIELD EXPERIMENTAL RESULTS

3.1 Description of Experiments

Experiments were conducted be the team of University of Birmingham. Consider BSAR with GNSS transmitter of opportunity, stationary target and stationary receiver. The target area was Metchley park, located to the West (Fig. 15, and Fig. 16).

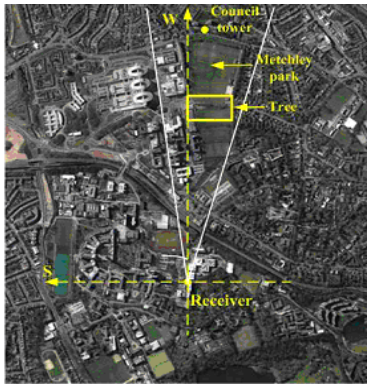

Figure 15: Satellite photo of full-size target area.

(a) (b)

Figure 16: Photo of council tower at far end (a), and trees in middle range (b).

A low-gain (HC) antenna registers a direct satellite signal for signal synchronization. A directional (RC) antenna, pointing towards the imaging scene, measures satellite signal reflections for imaging (Fig. 17 (a)) (Antoniou, 2012).

Four experiments with four different satellite positions are carried out. Satellite locations vary in both azimuth and elevation angles, resulting in bistatic angles from 540 to 910 (Fig. 17 (b)).

Satellite parameters: GLONASS, carrier band: L1, Waveform – P code, Signal bandwidth: 511 MHz, Integration time: 200 ms, Segment repetition period 1 KHz.

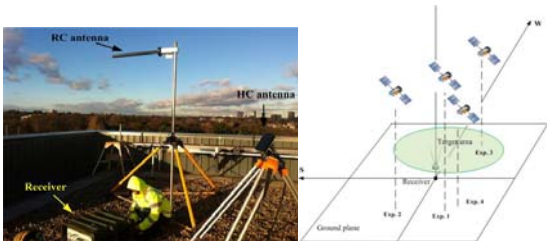

(a) (b)

Figure 17: Experimental equipment and satellite positions during experiments.

3.2 BSAR Image Analysis

After collecting data, synchronization and bistatic image formation were performed to get BSAR image. The images obtained from the four experiments are shown in Fig. 18, superimposed on a satellite photograph of the area. The dynamic range for all four images was clipped to 15 dB. The images have identical geometrical sizes, from -500 m to 500m in cross-range (Southings) and from 300m to 1500m in range (Westings) (Zeng, 2013).

The reflectivity of different targets at various bistatic geometries is evaluated. Two objects were of interest in the images: the buildings at 1.2 km (Fig.16 (a)) and the trees at approximately 800m range (Fig. 16 (b)). Signal-to-noise ratio (SNR) for each object is calculated (Fig. 18). SNR variation for both objects is 12-13 dB, depending on the position of the satellite. The maximum SNR for both objects

is obtained in Image 2, which is expected since it corresponds to a quasi-monostatic acquisition. In this case, their SNRs are similar (but note the buildings are located at approximately twice the distance of the trees). In image 3 (Fig. 18 (c)) and image 4 (Fig. 18 (d)), tree reflectivity is about 6 dB higher than that of the building. At the same time, in image 1 (Fig. 18 (a)) the reflectivity of the building is much higher than that of the tree.

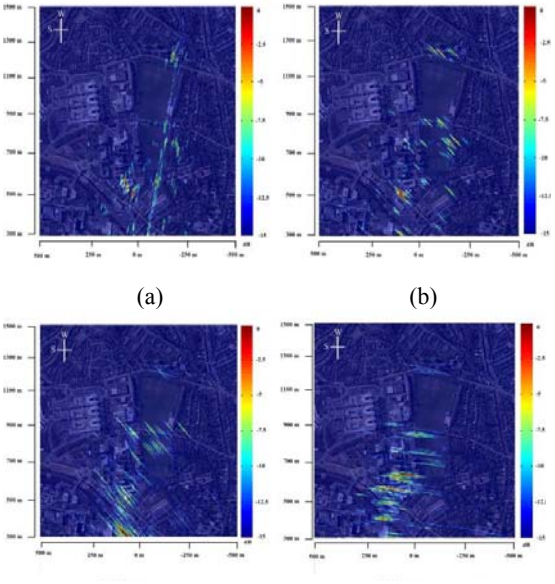

(a) (b)

(c) (d)

Figure 18: Images obtained for four positions of satellites: image 1 (a), image 2 (b), image 3 (c) image 4 (d).

5 CONCLUSIONS

BSAR system with a satellite transmitter of opportunity has been analyzed. The accent has been made on satellite communication system Astra and GNSS as carriers of non cooperative transmitters. Orbital parameters of potential targets as ballistic missiles have been given. Vector geometry of BSAR topology and main image reconstruction equations has been described. Results of numerical experiments performed by GPS and DVB-T waveforms have been presented and discussed. A compressed sensing algorithm to remove frequency gabs between DVB-T channels has been illustrated. Results of field experiments are presented.

ACKNOWLEDGEMENTS

Paper is supported by BFU/02/2014, and IICT-BAS.

REFERENCES

Whitewood, A.P., Baker, C.J., Griffiths, H.D., 2007, Bistatic radar using a spaceborne illuminator, In *IEE international radar conference*, Edinburgh.

Cherniakov, M. Saini, R., Zuo, R. Antoniou, M., 2007. Space-Surface Bistatic Synthetic Aperture Radar with Global Navigation Satellite System Transmitter of Opportunity – Experimental Results, In *IEE Proc. Radar Sonar Navig*., vol. 1, no. 6, pp. 447-458.

https://es.ses-astra.com/18579930/3A-footprint-fact-sheet.pdf

ETSI EN 302 307 V1.2.1 (2009-08), European Standard Telecommunications series Digital VideoBroadcasting (http://www.etsi.org/deliver/etsi_en/302300_302399/302307/01.02.01_60/en_302307v010201p.pdf).

http://en.wikipedia.org/wiki/Global_Positioning_System.

http://en.wikipedia.org/wiki/GLONASS.

Zuo, R., Saini, R., Cherniakov, M., 2007. Non-cooperative transmitter selections for Space-Surface Bistatic SAR, *Defence Technology Centre (DTC) Conference*, Edinburgh.

Cherniakov, M., Plakidis, E., Antoniou, M., Zuo, R., 2009. Passive Space-Surface Bistatic SAR for Local Area Monitoring: Primary Feasibility Study, In *6th European Radar Conference*, 30 Sept. - 2 Oct., Rome, Italy, pp 89-92.

Big book of warfare and other stuff (http://www.alternatewars.com/BBOW/ABM/BM_Classes.htm).

Lazarov, A. D., Chen, V.C., Kostadinov, T., Morgado, J., 2013. Bistatic SAR System with GPS Transmitter, *In Radar 2013*, Ottawa, 28 April-3 May.

Lazarov, A.D., Kostadinov T.P., 2014. Bistatic SAR/GISAR/FISAR Geometry*, Signal Models and Imaging Algorithms*, ISTE, John Wiley & Sons, Inc..

Farmer D., Martin K., Patent No. 5202604, 13 April 1993.

Lazarov, A.D., Kabakchiev, Hr., Kostadinov, T., 2014. DVB-T bistatic forward scattering inverse synthetic aperture radar imaging, In *Int. Radar Symposium* (*IRS*), June 16-18, Gdansk, pp 296-299.

Qiu, W., Giusti, E., Martorella, M., Zhao, H Z., Fu, Q., 2013. Compressive sensing for Passive ISAR with DVB-T signal, In *Int. Radar* Symposium (*IRS*), Dresden, vol. 1, 19-21 June, pp. 113 – 118.

Zeng, Z.,. Antoniou, M., Zhang, Q., Hui, M., Cherniakov, M., 2013. Multi-perspective GNSS-based Passive BSAR: Preliminary Experimental Results, In *Int. Radar Symposium* (*IRS*), Dresden, vol.1, 19-21 June, pp. 467 – 472.

Antoniou, M., Zeng, Z., Liu, F., Cherniakov, M., 2012. "Experimental demonstration of passive BSAR imaging using navigation satellites and a fixed receiver", In *Geoscience and Remote Sensing Letters*, vol. 9, pp. 477-481.

BRIEF BIOGRAPHY

Andon Dimitrov Lazarov received MS degree in Electronics Engineering from Sent Petersburg Electro-technical State University, Russia in 1972, and Ph. D. degree in Electrical Engineering from Air-Defense Military Academy, Minsk, Belarus in 1978, and Doctor of Sciences degree from Artillery and Air-Defense University, Bulgaria. From 2000 to 2002 he is a Professor at the Air Defence Department with Artillery and Air-Defense University. From 2002 he is a Professor with Bourgas Free University. He teaches Discrete Mathematics, Coding theory, Antennas and Propagation, Digital Signal Processing, Mobil Communications. His field of interest includes SAR, ISAR and InSAR modeling and signal processing techniques. He has authored above 150 research journal and conference papers. He is a secretary of Commission F of URSI Committee – Bulgaria, and a member of the IEEE, AES-USA, and in reviewer and editorial boards of IET - Canada, PIER & JEMWA – USA, Journal of radar technology, Beijing, China. EURASIP Journal on advances in signal processing - USA.

PAPERS

TaD MODEL OF TOPSIDE IONOSPHERE AND PLASMASPHERE FOR GNSS APPLICAT

Ivan Kutiev
Bulgarian Academy of Science , Acad.G. Bonchev str., bl.3, Sofia 1113, Bulgaria; National Observatory of Athens, Lofos Nymfon, GR11810, Thission, Athens, Greece
ivankutiev@yahoo.com

Pencho Marinov
Bulgarian Academy of Science , Acad.G. Bonchev str., bl.3, Sofia 1113, Bulgaria
pencho@parallel.bas.bg

Anna Belehaki, and Ioanna Tsagouri
National Observatory of Athens, Lofos Nymfon, GR11810, Thission, Athens, Greece
belehaki@space.noa.gr, tsagouri@space.noa.gr

Keywords: Topside ionosphere, Plasmasphere, Electron density profiles, TEC maps..

Abstract: TaD model reconstructs Ne profiles from the bottom of ionosphere up to GPS orbit heights. It is developed on the base of TSM (Topside Sounder Model), which provides the topside scale height (HT), transition height (hT), and their ratio (RT), as functions of the day-of-the- year, local time, geomagnetic latitude, solar flux F10.7 and Kp. Further, an analytical profiler, named TSMP was developed, which gives the shape of Ne profile above the F layer peak as a sum of O+ and H+ profiles, by using TSM topside parameters. When electron density NmF2 and height hmF2 are specified at the lower boundary, TSMP provides Ne profile up to GPS orbit heights. The later improvement of TSMP, namely TaD, reconstructs the topside Ne profile by using the actual (measured) NmF2, hmF2, and the scale height Hm from Digisonde sounders. TaD multiplies the Digisonde-derived scale height Hm with a predefined factor (approximately 2.5) and uses the modified scale height (2.5Hm) instead of HT. TaD uses a scale height Hp statistically derived from profiles measured in plasmasphere portion of the high-apogee ISIS-1 topside sounder. The final development of TaD is the procedure adjusting the model profile with measured collocated GNSS-TEC. This procedure varies HT until the integral of the model profile matches the measured TEC. TaD profiling accuracy was widely verified by comparing with measured profiles, ground based TEC, and PIM, NeQuick, and ISR models. TaD profiler has been implemented in European DIAS (Digital Upper Atmosphere Server) system. TaD was used to reconstruct the electron density profile from F layer peak up to the GNSS heights for each of the DIAS Digisonde stations. Then by using a spatial interpolation method, it produced instantaneous maps of each parameter involved in TaD calculations. This enabled obtaining 3D maps of electron density distribution in real time.

1 INTRODUCTION

Significant efforts have been made by the ionospheric community to support the GNSS practice developing high precision models able to provide, with the required accuracy, the electron density profile from the bottomside ionosphere up to the height of GNSS orbits, and it's integral which is known as the Total Electron Content (TEC). The current observing facilities are ionosondes, providing estimates of the electron density up to hmF2, Incoherent Scatter Radars (ISR) that cover the part of the profile up to 700 km, and satellites that use the Radio Occultation technique to reconstruct the electron density profile for the topside part of the

ionosphere. Except from ionosondes, none of the other observing techniques provide systematically measurements that can be exploited for monitoring purposes (Mikhailov et al., 2014). For this reason the scientific community has developed models that are able to predict the ED profile. These are of two basic categories: assimilation models (EDAM is a representative model, Angling and Jackson-Booth, 2011) and empirical models such as NeQuick (Radicella and Nava, 2010), and TaD (Kutiev et al., 2012).

The TaD model is a topside profiler based on empirical equations derived from topside sounding data of the Alouette/ISIS database and ingests the Digisonde observations at the height of the maximum electron density and the TEC parameters calculated from GNSS receivers at the Digisonde locations, to adjust the profiler with the real-time conditions of the ionosphere. The model has three components: a) the Topside Sounders Model (TSM) (Kutiev and Marinov, 2007; Kutiev et al. 2006) that provides the empirical functions for the O+- H+ transition height (hT), the topside electron density scale height (HT) and their ratio RT=HT/hT, derived solely from the Alouette/ISIS data; b) the Topside Sounders Model Profiler (Kutiev et al., 2009a, 2009b) that offers analytical formulas for obtaining the shape of the vertical plasma distribution in the topside ionosphere and plasmasphere based on TSM parameters and on the F layer maximum density (NmF2), its height (hmF2) and its scale height (Hm) at its lower boundary, derived from Digisondes. This profiler models separately the O+, H+, and He+ density distributions in transition region between topside F region and plasmasphere, extracted from the analysis of the electron density profiles from ISIS-1; c) the final TaD profiler that performs the necessary transformations to the Digisonde autoscaled scale height so that the integrated TSMP electron density from the F layer peak to GNSS orbits can be finally adjusted to the measured GNSS TEC at the Digisonde location (Belehaki et al., 2012, Kutiev et al., 2012).

2 TAD BACKGROUNDS

2.1 The Topside Sounders Model

(TSM) reproduce the O+- H+ (upper) transition height (hT) and the topside electron density scale height (HT), based on 172,622 measured Ne profiles by topside sounders on Alouette-1a, -1b, -1c and -2 and ISIS-1 and –2 satellites (Bilitza, 2001). The HT and hT models are represented by 5-dimensional polynomials expressing both quantities as functions of month of the year, geomagnetic latitude, local time, solar flux F107, geomagnetic index and Kp. Later, Kutiev and Marinov (2007) developed a model of the ratio RT = HT/hT, based on ratios of individual profiles and combined the three models into a single model named Topside Sounder Model (TSM). The key element in the modeling is the assumption that the lowest gradient on the topside Ne profile represents the altitude gradient of the O+ density profile. Assuming exponential distribution of O+ density, the transition height hT is found at the height, where the upward extrapolated O+ density becomes one half of the measured Ne density. The O+ gradient, inferred from the Ne profile is converted into scale height, e.g. the distance in km at which the O+ density changes e (Euler's number) times. Therefore, both HT and hT have the same dimension. TSM provides the topside F region scale height HT and transition height hT between O+ and H+ dominant regions, based on measured data only. As these parameters are intrinsic to plasma distribution in ionosphere and plasmasphere, they can be used in any model dealing with the plasma density structure. It has to be noted, that HT is a vertical scale height and differ from the theoretical plasma scale height defined along magnetic field lines (see Belehaki et al., 2006).

TSM approximates the individually extracted scale heights with a 5-dimensional polynomial, which consists of Tchebishev and trigonometric base functions. The same model is applied to the transition heights hT and their individual ratios RT. The average HT value over the whole dataset is 138 km with standard deviation of 54 km (or 39%). TSM reduces the standard deviation to 36 km (or the error to 26%). It is interesting to note that dispersion (25%) and model error (18%) of RT are considerable less than of the other two topside parameters.

2.2 Topside Sounder Model Profiler (TSMP)

Most recently, Kutiev et al. (2006) offered a method for obtaining the shape of the vertical plasma distribution in topside ionosphere and plasmasphere by introducing HT and hT parameters into three well known formulas describing the vertical plasma distribution: α-Chapman, Sech-squared, and Exponential (see Stankov et al., 2003). The analytical formulas containing HT and hT were named as Topside Sounder Model Profiler (TSMP). TSMP provides the shape of the vertical plasma distribution; to obtain the density distribution, it needs specifying

the F layer density (NmF2) and height hmF2 at its lower boundary. In recent development of TSMP (Kutiev et al., 2009a), the α-Chapman formula was used to describe O+ distribution, while H+ distribution was presented by exponential formula with scale height HH+=16HT. The present formulation of TSMP has the form:

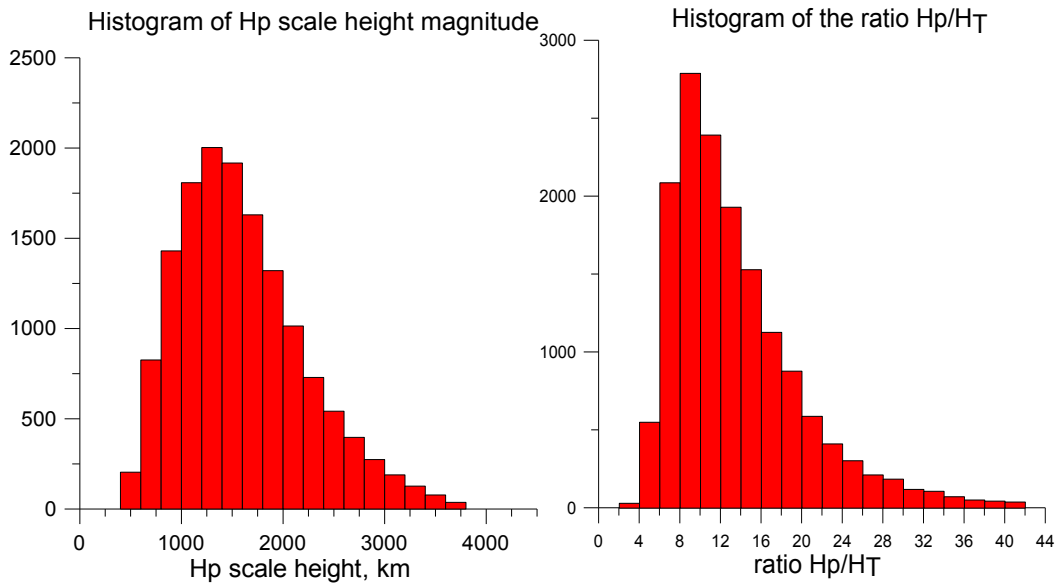

Figure 1: Histograms of a) Hp scale height; b) the ratio Hp/HT from ISIS-1 measured Ne profiles

$$Ne = N_0(h) + N_0(h_T)exp\left(-\frac{|h-h_T|}{Hp}\right) \quad (1)$$

where

$$N_0(h) = N_m exp\left\{\frac{1}{2}\left[1 - \frac{h-h_m}{H_{o^+}} - exp\left(-\frac{h-h_m}{H_{o^+}}\right)\right]\right\} \quad (2)$$

Here Ne is the electron density assumed to be equal to the sum of O+ and H+ densities (Ne = NO++ NH+) in all altitudes. NO+ is described by α-Chapman function, with a scale height HO+ being one half of HT, while NH+ is pure exponential function with a scale height HH+ denoted as Hp. Below hT, NH+ is forced to decrease by taking absolute difference |h-hT| in order to comply with the real distribution. Therefore, the maximum of NH+ distribution is fixed at transition height, although in reality it lies slightly above. At transition height, NH+ = NO+(hT) and scale the hydrogen ion distribution in plasmasphere. To calculate the topside density profile, TSMP needs values of NmF2 and hmF2 at the lower boundary (denoted as Nm and hm).

2.3 TSMP-assisted Digisonde profiler (TaD)

TSM provides another model quantity RT=HT/hT, not directly used in TSMP. The model ratio RT possess an important property: it can be used as a link between TSM parameters and another measured topside quantities. This property is used by Kutiev et al. (2009a) to link TSMP to Digisonde topside profiling technique. In TaD approach, the lower boundary values and the scale height are provided by Digisonde measurements.

Kutiev et al, (2009) developed a method that applies TSMP to EDP obtained by ground-based Digisonde sounders. Digisonde software (Reinisch and Huang, 2001) extends the measured bottomside profile in the topside by assuming α-Chapman shape with a scale height Hm obtained from the bottomside profile at the F layer peak hmF2. The scale height Hm is a neutral scale height, and the Digisonde α-

Chapman EDP well above hmF2 decreases upward with a gradient corresponding to a doubled Hm. Kutiev et al, (2009a) found that the doubled Hm is systematically lower than the TSM scale height HT by a factor of 1.25. In order to adjust TSMP to Digisonde measurements, Kutiev et al, (2009b) multiplied Hm by correction factor k = 2.5 and obtained the corresponding transition height hT through the ratio hT=kHm/RT, with the ratio RT taken from TSM. Having obtained the scale height HT = kHm and transition height hT, the new profiler named TaD (TSMP-assisted Digisonde Profiler) extends the measured bottomside EDP to the topside

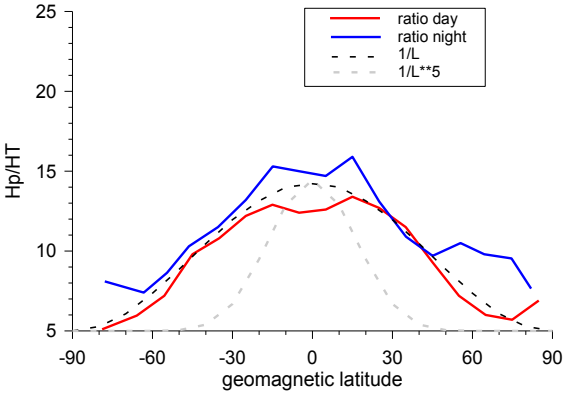

Figure 2: Average daytime (red - right) and nighttime (blue) variations of the ration Hp/H_T on geomagnetic latitude. Solid and grey dashed curves represent reversed invariant latitude 1/L and $1/L^5$ respectively.

F region and plasmasphere. It should be noted that while TSMP describes the shape of the topside EDP only, TaD provides EDP from hmF2 up to GPS orbit heights at Digisonde location.

2.4 Plasmasphere profile

Kutiev et al, (2009b) examined the H+ scale height by using ISIS-1 topside sounder profiles which extend up to 3500 km. The H+ scale height, denoted as plasmasphere scale height Hp, was extracted from ISIS-1 profiles as the largest gradient of the profiles above 2500 km, well above transition height. It was found that the ratio Hp/HT is close to 16 at equatorial and low latitudes, as it decreases significantly towards poles. Kutiev et al, (2009b) obtained a simple expression of the ratio depending linearly on squared cosine of geomagnetic latitude. In other words, the Hp/HT ratio follows strictly the shape of plasma pause.

Figure 1a shows a histogram of Hp values, accumulated from 14,628 measured profiles. The most probable Hp scale height value is around 1200 km. For TaD, more important parameter is the ratio of Hp and HT scale height, because the plasmaspheric scale height Hp is expressed as function of the F region scale height HT. Figure 1b shows a histogram of the bulk distribution of the ratio Hp/HT, the key parameter of plasmaspheric Ne profiling. The most probable value of the ratio surprisingly is not 16, but between 8 and 10. This fact, however, can be expected due to the lower plasma density in outer plasmasphere and magnetosphere. Figure 2 shows the average ratio for daytime (red line) and nighttime (blue line) conditions as a function of geomagnetic latitude. Vertical bars show doubled standard deviation for each 10-degree bin on latitude. The ratio Hp/HT has a maximum around equator (±30°) and marked decrease towards poles. Nighttime average ratio is slightly higher that daytime one, but local time dependence is not visible due to the large scatter of data. The daytime and nighttime variations of average curves are compared with 1/L (solid dashed) and 1/L5 (dashed gray) dependence. The scales of the latter curves are adjusted to fit average scale height ratios. While L=cos-2(glat) represents the length of the plasma flux tubes, L5 is proportional to the total volume of the respective flux tubes. Obviously, decrease of plasma density in equatorial plane is reversely proportional to L, not to the total volume of plasma tubes. Fortunately, the latitude variation of Hp/HT can easily be introduced in TaD by representing Hp as a function of geomagnetic latitude. We accept a simple relation Hp = HT(9cos2(glat)+4) to account for latitude changes of Hp.

2.5 Adjustment of TaD profile to GPS-TEC

Figure 3 illustrates the difference between Digisonde and TaD EDPs. Digisonde profile (red curve) is obtained from Ebro ionosonde station at 07:00 UT on 5 June 2001. Digisonde scale height Hm = 49.8 km, NmF2 = 1.0x106 cm-3 , and hmF2 = 284.3 km. The figure shows O+ and H+ profiles, which compose TaD EDP. TaD topside scale height HT = 124.5 km, Hp = 1490 km, and transition height hT = 825 km. The correction factor k, which converts Hm into HT is statistically obtained by comparing Digisonde data with corresponding TSM product). Although it assures a statistical reliability of TaD profiles, it cannot guarantee reliable reconstruction of EDP in all individual cases. One way to improve the accuracy of TaD profiling is to compare the EDP integral (bottomside + topside profiles) with GNSS-derived

total electron content (TEC GNSS), obtained at the location of the ionosonde. By varying the TaD parameters, we can be able to adjust EDP integral to TEC (GNSS) values (Kutiev et al, 2012).
The profile shape is most sensitive to the changes of topside scale height HT, respectively to correction factor k. We prepared a procedure, in which we vary subsequently EDP parameters k, Hm, hT, and Hp and calculate at each step the difference dTEC between the integral of TaD profile and TEC(GNSS).

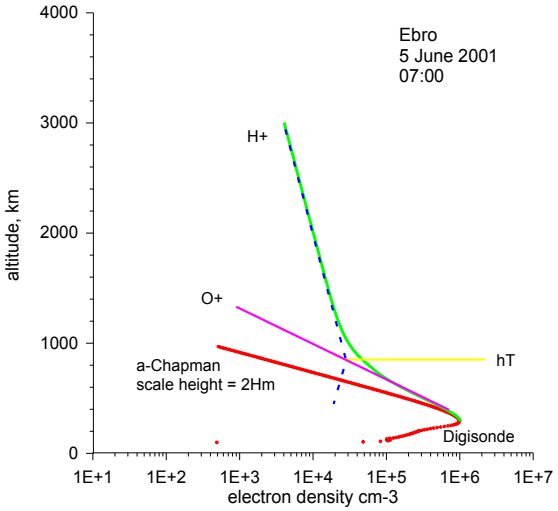

Figure 3: Reconstructed Ne profile over Ebro Digisonde station at 07:00 UT on 5 June 2001. Red curve is provided by Digisonde software, green curve represents TaD profile with its O^+ (pink curve) and H^+ (blue dashed curve) components.

Bottomside profiles provided by Digisonde software are added to TaD integral. Figure 4a shows as a sample the difference dTEC = TEC(TaD) – TEC(GNSS) obtained by varying the correction factor k. It this sample dTEC becomes zero at k = 3.3, denoted as k0. As can be expected, TEC(TaD) is lower than TEC(GNSS) for smaller k values and grows as k increases. It is a common feature of the adjustment procedure and dTEC depends linearly on k around ko. Figure 4b shows part of the profiles with default value 2.5 (no adjustment - blue curve) and k0 = 3.3 (with adjustment -red curve) for the same case as in Figure 4a. Note that the change of correction factor k changes also transition height hT and plasmasphere scale height Hp.

3 VERIFICATION OF TAD

3.1 Comparison with data

TaD EDPs were widely verified with all available measured profiles and those extracted from another measurements. Belehaki et al, (2009) summarized comparison of TaD profiles with CHAMP reconstructed profiles, ground-based GPS-derived TEC, Incoherent Scatter Radar (ISR) profiles at Malvern, UK, and with EDP obtained by Radio Plasma Imager (RPI) onboard IMAGE satellite.

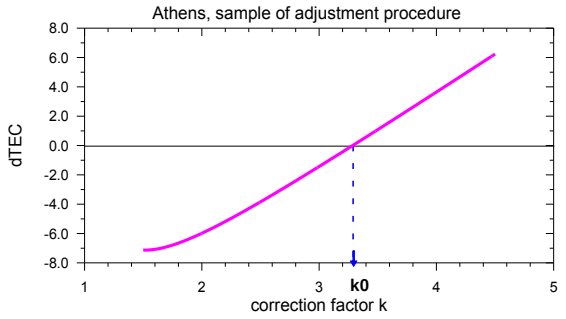

Figure 4a: The difference dTEC between TEC(TaD) and TEC(GNSS) as a function of correction factor k. The value k0 is the adjusted value for further calculations.

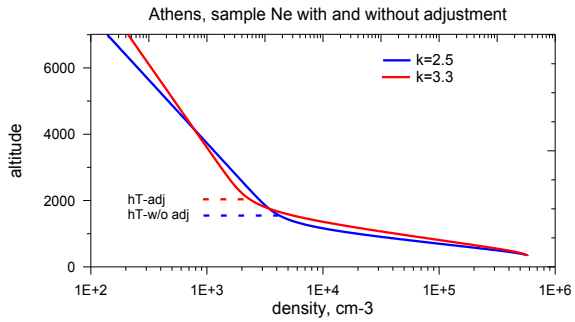

Figure 4b: Part of the reconstructed Ne profile with the use of default value of k=2.5 (blue curve –on top is at left) and that with k0=3.3 (red curve - on top is at right

Statistically sufficient comparison with GNSS-derived TEC showed an average model error of 1.92 TEC units (TECU) for Athens and 1.0 TECU for Juliusruh data with standard deviation of 5.2 and 2.9 respectively. By our knowledge, such a comparison between a reconstruction model of Ne and independent TEC measurements is unique in the literature. We consider the above cited figures acceptable, providing strong evidence for the reliability of TaD approach.

3.2 Comparison with models

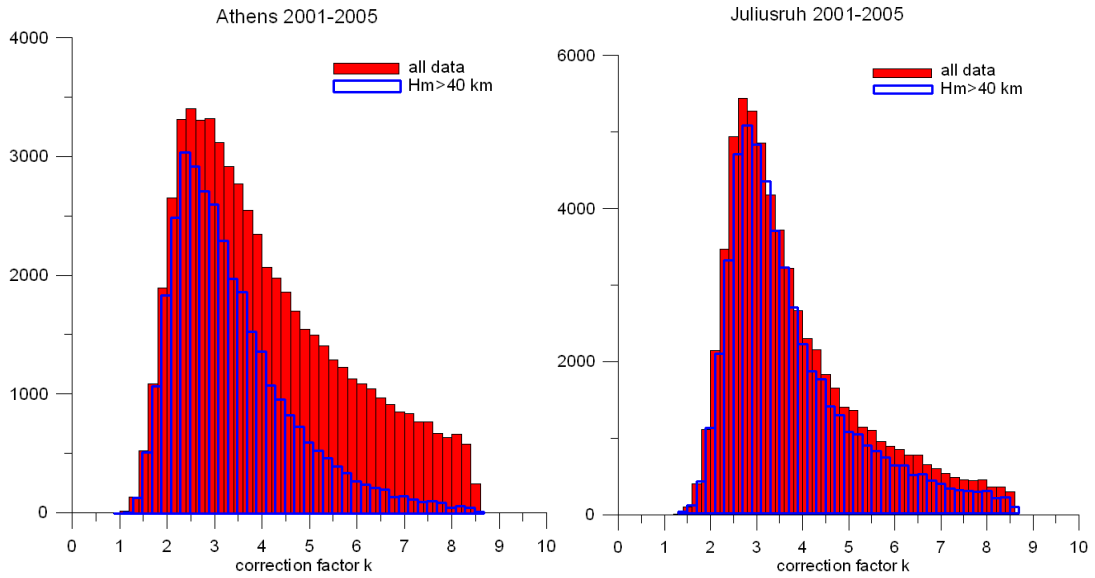

Figure 5: Adjustment procedure was applied to the hourly Digisonde profiles obtained at Athens and Juliusruh in the 6 years period 2001-2005. Histograms of the correction factor k are given separately for all Hm values (red bars) and for those greater than 40 km (open blue bars).

Stankov et al. (2007) compared the ionospheric scale height and transition height from TSM with those from two other well-known models – the NeQuick Model (NeQ- Hochegger et al. 2000) and the Parameterized Ionospheric Model (PIM- Daniell et al. 1995).

The topside ionospheric scale height HT and transition height hT have been extracted from the model profiles in the same manner as it was previously done for the topside sounder measurements.

Comparison showed that the three models rarely were in full agreement. In many cases, large discrepancies were found in both local time and seasonal variations. Analysis showed that there were some deficiencies in NeQuick and PIM formulations, particularly in the cases of observed extremely large discrepancies

Important verification of TaD model parameters was made by its comparison with IRS (Incoherent Scatter Radar) model (Holt et al. 2002, Zhang et al. 2004). The Topside Sounder Model (TSM) provides directly the scale height (HT), while the Incoherent Scatter Radar (ISR) model provides electron density profiles and its scale height (HR) was determined by the same manner as at NeQuick and PIM. HR was calculated at 7 ISR locations for fixed values of day-of-year (DoY), local time (LT), solar flux F10.7, and geomagnetic index ap and corresponding TSM HT was attached for the same conditions. Comparison revealed that HT values were systematically lower than respective HR values, as the average offset for all 7 stations is 55 km. For the midlatitude stations Arecibo (AR), Shimazaki (MU), and Millstone Hill (MH), this difference was reduced to 43 km. The range of variations of HR was much larger than that of HT, as the HT range overlapped the lower part of the HR range. Dependences on ap, (DoY) and LT are much stronger in the ISR model than in TSM. This resulted in much larger values of HR at higher ap. Diurnal amplitude of HR was much larger than that of HT, with large maximum at night. This comparison yielded to the conclusion that the ISR measuring technique provides steeper topside Ne profiles than that provided by the topside sounders.

The overall statistics is shown in Figure 5. The histogram of TSM HT is shown by the red bars, while the scale height from ISR profiles (HR) is given by the open blue bars. The average HT = 127 km with standard deviation sd = 30 km and average HR = 182 km with sd = 73 km. It has to be noted that HT and HR distributions shown in the histograms differ from the normal distribution due to their high value tails. The averages and standard deviations given in the text

refer to the corresponding normal distribution and should be considered as rough characteristics of the scale height distributions. Obviously, the average values do not match the maximums of the histograms and they may differ considerably.

3.3 TaD implementation in European DIAS system

To better characterize the ionosphere and forecast its disturbances over Europe, a data and model infrastructure platform called the European Digital Upper Atmosphere Server (DIAS) has been established in the National Observatory of Athens by a European consortium formed around eight ionospheric

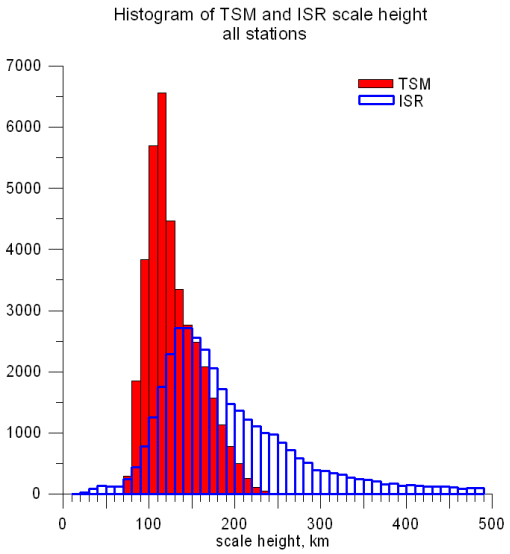

Figure 6: Histograms of scale heights H_R (open blue bars) and corresponding H_T (red bars) for all 7 ISR stations.

stations, and funded by the European Commission (Belehaki et al. 2005). The DIAS system (http://dias.iono.noa.gr) operates since 2006 and the basic products that are delivered are real-time and historical ionograms from all DIAS ionospheric stations with the results of the automatic scaling archived in SAO format, frequency plots and maps of the ionosphere over Europe based on the foF2, M(3000)F2, MUF and electron density parameters, as well as long term and short term forecasting up to 24 hour ahead (Belehaki et al., 2005; 2006a; 2007).
One of requirements of European Space Agency (ESA) for the European Ionosonde Service was the development of a procedure that calculates independently TEC maps based on ionosonde data only. To satisfy this request, Belehaki et al. (2014) use TaD to reconstruct the electron density profile from F layer peak up to the GNSS heights for each of the DIAS Digisonde stations. Then by using a special interpolation procedure, we produce instantaneous maps (further denoted as lat/long maps) of each parameter involved in TaD calculations. Maximum available stations of DIAS are 8, but frequently their number is less. For this set of stations, we take the geographic region confined in (-10°, 40°)E and (35°, 55°)N. Location of the 8 stations are marked by blue crosses in Figure 6. One station (Moscow) lays bit outside the area, but its data are included in calculation of maps. Figure 6 represents the distribution of the Digisonde-derived scale height Hm with the color-coded scale on the right. When the TaD parameter values are specified at any arbitrary location within the map, EDP profile is straight forward calculated. In this scheme, TaD model is run each time when the whole EDP or even the electron density at any single fixed height is needed.

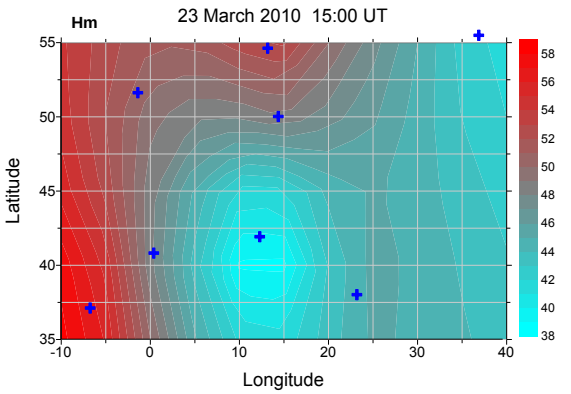

Figure 7: Instantaneous map (lat/long map) of the Digisonde-derived scale height Hm involved in TaD calculations. For this set of stations, we take the geographic region confined in (-10°, 40°)E and (35°, 55°)N. Location of the 8 DIAS stations are marked by blue crosses. One station (Moscow) lays bit outside the area, but its data are included in calculation of maps. The color-coded scale is shown on the right.

The TaD set of subroutines has been implemented in DIAS backend to provide maps of the electron density exploiting data streaming from the DIAS Digisondes in real-time. Operationally, the implemented code calculates first the maps of Hm, hmF2 and foF2 based on the available Digisonde data and TSM derivatives hT and Hp, applying the polynomial curve fitting for the mapping procedure. Then TaD code reconstructs the three-dimensional map of the electron density distribution (3D-EDD). Finally, the code adjusts the profiles with the TEC (GNSS) parameters at the points where Digisonde

measurements are available, and recalculates the 3D-EDD maps.

It is important to estimate the impact of the mapping procedure performance to the overall result. The weighted polynomial (Polyweight) procedure applied here, is a spatial interpolation method and can produce maps over any randomly spaced data, by calculating first values at the grid nodes (1˚x1˚ geographic coordinates) and then interpolates values between grid nodes by using a cubic interpolation method. Therefore, an important point is the dependence of the accuracy of the predictions on the number of stations contributing with data for the calculation of each map. Systematic comparisons are performed between the TaD (TEC) maps and the TEC (GNSS) maps provided by Royal Observatory

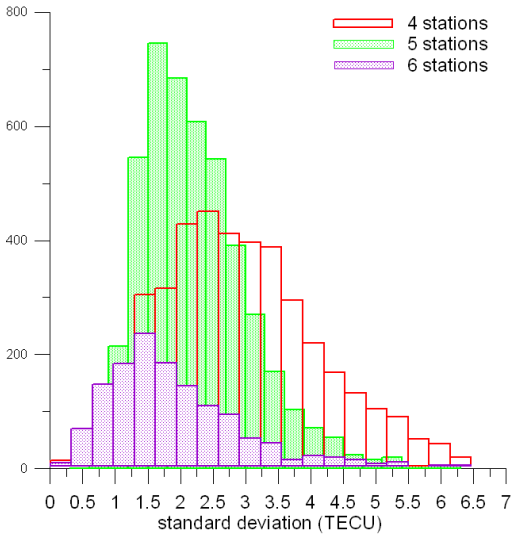

Figure 8: Histograms of standard deviation between TaD and GNSS maps produced in years 2000-2002. Histograms are given separately depending on the number of DIAS stations available for comparison.

of Belgium (ROB) (Bergeot et al, http://gnss.be/Atmospheric_Maps/ionospheric_maps.php). The ROB maps are produced by using 90-100 data points, while TaD maps are based on 4 - 8 data points provided by the available at the moments Digisonde stations between 2000 and 2002 years.. Comparison is aimed to give an estimate to what extent the TaD maps deviate from routine GNSS TEC maps. Distribution of standard deviation is given in a histogram format for three sets of available DIAS stations in Figure 8. The figure provides an evidence of the accuracy of TaD mapping depending on the number of contributing stations. Based on the above results, it is obvious that the number of contributing stations affect largely the performance of the mapping routine. As expected, the standard deviation between the TaD and GNSS TEC maps is almost doubled when the number of stations decreases from 6 to 4. Consequently the number of contributing stations is an important information and therefore it is provided to the user as a performance indicator for this product.

4 CONCLUSION AND FUTURE DEVELOPMENT

TaD reconstruction model is a reliable instrument for obtaining real-time vertical ED profiles up to GNSS orbit heights over Digisonde stations and, by applying the spatial interpolation technique, for producing 3D EDD over any area of interest. TaD profiling was extensively verified and validated by practically all available independent data and models and the overall model error is around 3 TECU, comparable with TEC measuring accuracy. TaD was implemented in European DIAS system and provides in near real time 3D EDD maps of the European area.

The plans are to increase the accuracy of TaD mapping technique by increasing the number of data points, having them at each grid node. For this purpose, we have to reverse the calculation scheme starting with GNSS-TEC maps (e.g. height integral of TaD profile) and then adjusting TaD profile parameters to its integral. The increased accuracy of the 3D maps will allow sensing the small changes in ionosphere invoked by the Large Scale Traveling Ionospheric Disturbances (LSTIDs). The latter, due to their sharp horizontal gradients, are able to produce large errors in GNSS positioning accuracy.

REFERENCES

Angling, M. J., and N. Jackson-Booth, 2011. *A short note on the assimilation of collocated and concurrent GPS and ionosonde data into the Electron Density Assimilative Model*, Radio Sci, 46, doi:10.1029/2010RS004566.

Belehaki A., Lj. Cander, B. Zolesi, J. Bremer, C. Juren, I. Stanislawska, D. Dialetis and M. Hatzopoulos, 2006a. *Monitoring and forecasting the ionosphere over Europe:* The DIAS project, Space Weather, 4, S12002, doi:10.1029/2006SW000270.

Belehaki, A., I. Kutiev, B. Reinisch, N. Jakowski, P. Marinov, I. Galkin, C. Mayer, I. Tsagouri, and T. Herekakis, 2009. *Verification of the TSMP-assisted Digisonde (TaD) topside profiling technique*, Acta Geophysica, 58, 3, 432-452.

Belehaki, A., I. Tsagouri, I. Kutiev, P. Marinov, and S. Fidanova, 2012. *Upgrades to the Topside Sounders*

Model assisted by Digisonde (TaD) and its validation at the topside ionosphere, J. Space Weather Space Clim., 2, A20, DOI: http://dx.doi.org/10.1051/swsc/2012020.

Belehaki, A., L. Cander, B. Zolesi, J. Bremer, C. Juren, I. Stanislawska, D. Dialetis, M. Hatzopoulos, 2005. "*DIAS Project: The establishment of a European digital upper atmosphere server*", Journal of Atmospheric and Solar-Terrestrial Physics, 67, pp. 1092-1099,

Belehaki, A., Lj. Cander, B. Zolesi, J. Bremer, C. Juren, I. Stanislawska, D. Dialetis and M. Hatzopoulos, 2007. *Ionospheric specification and forecasting based on observations from European ionosondes participating in DIAS project*, Acta Geophysica, Volume 55, 3, doi: 10.2478/s11600-007-0010-x, pp 398-409.

Belehaki, A., P. Marinov, I. Kutiev, N. Jakowski, S. Stankov, 2006b. *Comparison of the topside ionosphere scale height determined by topside sounders model and bottomside digisonde profiles*, Advances in Space Research 37, 963–966.

Belehaki A., I. Tsagouri, I. Kutiev, P. Marinov, B. Zolesi, M.Pietrella, K. Themelis, P. Elias, and K. Tziotziou, 2014. *The European Ionosonde Service: nowcasting and forecasting ionospheric conditions over Europe for the ESA Space Situational Awareness services*, J. Space Weather Space Clim.,. (to be submitted).

Bilitza, D, 2001. *International Reference Ionosphere (IRI)–Task Force Activity Report 2000*, IRI News, 8, 1/2, 8-15,

Kutiev I., P. Marinov, A. Belehaki, and B. Reinisch, N. Jakowski, 2009a. *Reconstruction of topside density profile by using the Topside Sounder Model Profiler and Digisonde data*, Adv. Space Res., 43, 1683-1687.

Kutiev I., P. Marinov, A. Belehaki, N. Jakowski, B. Reinisch, C. Mayer, and I. Tsagouri, 2009b. *Plasmaspheric electron density reconstruction based on the Topside Sounder Model Profiler*, Acta Geophysica, 58, 3, 420-431.

Kutiev, I., P. Marinov, , S.Watanabe, 2006. *Model of the topside ionosphere scale height based on topside sounder data*, Advances in Space Research, 37, 5, 943-950.

Kutiev, I., P. Marinov, S. Fidanova, A. Belehaki and I. Tsagouri, 2012. *Adjustments of the TaD electron density reconstruction model with GNSS TEC parameters for operational application purposes*, J. Space Weather Space Clim. 2 A21, DOI: http://dx.doi.org/10.1051/swsc/2012021

Kutiev, I., P. Marinov, 2007. *Topside sounder model of scale height and transition height characteristics of the ionosphere*, Advances in Space Research, 39, 759–766.

Mikhailov, A. V., A. Belehaki, L. Perrone, B. Zolesi and I. Tsagouri, 2014. *On the possible use of radio occultation middle latitude electron density profiles to retrieve thermospheric parameters*, J. Space Weather Space.Clim. 4 A12, DOI: http://dx.doi.org/10.1051/swsc/2014009.

Radicella, S., and B. Nava, 2010. *NeQuick model: Origin and evolution, in Antennas Propagation and EM Theory (ISAPE)*, 2010 9th International Symposium on, edited, pp. 422-425.

Stankov, S., P. Marinov, I. Kutiev, 2007. *Comparison of NeQuick, PIM, and TSM model results for the topside ionospheric plasma scale and transition heights*, Adv. in Space Res. 39, 767– 773.

Stankov, S., N. Jakowski, S. Heise, P. Muhtarov, I. Kutiev, R. Warnant, 2003. *A new method for reconstruction of the vertical electron density distribution in the upper ionosphere and plasmasphere* , J. Geophys. Res., 108(A5), 1164. doi.10.1029/2002JA009570.

Zhang, S.-R., J. M. Holt, A. M. Zalucha, and C. Amory-Mazaudier, 2004. *Mid-latitude ionospheric plasma temperature climatology and empirical model based on Saint Santin incoherent scatter radar data from* 1966 – 1987, J. Geophys. Res., 109, A11311. doi:10.1029/ 2004JA010709.

Holt, J. M., S.-R. Zhang, and M. J. Buonsanto, 2002. *Regional and local ionospheric models based on Millstone Hill incoherent scatter radar data*, Geophys. Res. Lett., 29(8), 1207. doi:10.1029/2002GL014678.

Daniell, R.E., Brown, L.D., Anderson, D.N., Fox, M.W., Doherty, P.H., Decker, D.T., Sojka, J.J., Schunk, R.W. 1995. *Parameterized ionospheric model: a global ionospheric parameterization based on first principles models.* Radio Sci. 30, 1499–1510.

Hochegger, G., Nava, B., Radicella, S.M., Leitinger, R., 2000. *A family of ionospheric models for different uses.* Phys. Chem. Earth 25 (4), 307–310.

Reinisch, B.W. and X. Huang, 2001. *Deducing topside profiles and total electron content from bottomside ionograms*, Adv. Space Res., 27, (1), 23-30.

TOWARDS ASYMPTOTIC STATISTICAL ALGORITHMS IN INTELLIGENT TELECOMMUNICATIONS

Blagovest Shishkov
Institute of Mathematics and Informatics – BAS
bshishkov@math.bas.bg

Keywords: Telecommunications; Asymptotic Optimal (AO) Algorithms; Robust Statistics; Adaptive Systems.

Abstract: When receiving signals, their adequate processing is of crucial importance, as an important challenge in current Telecommunications. Statistical Algorithms (including ones that rely on learning samples) play a role not only in extracting the useful signal (getting rid of the noise) but also in the decision-making process that follows Further, it is claimed that basing such algorithms on the Large Sample Theory, would bring in more reliable results. In such cases, we consider Asymptotic Statistical Algorithms and it is not surprising that such algorithms have been largely applied in Telecommunications for decades already. Nevertheless, applying Asymptotic Statistical Algorithms in adaptive telecommunication systems is not trivial because of more sophisticated samples-related procedures to be considered. In the current paper, we address the mentioned problem, by applying robust algorithms in condition of prior uncertainty. We partially validate the applicability of the proposed approach, by means of examples. The remaining of the paper is organized as follows: In Section 2, we provide relevant state-of-the art information that concerns Statistical Algorithms, in general, and Asymptotic Statistical Algorithms, in particular. In Section 3, we present our proposed approach, in the form of a set of guidelines and application directions. We then reflect this in illustrative examples in Section 4. Finally, Section 5 contains the conclusions.

1 INTRODUCTION

When receiving signals, their adequate processing is of crucial importance, as an important challenge in current Telecommunications. Statistical Algorithms (including ones that rely on learning samples) play a role not only in extracting the useful signal (getting rid of the noise) but also in the decision-making process that follows and in de-coding the signal (hence, the role of Statistical Algorithms also in transmitting the signal is to be mentioned, especially as far as the signal coding is concerned).

Further, it is claimed that basing such algorithms on the Large Sample Theory, would bring in more reliable results. In such cases, we consider Asymptotic Statistical Algorithms and it is not surprising that such algorithms have been largely applied in Telecommunications for decades already.

Nevertheless, applying Asymptotic Statistical Algorithms in adaptive telecommunication systems is not trivial because of more sophisticated samples-related procedures to be considered.

In the current paper, we address the mentioned problem, by applying robust algorithms in condition of prior uncertainty. We partially validate the applicability of the proposed approach, by means of examples.

The remaining of the paper is organized as follows: In Section 2, we provide relevant state-of-the art information that concerns Bayesian tests (for cases of finite samples). In Section 3, we address Statistical Algorithms, in general, and Asymptotic Statistical Algorithms, in particular, proposing applications in telecommunications. We then reflect this in illustrative examples in Section 4. Finally, Section 5 contains the conclusions.

2 OPTIMUM BAYESIAN TESTS FOR TESTING HYPOTHESES

Let us consider the construction and practical use of optimum Bayesian tests for testing the hypotheses

$H_0 : \boldsymbol{\theta} = \boldsymbol{\theta}_0$ against the class of arbitrary alternatives

$$H_1: \boldsymbol{\theta} \neq \boldsymbol{\theta}_0 \in \boldsymbol{\theta} \tag{1}$$

, in which *a prior* distribution P(**θ**) is specified

$$\Phi^B(\mathbf{x}) = \begin{cases} 1, & if\ T(\mathbf{x}) \geq c_\alpha \\ 0, & if\ T(\mathbf{x}) < c_\alpha \end{cases}$$

$$T(\mathbf{x}) = \int_{\boldsymbol{\Theta}} \frac{p(\mathbf{x}, \boldsymbol{\theta})}{p(\mathbf{x}, \boldsymbol{\theta}_0)} dP(\boldsymbol{\theta}) \tag{2}$$

$$\hat{\boldsymbol{\theta}}_{ML}(\mathbf{x}) = \arg\max_{\boldsymbol{\theta} \in \boldsymbol{\Theta}} p(\mathbf{x}, \boldsymbol{\theta})$$

Definition: According to [Le Cam, Roussas,], the family of distributions $\{p(\mathbf{x}, \boldsymbol{\theta},\ \boldsymbol{\theta} \in \boldsymbol{\Theta}\}$ is called LAN at the point $\boldsymbol{\theta}_0$ if the likelihood ratio (LR) for the close hypotheses

$H_0: \boldsymbol{\theta} = \boldsymbol{\theta}_0$ and $H_1: \boldsymbol{\theta} = \boldsymbol{\theta}_0 + \mathbf{h} n^{-1/2}$, $0 < \mathbf{h} < c$

$$\frac{p\left(\mathbf{x}, \boldsymbol{\theta}_0 + n^{-\frac{1}{2}}\mathbf{h}\right)}{p(\mathbf{x}, \boldsymbol{\theta}_0)} = exp\left\{-\mathbf{h}^T \Delta(\mathbf{x}, \boldsymbol{\theta}_0) + \frac{1}{2}\mathbf{h}^T \Gamma(\boldsymbol{\theta}_0)\mathbf{h} + \alpha_n(\mathbf{x}, \boldsymbol{\theta}_0, \mathbf{h})\right\} \tag{3}$$

3 ASYMPTOTIC OPTIMAL ALGORITHMS

3.1 Non-Gaussian Time Series.

The optimum statistical analysis of non-Gaussian time series is difficult in the sense that even if only the average and covariance function (or spectrum) of such a time series depends on the parameter **θ**, in the general case no explicit expression exists for the distribution density *p*(**x**, **θ**) of the observations, which could be analysed in order to establish the LAN conditions and to isolate simple forms of the asymptotically sufficient statistic and the Fisher information matrix. At the present time the LAN property of the observation distribution has been proved only for one general model of stationary non-Gaussian time series. This is the model of an ***m*-connected Markov sequence**, for which the joint observation distribution density is

$$p\left(\mathbf{x}; n^{-\frac{1}{2}}\gamma \mathbf{s}\right) = p\left(\mathbf{x}_1^{\boldsymbol{n}}; \gamma n^{-\frac{1}{2}} \mathbf{s}_1^m\right) \prod_{i=m+1}^{n} p\left(x_i \left| \mathbf{x}_{i-m}^{i-1}; \gamma n^{-\frac{1}{2}} \mathbf{s}_{i-m}^{i}\right.\right) \tag{4}$$

$$p(\mathbf{x}; \boldsymbol{\theta}) = p(\mathbf{x}_1^m; \boldsymbol{\theta}_m) \prod_{i=m+1}^{n} p\left(x_i | \mathbf{x}_{i-m}^{i-1}; \boldsymbol{\theta}_{m-1}\right) \tag{5}$$

$$\mathbf{s} = (s_1, \dots, s_n)^T, \quad \mathbf{x}_{i-m}^{i-1} = (s_{i-m}, \dots, s_{i-1})^T \tag{6}$$

$$\mathbf{z}^T = \left(y_{-m,\dots,y-1}, x\right) = (\mathbf{y}^T, x) \tag{7}$$

$$\boldsymbol{\theta}^T = \boldsymbol{\theta}_z^T = \left[\boldsymbol{\theta}_y^x\right]^T = \left(\boldsymbol{\theta}_y^T, \theta_x\right), \quad \boldsymbol{\theta} \in \Theta \subset R^{m+1} \tag{8}$$

$$p(x|\mathbf{y}; \boldsymbol{\theta}) = p(x|\mathbf{y}; \mathbf{0})[1 + \boldsymbol{\theta}^T \boldsymbol{\varphi}(\mathbf{z}) + |\boldsymbol{\theta}|^2 \delta(\mathbf{z}; \boldsymbol{\theta})] \tag{9}$$

$$\boldsymbol{\varphi}^T(\mathbf{z}) = [\phi_{-m}(\mathbf{z}), \dots, \phi_0(\mathbf{z})] \tag{10}$$

$$\boldsymbol{\varphi}^T(\mathbf{z}) = \frac{\partial}{\partial \boldsymbol{\theta}} \log p\,(x|\mathbf{y}; \boldsymbol{\theta})|_{\,\theta=0} = \begin{pmatrix} \frac{\partial}{\partial \theta_{y-m}} \log p(x|\mathbf{y}; \boldsymbol{\theta})|_{\,\theta=0}, \dots, \\ \frac{\partial}{\partial \theta_x} \log p(x|\mathbf{y}; \boldsymbol{\theta})|_{\,\theta=0} \end{pmatrix} \tag{11}$$

$$E\{\delta^2(\mathbf{z}; \boldsymbol{\theta})|\, H_0\} < D; \quad |\boldsymbol{\theta}| < B; \quad E\{\boldsymbol{\varphi}(\boldsymbol{z})|\, H_0\} = \mathbf{0} \tag{12}$$

$$E\{\boldsymbol{\varphi}(\boldsymbol{z})\boldsymbol{\varphi}^{\boldsymbol{T}}(\boldsymbol{z})|\, H_0\} = \mathbf{K}, \quad \det\mathbf{K} < \infty \tag{13}$$

Theorem 1. For the stated conditions the logarithm of the likelihood ratio permits the following asymptotic expansion

$$\begin{aligned}&\log l\left(\mathbf{x}; n^{-\frac{1}{2}}\gamma\mathbf{s}\right)\\&= \gamma n^{-\frac{1}{2}} \sum_{i=m+1}^{n} \left[\mathbf{s}_{i-m}^{i}\right]^{T} \boldsymbol{\varphi}\left(x_{i-m}^{i}\right)\\&-\frac{\gamma^2}{2} tr(\mathbf{SK}) + \alpha_n\left(\mathbf{x}; n^{-\frac{1}{2}}\gamma\mathbf{s}\right)\end{aligned} \tag{14}$$

$$\begin{aligned}&\boldsymbol{\varphi}^{T}\left(\mathbf{X}_{i-m}^{i}\right)\\&= \left[\phi_{-\boldsymbol{m}}\left(\mathbf{X}_{i-m}^{i}\right), \dots, \phi_0\left(\mathbf{X}_{i-m}^{i}\right)\right]\end{aligned} \tag{15}$$

$$\begin{aligned}&\phi_j\left(\mathbf{X}_{i-m}^{i}\right)\\&= \frac{\partial}{\partial\theta_{i+j}} \log p\left(x_i \middle| \mathbf{x}_{i-m}^{i-1}; \boldsymbol{\theta}_{i-m}^{i}\right)\Big|_{\theta_{i-\boldsymbol{m}}^{i}=0},\\&j = \overline{-m, 0}\end{aligned} \tag{16}$$

$$\begin{aligned}&\boldsymbol{K} = \left(K_{j\nu}\right) = \left(E_0\{\phi_j\phi_\nu\}\right), \quad j, \nu = \overline{-m, 0}\\&det\boldsymbol{K} < \infty\end{aligned} \tag{17}$$

$$\begin{aligned}&\mathbf{S} = \left(S_{j\nu}\right)\\&= \lim_{n\to\infty}\frac{1}{n}\sum_{i=m+1}^{n}\left[\mathbf{s}_{i-m}^{i}\right]\left[\mathbf{s}_{i-m}^{i}\right]^{T}\\&= \left(\lim_{n\to\infty}\frac{1}{n}\sum_{i=m+1}^{n}\mathbf{s}_{i+j}\,\mathbf{s}_{i+\nu}\right)\\&j, \nu = \overline{-m, 0} \qquad det\boldsymbol{S} < \infty\end{aligned} \tag{18}$$

Theorem 2 The asymptotically sufficient statistic

$$\begin{aligned}&n^{-\frac{1}{2}}\sum_{i=m+1}^{n}\mathbf{s}_{i-m}^{i}{}^{T}\boldsymbol{\varphi}\left(\mathbf{x}_{i-\boldsymbol{m}}^{i}\right)\\&= n^{-\frac{1}{2}}\sum_{i=m+1}^{n}\sum_{j=-m}^{0} s_{i+j}\,\boldsymbol{\phi_j}\left(\mathbf{x}_{i-m}^{i}\right)\end{aligned} \tag{19}$$

is an asymptotically normal random quantity with the parameters $N(0,tr(\mathbf{SK}))$ for the hypothesis H_0 and with the parameters $N(\gamma tr(\mathbf{SK}), tr(\mathbf{SK}))$ for the alternative H_1

3.2 Adaptive AO Algorithm for Detecting Signals in Auto-Regressive (AR) Interference Background

Let us consider the detection of a deterministic signal in a background of m-connected Markov interference. The problem consists of testing the hypothesis H_0 with regard to whether the sample $\mathbf{x}_n=(x_1,\dots,x_n)$ belongs to the distribution $p(\mathbf{x}_n;\mathbf{0})$ as opposed to the alternative H_1 that it belongs to the distribution $p(\mathbf{x}_n; \lambda_n \mathbf{s}_n)$ Here $\lambda_n = \gamma n^{-1/2}$ is the signal amplitude. An AO algorithm can be constructed on the basis of the previous statistic. Let us assume the sequence of additive Markov interference N_i , $i \in Z$ satisfies the AR equation with unknown coefficient:

$$\sum_{j=-m}^{0} a_j N_{i+j} = \eta_i\,, \quad i = \overline{1, n} \tag{20}$$

where a_j are constants and η_i are independent and identically distributed random quantities with the probability density

$$\begin{aligned}&p\left(x_i \middle| \mathbf{x}_{i-m}^{i-1}; \lambda_n \mathbf{s}_{i-m}^{i}\right)\\&= p_\eta\left(x_i + \textstyle\sum_{j=-m}^{-1} a_l\, x_{i+j} -\right.\\&\left.\lambda_n \textstyle\sum_{j=-m}^{-1} a_l\, x_{i+j}\right), \quad a_0\,,\end{aligned} \tag{21}$$

Consequently, the logarithmic derivative $\varphi_j\left(\mathbf{x}_{i-m}^{i}\right)$ can be represented as follows

$$\begin{aligned}&\varphi_j\left(\mathbf{x}_{i-m}^{i}\right)\\&= \frac{\partial}{\partial\theta_{i+j}} \log p\left(x_i \middle| \mathbf{x}_{i-m}^{i-1}; \boldsymbol{\theta}_{i-m}^{i}\right)\Big|_{\theta_{i-m}^{i}=0}\\&= -a_j \frac{p_\eta'\left(x_i + \sum_{j=-m}^{-1} a_j x_{i+j}\right)}{p_\eta\left(x_i + \sum_{j=-m}^{-1} a_j x_{i+j}\right)},\\&j = \overline{-m, 0}\end{aligned} \tag{22}$$

If the coefficients a_j re unknown, then one can find maximum likelihood estimates of them using the learning sample of AR interference $\{N_i\}$ and ,

consequently, the estimate $\hat{\varphi}_j(\mathbf{x}_{i-m}^i)$ of the logarithmic derivative. In this case the algorithm

$$\Phi(\mathbf{x}) = \begin{cases} 1, & (signal)\ if\ T(\mathbf{x}) \geq \hat{C}_\alpha \\ 0, & (no\ signal)\ if\ T(\mathbf{x}) < \hat{C}_\alpha \end{cases} \qquad (23)$$

$$T(\mathbf{x}) = n^{-\frac{1}{2}} \sum_{i=m+1}^{n} \mathbf{s}_{i-m}^{iT}\, \hat{\boldsymbol{\varphi}}(\mathbf{X}_{i-m}^i)$$

is the adaptive AO algorithm for detecting signals in an interference background

3.3 Communication systems

Figure 1 is depicted the structure of the detector for a narrow band modulated signal.

DL-delay line; SQ-squared; TD-threshold device

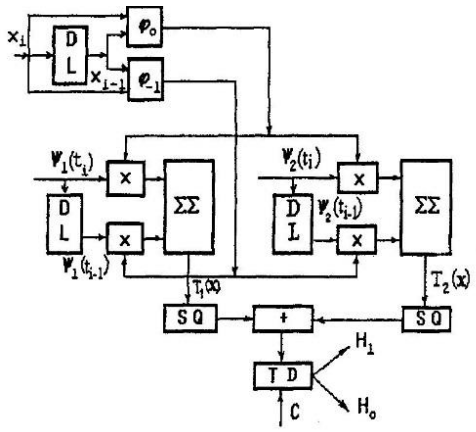

Figure 1: Structure of the detector for a narrow band modulated signal.

The basic algorithm (23) is interpreted, when m=1-Markov noise with unknown densities, and the useful signal is a deterministic one-a narrow band one (with an initial random phase φ_0) that is modulated by amplitude and by phase (frequency):

$$s(t) = a(t)\cos[\omega_0 t + \mu(t) - \varphi_0] = \nu_1\psi_1(t) + \nu_2\psi_2(t)\,, \qquad (24)$$

$where$:

$$\nu_1 = \cos\varphi_0;\ \nu_2 = \sin\varphi_0\,;$$
$$\psi_1(t) = a(t)\cos[\omega_0 t + \mu(t)]$$
$$\psi_2(t) = a(t)\sin[\omega_0 t + \mu(t)]$$

Here the envelope α(t) and the phase μ(t) are slowly changing deterministic functions; the random phase φ_0 is uniformly distributed in [0,2π]
The following algorithm is synthesized

$$|\mathbf{T}(\mathbf{x})|^2 = \frac{1}{n}\left\{\sum_{i=2}^{n}\sum_{j=-1}^{0}\alpha(t_{i+j})\cos[\omega_0 t_{i+j} + \mu(t_{i+j})]\,\hat{\varphi}_j(\mathbf{x}_{i+1}^i)\right\}^2 + \frac{1}{n}\left\{\sum_{i=2}^{n}\sum_{j=-1}^{0}\alpha(t_{i+j})\sin[\omega_0 t_{i+j} + \mu(t_{i+j})]\,\hat{\varphi}_j(\mathbf{x}_{i+1}^i)\right\}^2 \qquad (25)$$

And the structure scheme is presented as well (Figure 1)

4 ILLUSTRATIVE EXAMPLES

On the Figure 1 input data go DL and two nonlinear transformations. Bases functions also pas DL and form statistics $T_1(x)$ $T_2(x)$, one follows summation and squared, again summation and comparison by TD and respectively accept H_0 or H_1

Figure 2 is depicted estimation probability of correct detection AR1 at constant signal One can see increasing the probability of correct detection for different α

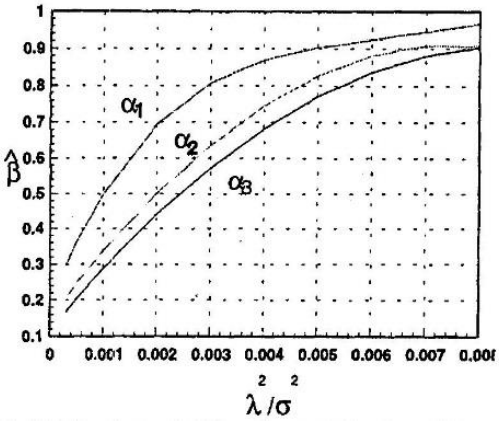

Figure 2: Estimation probability of correct detection AR1 Constant signal α_1 =0.05, α_2 =0.01 α_3 =0.005, n=100.

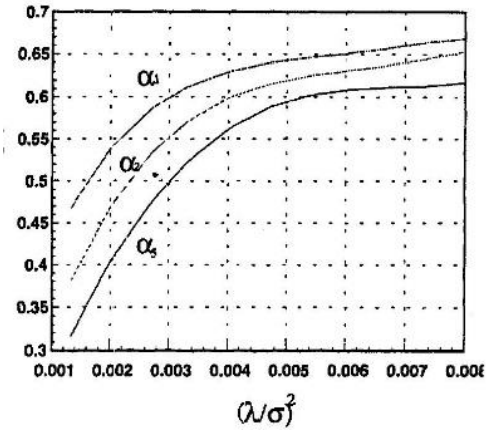

Figure 3: Estimation probability of correct detection; AR1, Pulse-signal, α_1=0.05, α_2=0.01 α_3=0.005, n=100.

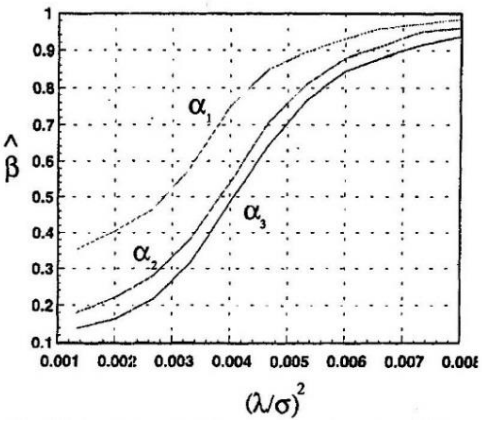

Figure 4: Estimation probability of correct detection; AR3, Const. signal, α_1=0.05, α_2=0.01 α_3=0.005, n=100.

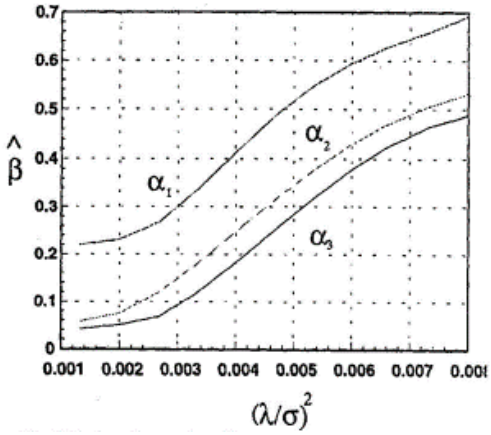

Figure 5: Estimation probability of correct detection; AR3, Pulse signal, α_1=0.05, α_2=0.01 α_3=0.005, n=100.

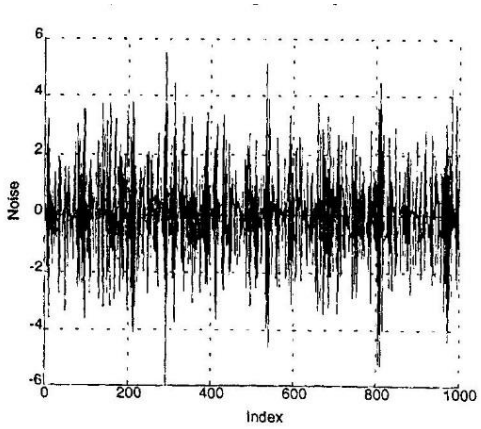

Figure 6: AR1, $N_i+0.8N_{i-1} \approx \eta_i$, $\eta_i \sim N(0,1)$

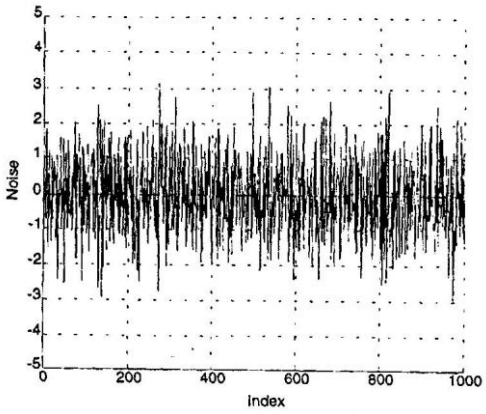

Figure 7: AR3, $N_i+0.95N_{j-1} + 0.2996N_{i-2} + 0.0314N_{i+3} = \eta_i$, $\eta_i \sim N(0,1)$

5 CONCLUSIONS

In this paper, Asymptotic Optimal algorithms have been addressed, as a way of overcoming the prior uncertainty of communication systems. They have been compared by classical methods of mathematical statistics, sign and rank algorithms, robust statistics (algorithms), and adaptive algorithms. Further, these algorithms appear to have structure that is not difficult to implement. Hence, in combination with adaptive algorithms (learning samples), they represent a powerful way of overcoming the prior uncertainty of communication systems. Practically, they are applied for finite "n" and become suboptimal. We can refer mathematical study of AO algorithms to works of *Le Cam* and *Roussas*, etc. However, analytical study of rate of convergence of AO algorithms is not resolved yet.

ACKNOWLEDGEMENTS

The author is grateful to the Research Laboratory of Kyoto University, Japan.

REFERENCES

Shinohara N., Blagovest Shishkov, Hiroshi Matsumoto, Kozo Hashimoto, and A.K.M. Baki, 2008. *"New Stochastic Algorithm for Optimization of Both Side Lobes and Grating Lobes in Large Antenna Arrays for MPT"*, IEICE Trans. Communications, Vol.E91-B:1:286-296

Shishkov, B.B. 2006 *"Asymptotic Optimal Algorithms in Statistical Communication Theory",* Proc. of National Colloquium of Mathematics,

Shishkov, B.B. 2006. "*Locally Asymptotic Normality of Parametric Models of Time Series"*, Comptes Rendus de l'Academie bulgare des Sciences, Tome 59, No 8,

Shishkov, B. 2005. "*Beamforming of Reactively Controled Adaptive Antenna Array Based onCyclostationary Signal Properties*", Comptes Rendus de l'Academie bulgare des Sciences, Tome 58, No 10, 1163-1168.

Shishkov, B., H. Matsumoto, N. Shinohara. 2005 "*Probabilistic Approach to Design of Large Antenna Arrays*", Pliska Studia Mathematica Bulgarica, Vol. 17, pp. 249 – 269.

Shishkov, B., J.Cheng and T.Ohira. 2002 "*Adaptive Control Algorithm for the ESPAR Antenna Based on Stochastic Approximation Theory"*, IEICE Transactions on Communications, Vol. E85-B. No.4 April 2002, pp. 802-811.

Shishkov, B., J. Cheng and T. Ohira. 2002 "Adaptive Beamforming of ESPAR Antenna -Unconventional Approach", IEICE Transactions on Electronics, Vol. E85-C. No.3 March 2002, pp.452-457.

Masson, A., B. Shishkov and F. Lefeuvre. 2001 "*On the Use of High Order Statistical Tests of the Analysis of Time Series Associated with Space Data*", Traitement du Signal, France, Vol. 18, No1, 2001, pp. 59-78.

Shishkov, B. and T. Ohira. 2001 "*Adaptive Control Algorithm for the ESPAR Antenna",* ATR Journal, pp.24-25, Kyoto, Japan, October 2001.

Shishkov, B., H. Tsuji, J. Xin, Y. Hase. 1998. "*Spatial and Temporal Processing of Cyclostationary Signals in Array Antennas Based on Linear Prediction Model",* Proc. of the Telecommunications Advancement Organization (TAO) of Japan, pp. 1-34.

Shishkov, B.B. 1994. "*Testing Hypotheses on Distribution's Parameters of Time Series and Applications to Signal Detection",* Radio Eng. Electron. Phys., t. XXXIX, No 3, pp.411-423.

Shishkov, B.B. 1994 "*Testing the Hypotheses of Time Series Distribution Parameters. Application to Signal Detection",* Journal of Communications Technology and, Electronics 39(7), pp. 64-76.

Shishkov, B.B. 1994. "*Asymptotic Optimal Algorithms for Detecting Signals on a Background of Correlative Interference and White Noise*", Radio Eng. Electron. Phys., t. XXXIX, No 1, pp. 76-81.

Shishkov, B.B. 1994 "*Asymptotically Optimum Algorithms for Signal Detection in Background of Correlated Interference and White Noise (Discrete Time)"*, Journal of Communications Technology and, Electronics 39(5), pp. 35-40.

Shishkov, B.B. 1993 *"Optimum Quantizer-Detectors for Deterministic Signals in m-Dependent Markov Noise",* Radio Eng. Electron. Phys., t. XXXVIII, No 11, pp. 2047-2064.

Shishkov, B.B. and S.I. Penev. 1982 "*Asymptotic Theory of Signal Identification According to Continuous Observations",* University Annual (Applied mathematics), Tome 18, Book 3, pp. 131- 140.

IMPACT OF RECENT GEOMAGNETIC STORMS ON IONOSPHERIC CHARACTERISTICS OVER EUROPE

Haris Haralambous, Photos Vryonides, and Christina Oikonomou
Frederick Research Center, 7 Filokyprou St., Palouriotisa, Nicosia 1036, Cyprus
eng.hh@fit.ac.cy

V. Dobrica, C. Demetrescu, G. Maris, and D. Ionescu
Institute of Geodynamics of the Romanian Academy, Bucharest, Romania

Keywords: Ionospheric storms, total electron content, F-layer critical frequency

Abstract: We investigate the ionospheric variability in terms of total electron content (TEC) and F-layer critical frequency (foF2) during the more significant storm events (3-9 April 2010 and 7-13 March 2012) during the rising phase of the current solar cycle for the period 2009-2012. For this purpose TEC values were derived from RINEX files of nine GNSS permanent stations located in Europe. Increase in the background vTEC values is being observed, which represent a clear positive storm effect. The foF2 variations during these two geomagnetic storms was also studied with the aid of the empirical model IRI-2012 and the model results were then compared with ionosonde measurements obtained from 9 European stations. The results indicate that the IRI with the STORM model option captures quite well the directions of the changes in most cases but does not reproduce well the measured values.

1 INTRODUCTION

The interaction between the Sun and upper atmosphere intensifies during space weather events such as CME (Coronal Mass Ejections) and solar flares which can cause geomagnetic storms that can significantly modify the spatial and temporal ionospheric structure. During a geomagnetic storm, the solar wind energy deposited into the magnetospheric polar cap region will eventually be dissipated into the ionosphere and thermosphere. Meanwhile, various physical and energy transport processes within the ionosphere become extreme and more complicated.

In particular, one of the major indications of the magnetosphere ionosphere coupling is the significant variation of electron density during a storm. Basically, the peak electron density of the F-region (NmF2) and therefore the F-layer critical frequency (foF2) which is directly related to NmF2 can either increase or decrease from their mean value during disturbed conditions (positive or negative ionospheric storms).

The study of such ionospheric perturbations produced during geomagnetic storms is also of practical interest since trans-ionospheric radio communications and also satellite ephemeris are severely degraded during these events. A number of instruments have been used to investigate the electron density variation during such events. Several investigators have shown that the observations of total electron content (TEC) by the Global Positioning System (GPS) can contribute to understanding of the characteristics of ionospheric variations during geomagnetic storms (Mannucci et al., 1993, Maruyama et al., 2004, Kumar and Singh, 2011). Other studies have also demonstrated that empirical modeling can encapsulate and replicate underlying trends in the ionospheric response during these conditions (Araujo-Pradere et al., 2002, Adewale et al., 2013). One of the most widely used empirical models is the International Reference

Ionosphere (IRI) which in its latest version of 2012 includes an empirical Storm-Time Ionospheric Correction Model (STORM) extension to account for storm-time changes of the F layer critical frequency (foF2) during increased geomagnetic activity (Bilitza et al., 2011). Measurements of the F-layer peak ionospheric characteristics deriving from different ionosonde stations are also employed in conjuction with GPS and empirical model products.

During the present solar cycle that is currently undergoing its maximum activity phase, a number of geomagnetic storm events was registered and is presented along with a demonstration of their effects on ionospheric characteristics such as TEC and foF2. In order to achieve this goal all three above mentioned techniques were applied. Within this frame the evaluation of IRI-2012 model (with and without STORM model option) was possible through the comparison of model results with ionosonde measurements from different stations.

2 EXPERIMENTAL DATA AND METHODOLOGY

2.1 GPS derived TEC

Global Positioning System (GPS) receivers provide an opportunity to determine total electron content. The TEC values observed for two geomagnetic storms of the period 2010-2012 (Table 1) is used in this paper to discuss the behaviour of ionospheric TEC during geomagnetically disturbed periods. Variation of TEC is studied in correlation with the geomagnetic index Dst which represents the various phases of a storm. For this purpose we use RINEX files from nine GNSS permanent stations located in Europe and belonging to EUREF Permanent networks (Figure 1). These files have been processed with a calibration algorithm to obtain vertical total electron content, vTEC (Ciraolo, 2012). This processing technique assumes ionospheric thin shell model (located at 350km of altitude) to obtain vTEC from slant total electron content (sTEC) at the Ionospheric Pierce Point, IPP. Minimum values of Dst can be used to classify the magnetic storms: weak (-30nT<Dst<-50nT), moderate (-50nT<Dst<-100nT) intense (-100nT<Dst<-200nT) and very intense (Dst>-200nT). The Hourly Dst indices are obtained from the World Data Center at the University of Kyoto database. As can be seen in Table 1, the storms are classified with the negative intensity of Dst (intensity of ring current) index.

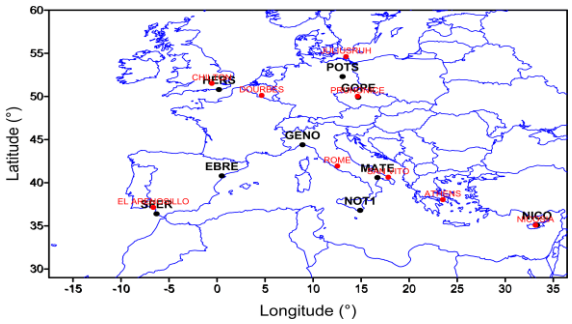

Figure 1: GNSS Stations (black dots) and ionosonde stations (red dots).

Table 1: Selected storm events for 2010-2012.

DATE	D_{ST} INDEX MINIMUM	CLASSIFICA-TION
3-9 April 2010	-81 nT	Moderate
7-13 March 2012	-131 nT	Intense

2.2 IRI-2012 modeled foF2 critical frequency

The empirical IRI model provides values of electron density and temperature, and ion composition as a function of height for a given location, time, and sunspot number. In this investigation, the latest version of IRI model (IRI-2012) (Bilitza et al., 2011) is running using two options to provide the foF2: with the STORM model turned ON and with the STORM model OFF. This model extension is driven by past history values of the geomagnetic index ap (The magnetic index applied is the integral of ap over the previous 33 hours with a weighting function deduced from physically based modelling) and it adjusts the quiet-time foF2 to account for storm-time changes in the ionosphere. The model foF2 results are also compared with the foF2 measured at nine different European ionosonde stations for the two selected storms (Table 1).

3 DISCUSSION - CONCLUSIONS

3.1 TEC variations during geomagnetic storms

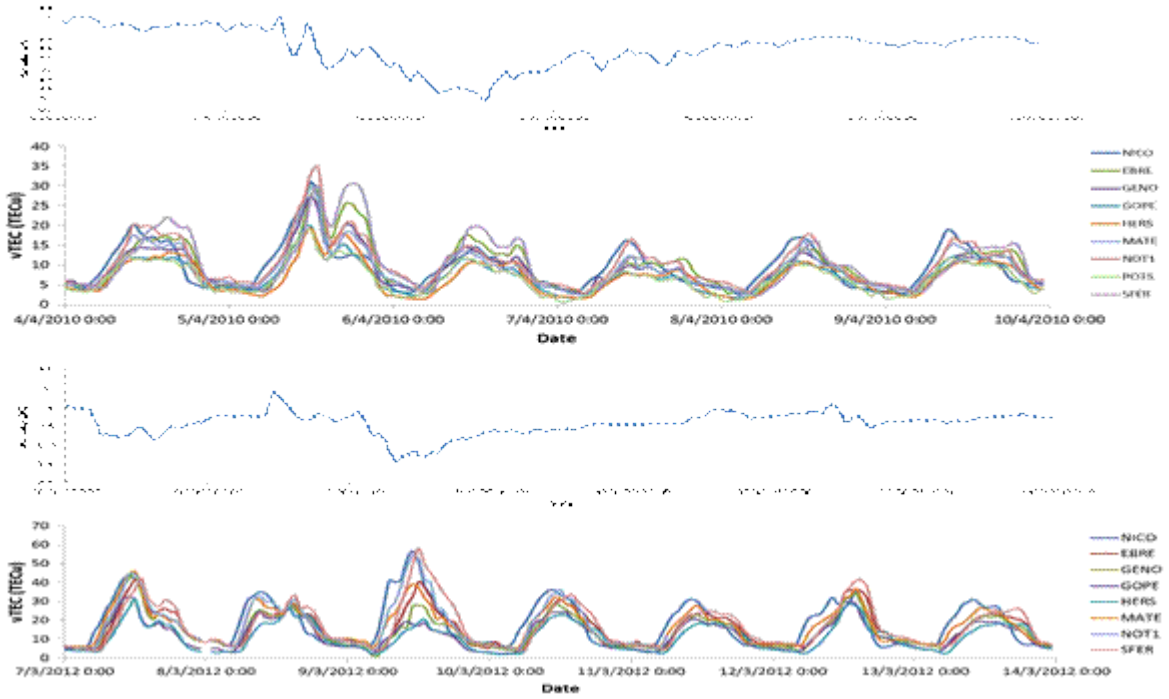

Figure 2: Temporal variation of the Dst Index and vTEC plots for the two storm periods during 2010-2012.

The first significant moderate geomagnetic storm of the current solar cycle was observed in April 2010 (Figure 2, upper two panels). It started just before noon on 5th of April with a slow decrease of the Dst index which continued to the following day and later recovered to normal condition two days after. The initial phase of the storm started around 1000LT on 5th April, 2010 and the main phase around 2400LT on the same day reaching its peak activity (Dst = -81nT) around 1500LT the following day (i.e April 6th, 2010). The recovery phase started slowly, immediately after reaching its minimum decrease, restoring back to its normal condition at around 2100LT on 7th of April, 2010.

Solar activity during the week 5 – 12 March 2012 (Figure 2 lower two panels) was dominated by three X-class flares, twelve M-class flares, and numerous C-class flares. In accordance with the ground geomagnetic field measurements the storm of 7 March 2012 started with the storm commencement (SC) at 0420 UT. An interplanetary shock was detected at 03:35 UT by ACE with the interplanetary magnetic field (IMF) magnitude reaching 18 nT, with the north-south IMF component Bz negative during extended intervals. Around 00:00 UT on 9 March, the IMF magnitude in the interplanetary CME increased again, and this time the IMF Bz component was directed predominantly southward. Around 08:18 UT the solar wind speed suddenly increased up to around 950 km/s. Together with still negative (southward) IMF Bz component, this led to strengthening the ongoing geomagnetic storm. For these typical storm events, the amplitude level of the vTEC variations tend to increase during the first 24 hours of geomagnetic storm, and then decrease below its quiet time reference level with recovery in one or two days later. Figure 2 clearly demonstrates that all the events are ionospheric storms with a positive phase followed by a negative phase and then a slow recovering phase.

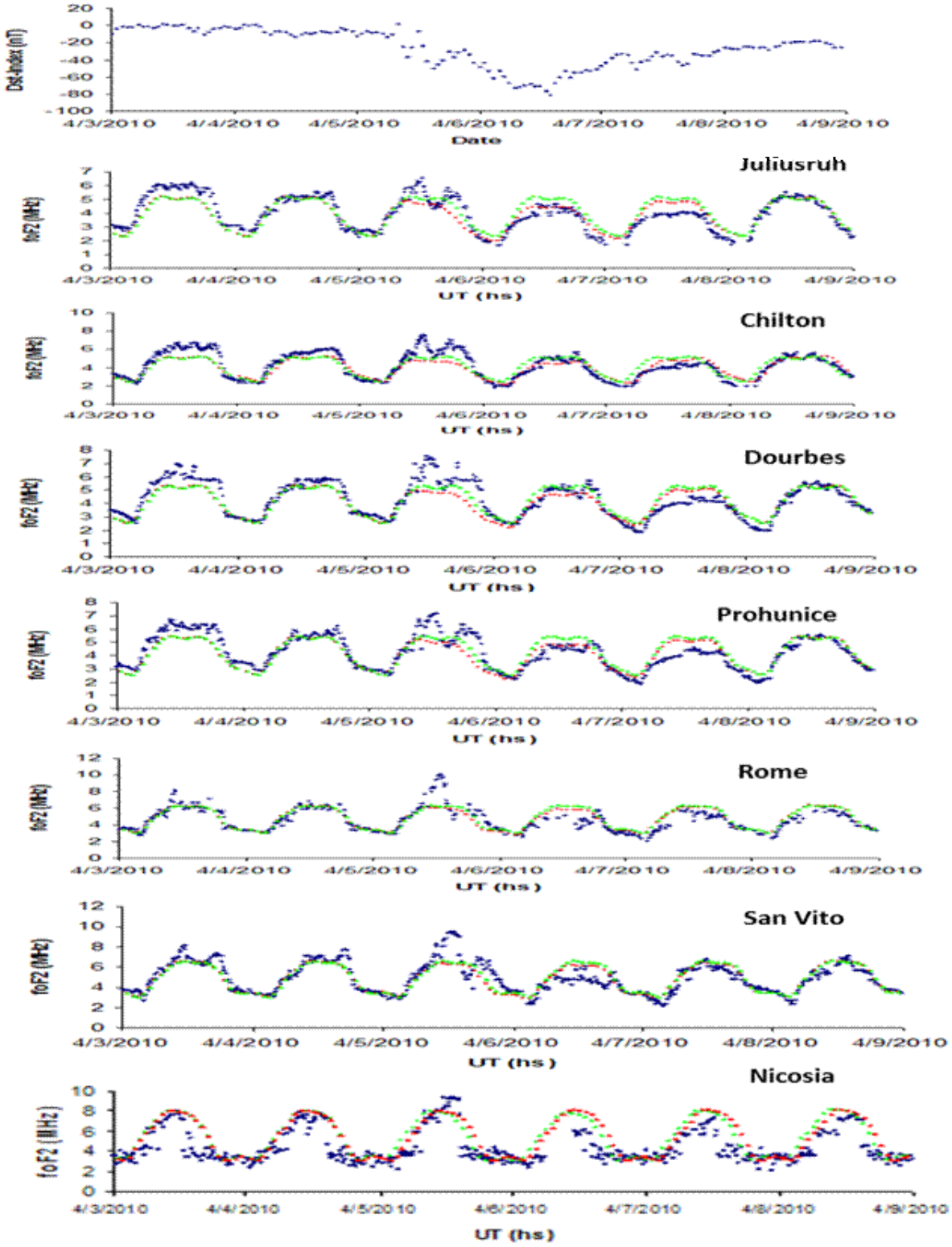

Figure 3: Temporal variation of Dst Index, storm time foF2 data, and outputs of the IRI-2012 model with (red) and without (green) STORM model for the 3-9 April 2010 storm period

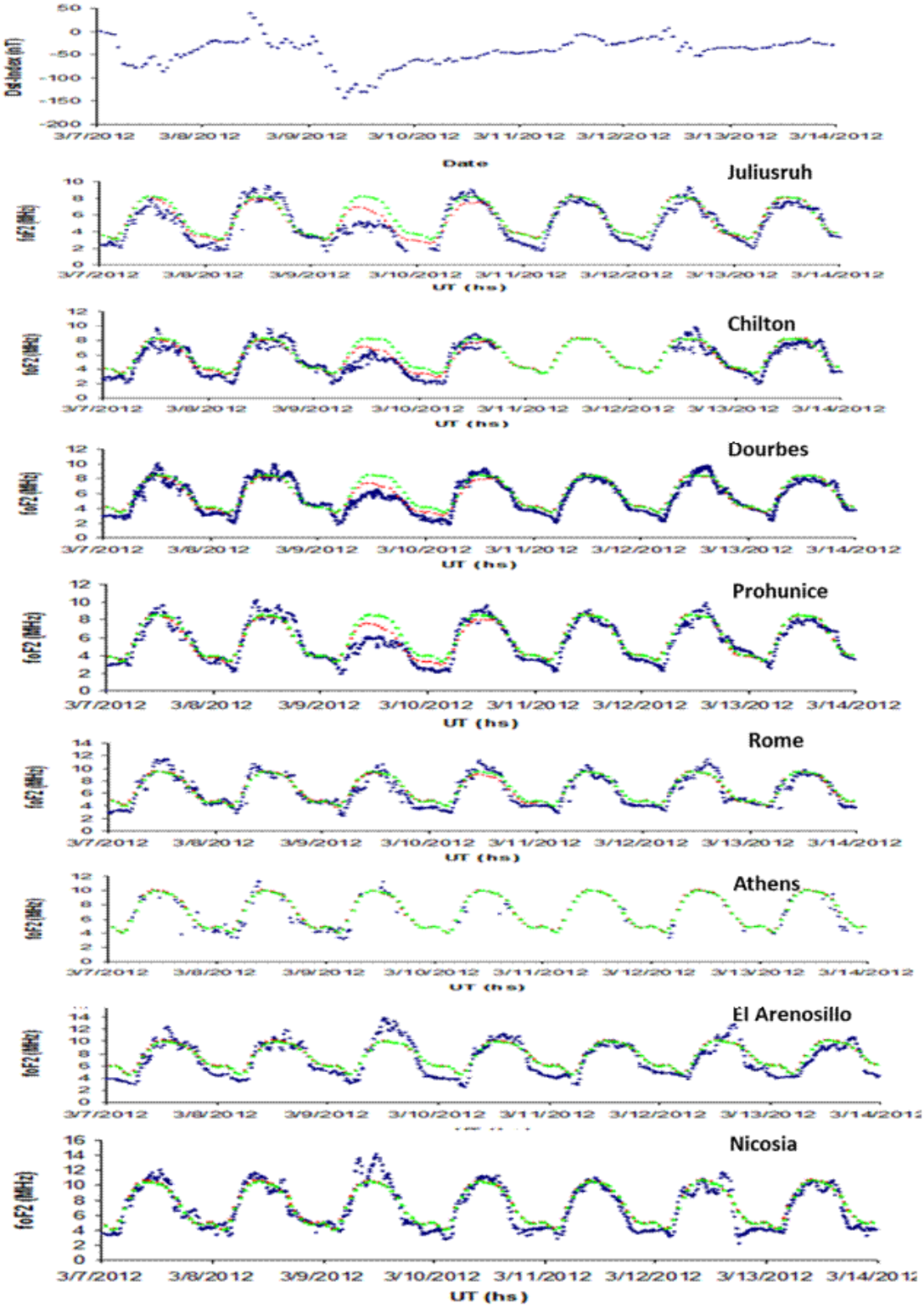

Figure 4: Temporal variation of Dst Index, storm time foF2 data, and outputs of the IRI-2012 model with (red) and without (green) STORM model for the 7-14 March 2012 storm period.

A clearly defined positive phase of the ionospheric storms occurred early in the storm development but their duration is different depending on the locations' latitude. The negative phase follows with different magnitude depending again on the latitude of the station. The first strong increase in vTEC after SC corresponds to the period (1000-1600 UT) when Dst index was decreasing rapidly to a local minimum. The maximum vTEC value is about 35 TECU (1 TECU = 10^{16} electron/m^2). The second pronounced but short lived enhancement appears in the evening sector. The negative phase for vTEC begins at these stations at about the same time on the 6th of April. Similar features are also identified during March 2012 storm. The positive deviations in TEC during ionospheric storms can lead to range errors at (L1 frequency corresponding to single-frequency receivers) 0.16m/TECU.

3.2 foF2 variations during geomagnetic storms

The top plot in Figure 3 shows the evolution of the Dst geomagnetic index for the 3- 9 April 2010 storm period. The storm was characterised by a short duration main phase followed by a relatively fast recovery. The bottom part of Figure 3 presents the behaviour of foF2 data (blue) and also both the IRI-2012 predictions with (red) and without (green) the STORM model. In addition, the absolute bias between the measured hourly foF2 values and the corresponding model predictions (with both options STORM-ON and STORM-OFF) are assessed and the maximum as well as the average absolute deviation are recorded at Table 2 and Table 3 for the two storm periods respectively.

Table 2: Absolute maximum and average hourly deviations of foF2 modelled from measured values for the 3- 9 April 2010 storm.

7-13 March 2012	STORM-ON	STORM-OFF	STORM-ON	STORM-OFF
STATION	Max. Dev	Max. Dev.	Average Dev.	Average Dev.
Nicosia	3.34	3.34	0.86	0.86
Dourbes	2.13	3.06	0.70	0.79
Athens	2.46	2.39	0.94	0.93
Chilton	2.26	3.17	0.72	0.99
Arenosillo	3.86	3.77	1.21	1.21
Juliusruh	2.71	3.77	0.84	0.97
Pruhonice	2.23	3.30	0.67	0.77
Rome	3.42	3.56	0.76	0.79

Table 3: Absolute maximum and average hourly deviations of foF2 modelled from measured values for the 7-13 March 2012 storm

3- 9 April 2010	STORM-ON	STORM-OFF	STORM-ON	STORM-OFF
STATION	Max. Dev.	Max. Dev.	Average Dev.	Average Dev.
Nicosia	4.25	4.25	0.98	1.00
Dourbes	2.48	2.12	0.51	0.50
Athens	3.25	3.09	0.70	0.65
Chilton	2.67	2.28	0.63	0.63
Arenosillo	3.89	3.54	0.87	0.85
Juliusruh	1.78	1.49	0.47	0.57
Pruhonice	2.31	1.80	0.52	0.59
Rome	4.13	3.88	0.55	0.57
San Vito	3.29	3.05	0.57	0.60

As it can be seen IRI-2012 with STORM model follows the foF2 variations better than IRI-2012 without the empirical storm effect. The STORM model captures the direction of initial changes but it overestimates the measured foF2 during the end of the main phase. Figure 4 presents the variations of Dst and foF2 between 7-13 March 2012. For the mid-latitude stations like Nicosia, Athens and El Arenosillo the STORM model tends to underestimate the foF2 data whereas for the rest stations it tends to overestimate the foF2 data.

In this study an increase in background vTEC values is being observed, which represent a clear positive storm effect consistently for both storms at all middle-latitude European stations. The comparison of foF2 measurements from 9 European stations with the outputs of the IRI-2012, with and without the STORM model, during these storms indicated that the STORM model captures quite well the directions of the changes in most cases but does not reproduce well the measured values.

ACKNOWLEDGEMENTS

This paper is funded by the project Disturbed Ionospheric and geomagnetic conditions under the influence of solar activity KY-POY/0311/05 which is financed by the Republic of Cyprus (through the ΔΕΣΜΗ 2009-2010 of the Cyprus Research Promotion Foundation).

REFERENCES

Bilitza, D., McKinnell, L.-A., Reinisch, B., Fuller-Rowell, T. 2011. *The International Reference Ionosphere (IRI) today and in the future, J. Geodesy*. 85, 909-920.

Ciraolo, L., 1993. *Evaluation of GPS L2-L1 biases and related daily TEC profiles, in: Proc. of the GPS/Ionosphere Workshop, 90–97*, Neustrelitz.

Mannucci, A.J., Wilson, B.D., Ewards, C.D., 1993. *A new method for monitoring the Earth's ionosphere total electron content using the GPS global network.* In: Proc. of ION GPS-93, Inst. of Navigation, 1323–1332.

Maruyama, T.G., Ma, G., Nakamura, M., 2004. *Signature of TEC stormon 6 November 2001 derived from dense GPS receiver network and ionosonde chain over Japan*. J. Geophys. Res. **109**, A10302.

Kumar, S, Singh A.K., 2011. *Storm time response of GPS-derived total electron content (TEC) during low solar active period at Indian low latitude station Varanasi.* Astrophys Space Sci, 331, 447–458.

Adewale, A.O., Oyeyemi, E.O., Adeloye, A.B., Adedokun M.B., 2013. *Ionospheric effects of geomagnetic storms at Hobart and comparisons with IRI model predictions*. Journal of Sci. Res. 14, 98 - 105.

Araujo-Pradere, E.A., Fuller-Rowell, T.J., 2002. STORM: *an empirical stormtime ionospheric correction model 2*. Validation. *Radio Sci*. 37 (5), 1071.

STUDY OF THE TOPSIDE ELECTRON DENSITY PROFILES OBTAINED BY COSMIC SATELLITES AND IONOSONDES OVER EUROPE DURING A FOUR YEAR PERIOD

H. Haralambous and C. Oikonomou
Frederick Research Center, 7 Filokyprou St., Palouriotisa, Nicosia 1036, Cyprus
eng.hh@fit.ac.cy

Keywords: Ionosphere, radio occultation, electron density profile, total electron content.

Abstract: The determination of ionospheric electron density profile below the electron density peak (bottomside electron density profile) has been traditionally conducted on a relatively local basis by ground-based ionosondes. Since ionosondes can only probe the ionosphere up to the maximum electron density, the determination of the profile above the peak (topside electron density profile) is represented by models which extend the profile above the peak. An alternative modern technique for measuring electron density profiles is the GPS Radio Occultation conducted by means of signals transmitted by GPS satellites and received by LEO satellites. The profiles are inferred indirectly exploiting radio signals crossing the Earth's ionosphere and undergoing refraction. The FORMOSAT-3/COSMIC (Constellation Observing System for Meteorology, Ionosphere, and Climate) satellite constellation is such a system based on 6 satellites and has been in operation since 2006 providing excellent spatial coverage with more than 2000 occultations per day. In this paper a comparison of the topside electron density profiles over the European area is investigated in terms of these two different measurement techniques, within a period of 4 years. A subsequent comparison is therefore presented based on the values retrieved by radio occultation measurements and ionosondes systematically monitoring the ionosphere over Europe.

1 INTRODUCTION

The specification of accurate electron density profiles of the ionosphere is a key requirement for total electron content (TEC) model development necessary for correcting ionospheric range errors in single frequency GNSS applications. The bottomside (below the F2 peak) component of the electron density profile has been routinely monitored by ionosondes compiling an extended dataset of key characteristics of the F2-layer peak, namely the peak height hmF2 and the peak electron density NmF2. A significant subset of these measurements (extending over the last three decades) has been provided by the Global Ionospheric Radio Observatory (GIRO) using the ground-based Digisonde network (Reinisch, 2009). The electron density profile of the topside ionosphere represents an important topic of interest in ionospheric studies since it has been shown that the main contribution to TEC is attributed to an altitude range above the F2 peak. However there is a lack of topside observational data as ground-based ionosondes can probe only up to the F2-layer peak, and observations from topside sounders are sparse (Reinisch and Huang, 2001) since only a few satellite missions, for example Alouette, ISIS-1 and ISIS-2 have been dedicated to topside electron density profile measurements.

Ionospheric radio occultation (RO) observations onboard low Earth orbiting (LEO) satellites (Heise, 2002), is a powerful technique to investigate the vertical and horizontal ionospheric structure achieving data coverage on a global scale. A constellation of six satellites, called the Formosa Satellite 3- Constellation Observing System for Meteorology, Ionosphere, and Climate (COSMIC),

was launched in 2006 to improve global weather prediction and space weather monitoring (Rocken, 2000). Three different instruments make up the science payload of the COSMIC satellites which orbit at 800 km, namely, four sets of GPS receivers, a Tri-Band (150, 400, and 1067 MHz) beacon transmitter system, and a tiny ionospheric photometer at 135.6 nm. In this investigation we deal with the GPS receiver which is used to obtain atmospheric and ionospheric measurements through phase and Doppler shifts of radio signals. The Doppler shift of the GPS L- band signals received by a low earth orbit (LEO) satellite is used to compute the amount of signal bending that occurs as the GPS satellite sets or rises through the earth's atmosphere as seen from LEO.

The ionosonde topside electron density profiles used in this study were provided by DIAS (European Digital Upper Atmosphere Server). This is a service based on a pan-European digital data collection on the state of the upper atmosphere, which offers real-time information and historical data collections provided by most operating ionospheric stations in Europe (Belehaki and Reinisch, 2008).

The primary objective of this paper is a comparison of topside electron density profiles retrieved from COSMIC (RO) measurements with topside electron density profiles over European ionosondes (contributing to the DIAS system) and with topside electron density profiles calculated by the International Reference Ionosphere model (IRI-2007) which is the most widely used empirical ionospheric model (Bilitza and Reinisch, 2008).

2 EXPERIMENTAL DATA AND METHODOLOGY

2.1 COSMIC derived topside profiles

The Each COSMIC satellite is equipped with four antennas, two of which are used for ionospheric electron density measurements (one for rising and one for setting occultations). These two antennas collect L1 and L2 GPS phase data from up to 13 GPS satellites every second. The inversion of COSMIC data into electron density profiles is based on the difference between L1 and L2 GPS phase path measurements (Liou, 2007). Under the assumption of straight-line propagation of GPS signals in the ionosphere, the difference between the L1 and L2 phase path measurements (except for a constant offset) is approximately proportional to the TEC along the line from the LEO satellite to the GPS satellite.

On the basis of the radio occultation technique, the bending angle of GPS ray received by the GPS receivers can be converted into atmospheric refractive index through the calculation of Abel transformation. According to the Abel transformation, the spherical symmetry of the atmospheric refractive index with respect to the Earth center is the most critical assumption of the retrieval algorithm in radio-occultation of atmospheric parameters. Under this assumption, no horizontal gradient of the refractive index is allowed to exist along the spherical shell of the refractive index. In addition, the presence of plasma irregularities in the GPS raypath may cause significant fluctuations of the retrieved electron density profile, giving rise to large uncertainty of the estimation and impairment of the data reliability.

2.2 Ionosonde derived topside profiles

The DIAS server operates since 2005 and is based on European ionospheric stations (those contributing to the present study are shown in Figure 1) with the capability of automatically scaling and transmitting in real time all important parameters characterising the ionosphere and delivers such products as real-time and archive ionograms, foF2 plots and electron density profiles. DIAS calculates the topside electron density profile over each ionospheric station assuming an α-Chapman function with constant scale height H_T (derived from bottomside ionograms) for the topside electron density distribution.

Figure 1: Ionospheric stations considered in this study.

2.3 IRI derived topside profiles

The International Reference Ionosphere (IRI) is an international project sponsored by the Committee on Space Research (COSPAR) and the International Union of Radio Science (URSI) based on available experimental observations from data sources including ground, in-situ as well as satellite observations. For a given location, time and date, IRI-2007 provides monthly averages of the electron density, electron temperature, ion temperature, and ion composition in the altitude range from 50 km to 2000 km. There is also the option to drive the model with measured ionospheric peak characteristics to obtain a better representation of the electron density profile. This option was exploited in the current study to estimate topside electron density profiles over European ionosondes using measured foF2 and hmF2 values obtained by the COSMIC profiles. The IRI model was applied under the Nequick topside option over the geographical scope of the mid-latitude European region at the footprint location of each occultation in the vicinity of an ionosonde.

2.3 Data selection methodology

In this comparative study 238 radio occultation profiles obtained within the period August 2006 to October 2010 were considered all of which were selected under the criterion of their F-layer peak characteristics (foF2 and hmF2) matching the values obtained from European ionosondes. Electron densities at each altitude as well as peak ionospheric characteristics and occultation footprint were extracted directly from these profiles provided by the COSMIC Data Analysis and Archive Center (CDAAC). No further processing was carried out apart from rejection of profiles which exhibited excessive electron density fluctuation. In order to make the comparison between COSMIC and ionosonde measurements as accurate as possible, collocation distance between the GPS occultation at F-layer peak and the ionosonde location was limited up to 1^o in latitude and longitude within a time interval for the occultation occurrence within 15 min. Only data in geomagnetically quiet conditions were considered in the comparison (Kp<2). It must be clarified that COSMIC retrieved electron density profiles should be considered as vertical profiles as the geographical location of the ray path tangent points from the bottom to the top of a profile may differ by several hundred kilometers. So the effective profile which is considered is the result of imaging at the same time vertical and horizontal ionospheric structures which for the sake of the Abel transformation being applied, are considered stable (non-drifting).

3 RESULTS AND DISCUSSION

The topside electron density profiles considered in this study were selected based on the fact that the COSMIC and ionosonde peak profile characteristics are practically equal. This facilitated the investigation to focus on the shape of the profile. The IRI derived electron density profiles were also calculated based on the peak profile characteristics of every COSMIC-ionosonde profile pair allowing the IRI representation of these cases to be explored.

Figures 2-5 demonstrate characteristic cases of topside electron density profile comparisons from all ionosondes considered. We immediately observe that the IRI representation significantly overestimates the COSMIC electron density in the majority of the cases shown. There are some cases (Figure 3b, 3d, 3e, 4d, 5c, 5d, 5f) where this overestimation effect is diminished, over 500 km. There are even some cases (Figure 3f, 4b, 4c, 4d) where the COSMIC electron density profile is underestimated by IRI. However the general trend is for IRI to overestimate COSMIC topside electron density profiles.

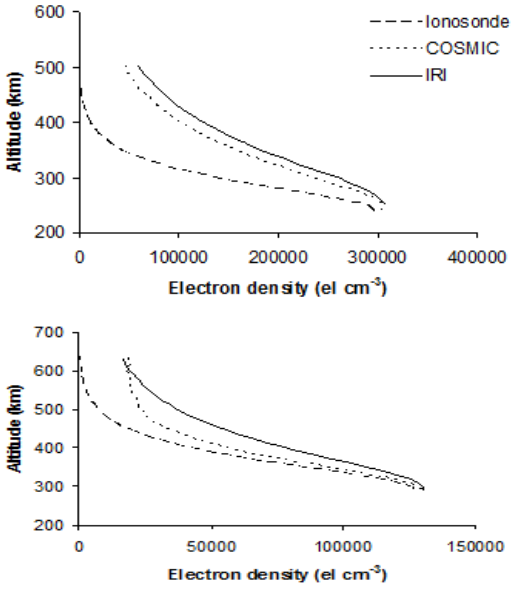

Figure 2. COSMIC, Ionosonde and IRI topside electron density profiles over Athens. a) at 4/10/2006 17:08 UT (upper panel) and b) at 24/2/2007 22:52 UT (lower panel).

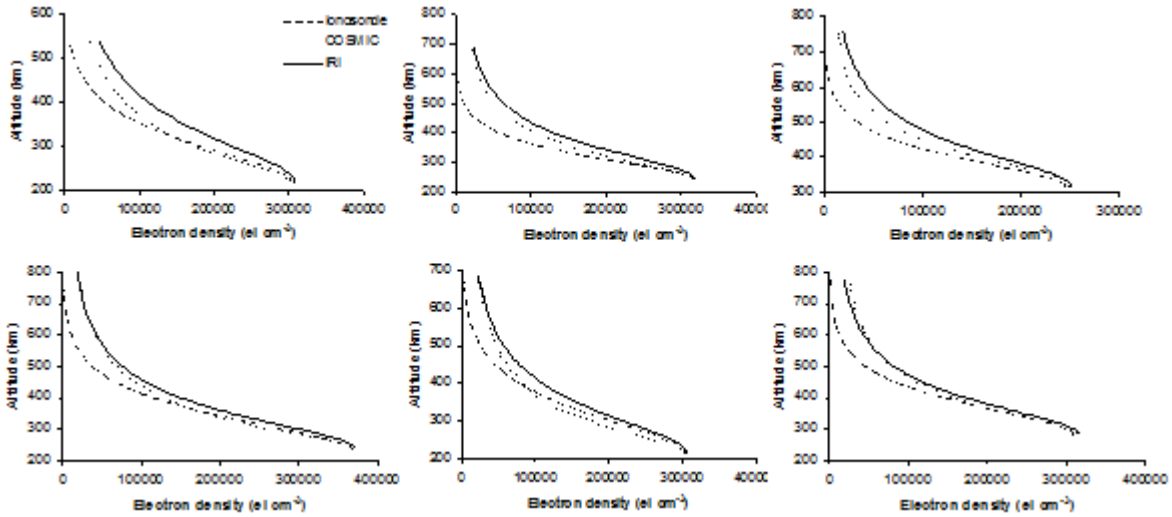

Figure 3. COSMIC, Ionosonde and IRI topside electron density profiles over Pruhonice a) at 15/8/2006 14:09 UT (upper left panel), b) at 4/5/2009 17:12 UT (upper middle panel), c) at 11/4/2010 21:51 UT (upper right panel), d) at 16/4/2010 09:12 UT (lower right panel), e) at 20/6/2010 06:42 UT (lower middle panel) and f) at 28/8/2010 17:37 UT (lower right panel).

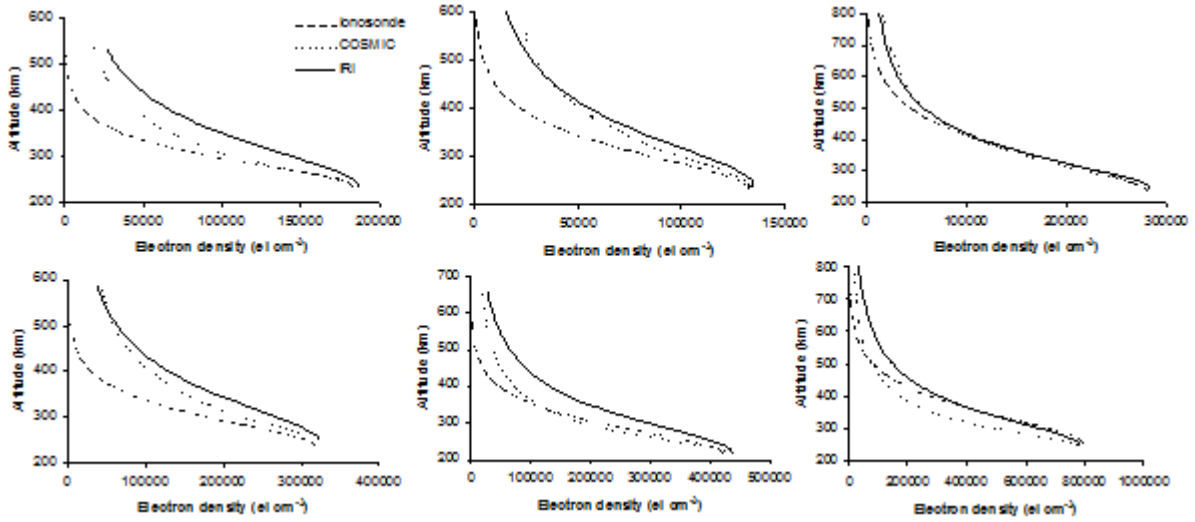

Figure 4. COSMIC, Ionosonde and IRI topside electron density profiles over Juliusruh and Ebre. a) Juliusruh 25/10/2008 16:37 UT (upper left panel), b) Juliusruh 30/6/2009 03:11 UT (upper middle panel), c) Juliusruh 7/5/2009 09:24 UT (upper right panel), d) Juliusruh 21/9/2009 16:10 UT (lower right panel) e) Ebre 10/11/2007 13:56 UT (lower middle panel) and f) Ebre 25/10/2010 14:38 UT (lower right panel)

.

Considering ionosonde profiles we can immediately observe that IRI representation significantly overestimates the ionosonde derived electron density at every altitude. We must however note that as mentioned before the ionosonde topside electron density profile is not based on actual measurements but on an α-Chapman function with constant scale height H_T for the topside electron density distribution based on the measured F2-layer peak characteristics (foF2-hmF2) that are derived from measured bottomside profiles (Reinisch and Huang, 2001). Such fit can be reasonable for the first few hundred kilometers above hmF2, and the use of a Chapman-type function to larger heights, like 800 km or more, would require using a scale height that continuously varies with height (. It is therefore worth noting that recent efforts have resulted in improved topside electron density profile representation from ionosonde measurements

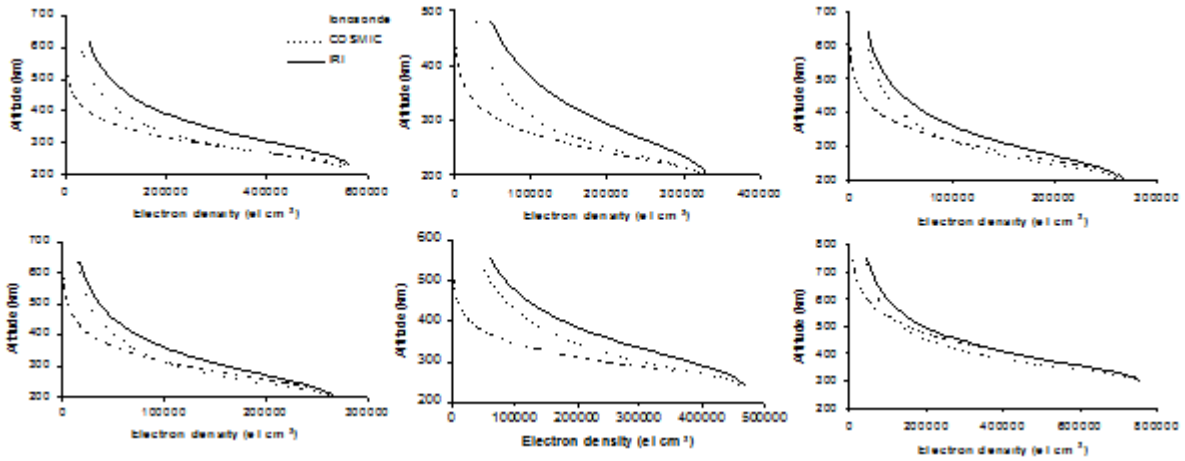

Figure 5. COSMIC, Ionosonde and IRI topside electron density profiles over Rome and Arenosillo. a) Rome 15/8/2006 14:09 UT (upper left panel), b) Rome 14/12/2007 12:49 UT (upper middle panel), c) Rome 22/3/2008 07:10 UT (upper right panel), d) Rome 19/4/2008 16:06 UT (lower right panel) e) Arenosillo 15/8/2006 14:09 UT (lower middle panel) f) Arenosillo 4/5/2009 17:12 UT (lower right panel)

(Nsumei, 2012). There are a few cases (Figure 3d, 3f, 4c, 4f, 5f) where this overestimation is minimised, especially near the F2-layer peak. The fact that in these examples the COSMIC profiles also coincide to a great extend with ionosonde and IRI representations underlines the satisfactory IRI performance in these particular cases. In almost all of the cases the ionosonde topside electron density profile underestimates the COSMIC profile. Since the COSMIC profile is composed by true measurements we can conclude that the ionosonde bottomside-based topside electron density profile model is not adequate in representing topside electron densities. We also determined a certain maximum of this underestimation to occur around 400 km (as shown in Figure 6 based on Juliusruh and Pruhonice overlapping profile differences.

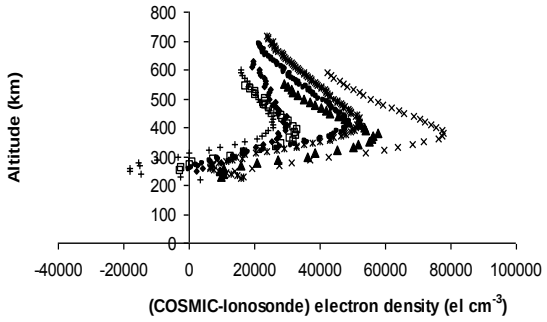

Figure 6. COSMIC-Ionosonde topside electron density profile differences over Juliusruh and Pruhonice.

4 CONCLUSIONS

In this study we have attempted to compare topside electron density profiles from COSMIC occultation mission, ionosondes operating in the European region and modeled IRI profiles based on bottomside measured peak ionospheric characteristics (foF2-hmF2) with the NeQuick topside model option. By comparing profiles corresponding to equal values of foF2-hmF2 we focused on the shape of the topside profiles. The main conclusions that come out of this investigation is the systematic IRI overestimation of both the COSMIC measured and ionosonde modeled topside profiles. There is also a systematic trend of the ionosondes to underestimate the COSMIC profiles which indicates that an improved topside representation is necessary and which in fact has been addressed recently (Nsumei, 2012). There is also an indication of possible maximization of the discrepancy between COSMIC and ionosonde profiles around 400 km. This will be further explored with additional measurements and to a much greater extend in the near future with the new COSMIC mission and the next generation of Global Navigation Satellite System (GNSS) that is expected to provide continuity of RO to the scientific community.

REFERENCES

Reinisch, B.W., Galkin, I.A., Khmyrov, G.M., Kozlov, A.V., Bibl, K., Lisysyan, I.A., Cheney, G.P., Huang, X., Kitrosser, D.F., Paznukhov, V.V., Luo, Y., Jones, W., Stelmash, S., Hamel, R., Grochmal, J. 2009. *The new digisonde for research and monitoring applications.* Radio Sci. 44, RS0A24.

Reinisch, B. W., and X. Huang. 2001. *Deducing topside profiles and total electron content from bottomside ionograms.* Adv. Space Res., 27, 23–30.

Heise, S., Jakowski, N., Wehrenpfennig, A., Reigber, Ch., Lu¨ hr, H. 2002. *Sounding of the topside ionosphere/plasmasphere based on GPS measurements from CHAMP: initial results*. Geophys. Res. Lett. 29 (14).

Rocken, C., Y.-H. Kuo, W. Schreiner, D. Hunt, S. Sokolovsky, and C. McCormick. 2000. *COSMIC system description.* Terr. Atmos. Ocean Sci., 11, 21-52.

Belehaki A., L. Cander, B. Zolesi, J. Bremer, C. Juren, I. Stanislawska, D. Dialetis, M. Hatzopoulos. 2005. *DIAS project: The establishment of a European digital upper atmosphere server*. Journal of Atmospheric and Solar-Terrestrial Physics, 67 (12): 1092-1099.

Bilitza, D., Reinisch, B. W. 2008. *International Reference ionosphere 2007: "Improvements and new parameters"*. Adv. Space Res. 42, 599-609.

Liou, Y.-A., A. G. Pavelyev, S.-F. Liu, A. A. Pavelyev, N. Yen, C.-Y. Huang, and C.-J. Fong. 2007. *FORMOSAT-3/COSMIC GPS Radio Occultation Mission: Preliminary Results*. IEEE Transactions on Geoscience and Remote Sensing, 45(11).

Reinisch, B.W., Nsumei, P., Huang, X., Bilitza, D.K. 2007. *Modeling the F2 topside and plasmasphere for IRI using IMAGE/RPI and ISIS data*. Adv. Space Res. 39, 731–738.

Nsumei, P., B. W. Reinisch, X. Huang, and D. Bilitza. 2012. *New Vary-Chap profile of the topside ionosphere electron density distribution for use with the IRI model and the GIRO real time data*. Radio Sci., 47, RS0L16.

MACHINE LEARNING TECHNIQUES IN SOFTWARE SYSTEM FOR SIMULATION OF CONVOLUTIONAL ENCODERS AND DECODERS

Adriana Borodzhieva
Faculty of Electrical Engineering, Electronics and Automation, Telecommunications Department, University of Ruse, 8 Studentska Street, Ruse, Bulgaria
aborodjieva@ecs.uni-ruse.bg

Galia Marinova
Telecommunications Faculty, Technical University of Sofia, 8 Kl. Ohridski Blvd., Sofia, Bulgaria
gim@tu-sofia.bg

Tzvetomir Vassilev, Plamen Manoilov, and Stanislav Kostadinov
Faculty of Natural Sciences and Education, Department of Informatics and Information Technologies, University of Ruse, 8 Studentska Street, Ruse, Bulgaria
tvassilev@uni-ruse.bg, pmanoilov@ecs.uni-ruse.bg, sdkostadinov@uni-ruse.bg

Keywords: Convolutional encoders and decoders, Software system, Machine learning.

Abstract: Machine learning, as a branch of artificial intelligence for construction and study of systems that can learn from data, is applied in the Software system for simulation of convolutional encoders and decoders. The paper describes the elements of machine learning implemented: 1) Memorization; 2) Macro-operators; 3) Parameters specification used in evaluating functions; 4) Advises to be organized in Expert system. First the Software system for simulation study of channel encoders and decoders is described in brief. It allows simulation in presence of noise and integrates four modes: 1) Dividing the combinations of generator polynomials into valid and non-valid, and searching the valid combinations to find candidates for the best encoders; 2) Convolutional encoding and decoding with two options for decoding all valid combinations of generators – using hard or soft decision decoding based on Viterbi algorithm to discover the best encoders at given conditions; 3) Determining the performance of non-recursive convolutional encoders with constraint length $L = 3$; 4) Study of cascaded convolutional encoders. The machine learning techniques are considered at different stages of simulation process. The system is used by students in the specialty "Telecommunication Systems" for Bachelor degree at University of Ruse in the course "Coding in Telecommunication Systems".

1 INTRODUCTION

The paper describes the design and implementation of a software system for simulation study of convolutional encoders and decoders in presence of noise. Here, the system is considered in the context of machine learning.

Machine learning (ML) is a subfield of computer science and artificial intelligence that deals with the design and study of systems that can learn from data, rather than follow only explicitly programmed instructions. ML has strong ties to statistics and optimization, which deliver both methods and theory to the field. ML is employed in a range of computing tasks where designing and programming explicit rule-based algorithms is infeasible for a variety of reasons. Example applications include spam filtering, optical character recognition, search engines and computer vision. ML is sometimes conflated with, and sometimes distinguished from data mining and pattern recognition.

Several types of ML are considered in the paper:

Self-learning by memorization – it represents the most primitive type of ML, similar to learning by

heart in human studies, or to design reuse, or also to LUT (lookup-table) memorization in FPGA (field-programmable gate array). Here, the performance of the system (conditions of heavy, labour-intensive tasks and the resulting decisions) are retained in order to use them for granted if the request comes in to solve an already known problem. In literal form, the method does not involve any processing of these results. It turns out that in a number of tasks such preservation leads to significantly improving the system performance (speed-up, saving memory, etc.).

Self-learning by macro-operators – it is similar to self-learning by memorization – a variant of this type of ML where further processing of stored performance of the system is implied. It is used most often in systems related to action planning. For example, the system STRIPS (**St**anford **R**esearch **I**nstitute **P**roblem **S**olver), an automated planner developed by Fikes and Nilsson in 1971 at SRI International (Fikes, 1971), has a training subsystem for gathering the results from its work as macro-operators. Each macro-operator represents a general plan for solving a given type of tasks and consists of preconditions (summarize essential part of the initial state in solving the specific task of planning), body (a summary of the plan constructed by the system) and post-conditions (summary of purpose in addressing specific planning task).

Self-learning by specifying the parameters – many artificial intelligence systems use evaluating functions that are combinations of values of appropriately chosen set of parameters (features, factors), as each parameter in the estimating function is involved with the corresponding coefficient (weight). In the design and initial programming of such systems it is usually difficult a priori to determine the correct weights of all factors involved in the formulation of the evaluating function. One possible approach to determine the proper weights of individual factors is associated with including tools for modifying these weights based on the experience of the system with the current version of the estimating function. For example, the program of Samuel (Samuel, 2000) to play checkers is a combination of ML by memorization and ML by specifying the parameters. This is one of the most common methods used for ML in the art of pattern recognition and neural networks.

Self-learning by advices – here knowledge is acquired by the teacher (possibly textbook, etc.) and the training subsystem transforms this knowledge in a form that is usable by the processing subsystem. In other words, the teacher chooses contents, structure and presentation of knowledge (tips) that he/she wants to add to existing knowledge of the system and training subsystem has the task of syntactic transformation of knowledge obtained from the teacher in a way that is accessible for the processor module.

For example, the program TEIRESIAS acts as an interface for obtaining advices to the popular expert system MYCIN, an early expert system that used artificial intelligence to identify bacteria causing severe infections, such as bacteraemia and meningitis, and to recommend antibiotics, with the dosage adjusted for patient's body weight (Buchanan, B.G. and Shortliffe, E.H., 1984). TEIRESIAS performed specializations and generalizations based on advices given by the teacher, basing its work on two simple ideas: it relies on a menu-guided dialogue, which makes its internal structure of a clear maximum for the teacher; when natural language input is needed the program consults the teacher to make sure that the input text is translated correctly.

Self-learning by examples – this is a type of ML (a special case of inductive self-learning), which is usually used in systems designed to solve problems associated with the classification of objects.

2 ARCHITECTURE OF THE SOFTWARE SYSTEM

The software system (Figure 1) is implemented using the software package MATLAB 7 under Windows. The system allows solving the problems provided for self-dependent work of students during the practical exercises, making the learning process more attractive and more effective for the students and the teacher.

When starting the application a menu appears, through which the user selects the academic year required for collecting and subsequent processing of statistical data on training. Then a choice of the administrative group, to which the student belongs, is made. The course “Coding in Telecommunication Systems” is elective and studied by students in specialization *B*. When choosing a subgroup of specialization *A* an error message appears. After selecting a subgroup of specialization *B* through menu a list of students in the subgroup is displayed. The menu contains buttons with the data of each student (faculty number and full name), of which the student must select and click on “his/her button”. Thus the student is registered in the system. The

system records in a file the academic year, the subgroup, the faculty number and the full name of the student and the student's work within the system during the practical exercise. Using the generated file the lecturer can track the actions of the student after completing the exercise. The file is in a text format (*.txt*); it can be saved on flash memory and be sent by e-mail to the lecturer.

After the student's registration the choice of the topic of the current practical exercise is made through a menu.

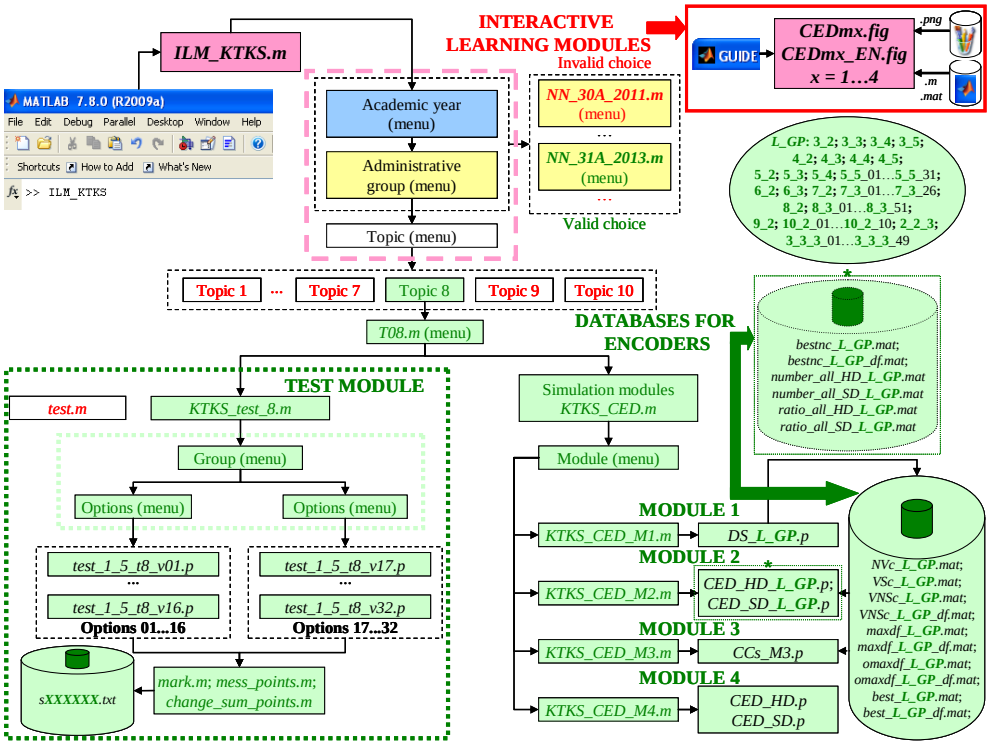

Figure 1. Architecture of the software system for simulation study of the channel encoders and decoders

The simulation modules allow simulation study of convolutional encoders and decoders in presence of noise. They were developed in MATLAB and its extensions Communications Toolbox and Symbolic Math Toolboxes. The developed software system is composed of the following simulation modules: Module 1: "Divide and search", Module 2: "Convolutional encoding and decoding", Module 3: "Determining the performance of the convolutional encoders" and Module 4: "Simulation study on cascaded convolutional encoders".

Module 1 performs the procedure "divide and search" including the processes "dividing" the combinations of generator polynomials into valid and non-valid, and "searching" the valid combinations in order to identify the candidates for the best encoders.

Module 2 performed the procedure "convolutional encoding and decoding", offering two options for decoding all valid studied (stopped and non-stopped) combinations of generators of the encoders – with hard or soft decisions decoding based on Viterbi algorithm.

Module 3 performs the procedure "determining the performance of convolutional encoders" for non-recursive convolutional encoders with constraint length $L = 3$.

Module 4 allows the study of cascaded convolutional encoders obtained on the basis of the developed mathematical models. In connection with these models the procedure "divide and search" (Module 1) had to be implemented for convolutional encoders with two registers and three generator polynomials used as an internal encoder in the structure of the cascades in the mathematical models.

In the publication convolutional encoders and decoders are considered in terms of algebraic

information theory. With regard to the statistical information theory only the decoding on the basis of the algorithm of Viterbi can be assigned, but for this purpose a built-in Matlab function was used. The paper deals communication channels with additive white Gaussian noise only.

In the first version of the system Module 1 allowed finding the encoders with a maximum value of the free distance $d_{free\,\max}$. Analysis on the simulation study of convolutional encoders by Module 2 showed that it was possible under the conditions of the experiment that another encoder different from that stated in the tables with the best encoders in the references (Blahut, 1983) was the best, i.e. it produces the least *BER* (Bit Error Rate). The analysis showed that candidates for the best encoders can be encoders with a maximum value of the free distance $d_{free\,\max}$, and if this parameter is an even number, then the candidates for the best encoders can also be encoders with the maximum free distance reduced by one $d_{free\,\max} - 1$. Thus the software system was improved, as the encoders with free distance $d_{free\,\max} - 1$ (if even number) are stored in separate databases. The analysis by Module 2 led to the conclusion that the time for simulation study of the encoders can be reduced if eliminating all catastrophic encoders from the database of candidates for the best encoders. Thus the latest improved version of the software system for simulation study of the convolutional encoders was developed.

After selecting to work with the system's simulation modules a menu for choosing the simulation module with four options for each of the simulation modules appears.

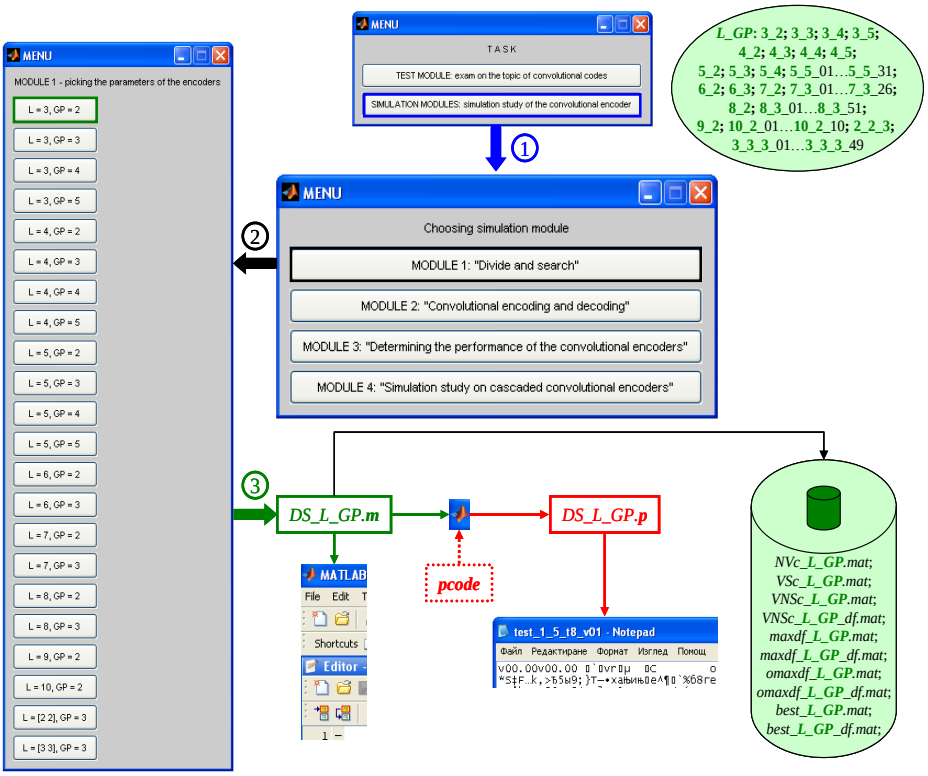

Figure 2. Choosing through a series of menus to work with simulation modules, Module 1

When selecting Module 1 (Figure 2) a menu for picking the parameters of the encoders for which the procedure "divide and search" will be done, reappears. The procedure "divide and search" is implemented for the following cases: $L = 3$ and $GP = 2 \div 5$, $L = 4$ and $GP = 2 \div 5$, $L = 5$ and $GP = 2 \div 5$, $L = 6$ and $GP = 2 \div 3$, $L = 7$ and $GP = 2 \div 3$, $L = 8$ and $GP = 2 \div 3$, $L = 9$ and $GP = 2$, $L = 10$ and $GP = 2$, $L = [2 \;\; 2]$ and $GP = 3$, $L = [3 \;\; 3]$ and $GP = 3$. All these options are available from the menu after Module 1 is selected (Figure 2).

After the parameters of the encoders are determined one of the *p*-files *DS_L_GP.p* is called. *L* and *GP* in the file names are specific numerical values, where *L* is the constraint length and *GP* is the number of generator polynomials of the encoder. For example, when pressing the button "*L* = 3, *GP* = 2" (Figure 2) the *p*-file *DS*_3_2.*p* is called. After running *DS_L_GP.p*, all possible combinations of polynomial generators are passed and a set of *mat*-files is generated: *NVc_L_GP.mat*, *VSc_L_GP.mat*, *VNSc_L_GP.mat*, *NVc_L_GP.mat*, *VSc_L_GP.mat*, *VNSc_L_GP.mat*, *VNSc_L_GP_df.mat*, *maxdf_L_GP.mat*, *maxdf_L_GP_df.mat*, *omaxdf_L_GP.mat*, *omaxdf_L_GP_df.mat*, *best_L_GP.mat*, *best_L_GP_df.mat*.

After passing through all possible combinations of generator polynomials, they are divided into two groups: 1) non-valid combinations stored in the database *NVc_L_GP.mat* and hereinafter not to be tested – these are combinations for which the output code symbols of the encoder are not determined by the current input bit of the message and/or the right-most flip-flop of the register generating the convolutional code, which violates the condition for defining the parameters of the constraint length of the code; 2) valid combinations which, in turn, also are divided into two subgroups: valid stopped combinations – stored in the database *VSc_L_GP.mat*, for which the simulation is interrupted (stopped) after expiry of a fixed time (100 seconds) in an attempt to determine their free distance, and valid non-stopped combinations – stored in the database *VNSc_L_GP.mat*, for which simulation in "divide and search" was completed successfully, as their free distance is determined. In a separate database *VNSc_L_GP_df.mat* information about the corresponding value of the free distance for all valid non-stopped combinations is stored. From all valid non-stopped combinations the combinations with the maximum value of the free distance $d_{free\max}$ are stored in a separate database *maxdf_L_GP.mat*. If $d_{free\max}$ is an even number then the database *omaxdf_L_GP.mat*, in which the encoders with free distance $d_{free\max}-1$ are stored, is generated. These two databases form the database *best_L_GP.mat* storing all the possible candidates for the best encoders. The databases *maxdf_L_GP.mat*, *omaxdf_L_GP.mat* and *best_L_GP.mat* are modified accordingly in the following databases *maxdf_L_GP_df.mat*, *omaxdf_L_GP_df.mat* and *best_L_GP_df.mat*, which contain information about the respective value of the free distance for valid non-stopped combinations with the maximal free distance $d_{free\max}$, for encoders with free distance $d_{free\max}-1$ if $d_{free\max}$ is even, and for all possible candidates for the best encoders.

When selecting Module 2 (Figure 3) a menu for choosing the type of the investigation with four options appears: 1) "Study of a convolutional encoder, hard decoding"; 2) "Study of a convolutional encoder, soft decoding"; 3) "Study of a group of convolutional encoders, hard decoding"; 4) "Study of a group of convolutional encoders, soft decoding." After selecting one of the first two options one of the files *CED_HD_M2.p* or *CED_SD_M2.p* is called. After selecting one of the last two options a menu for choosing the parameters of the study group of encoders for which the procedure "convolutional encoding and decoding" will be done, appears, i.e. the constraint length *L* and the number of generator polynomials *GP*.

When using the second system module implementing the procedure "convolutional encoding and decoding based on Viterbi algorithm" (hard or soft decisions decoding) all encoders from the databases *best_L_GP.mat* are explored for the following cases $L=3$ and $GP=2\div5$, $L=4$ and $GP=2\div5$, $L=5$ and $GP=2\div5$, $L=6$ and $GP=2\div3$, $L=7$ and $GP=2\div3$, $L=8$ and $GP=2$, $L=9$ and $GP=2$, as at the specific conditions of the simulation experiment actually the best encoder, which permits the least number of wrong bits, is found. For encoders with constraint length $L=3$ and number of generator polynomials $GP=2$ and $GP=3$ all valid combinations of generators are examined. All these options are available from the menu, which appears after selecting Module 2 (Figure 3).

After setting the encoders' parameters one of the files *CED_HD_L_GP.p* or *CED_SD_L_GP.p* is called. *L* and *GP* in the file names are specific numerical values, where *L* is the constraint length and *GP* is the number of generator polynomials of the encoder. For example, when pressing the button "*L* = 7, *GP* = 3, best" (Figure 3) the corresponding *p*-file *CED_HD*_7_3.*p* or *CED_SD*_7_3.*p* is called.

The generated databases (*mat*-files) *NVc_L_GP.mat*, *VSc_L_GP.mat*, *VNSc_L_GP.mat*, *NVc_L_GP.mat*, *VSc_L_GP.mat*, *VNSc_L_GP.mat*, *VNSc_L_GP_df.mat*, *maxdf_L_GP.mat*, *maxdf_L_GP_df.mat*, *omaxdf_L_GP.mat*, *omaxdf_L_GP_df.mat*, *best_L_GP.mat*, *best_L_GP_df.mat*, generated by the scripts *DS_L_GP.m* (Module 1) are used by the scripts

CED_HD_L_GP.m and *CED_SD_L_GP.m* (Figure 3). After running the last two scripts multiple databases (*mat*-files) are formed:
number_all_HD_L_GP.mat,
ratio_all_HD_L_GP.mat,
number_all_SD_L_GP.mat,
ratio_all_SD_L_GP.mat, *bestnc_L_GP.mat*, *bestnc_L_GP_df.mat*.

When selecting Module 3 a menu for choosing the parameters of the encoders, for which the procedure "determining the working characteristics" will be done, appears. The study covers only encoders with constraint length $L = 3$ and number of generator polynomials $GP = 2$. The possible structures of the studied encoders are 32; all of these options are available from the menu after selecting Module 3. Here, the separation of the list of the encoder generators into two groups (the first group of generators $\boldsymbol{G} = [1 \ldots 4, x]$, and the second one – $\boldsymbol{G} = [5 \ldots 7, x]$) is performed, which is required due to the need for better visualization of the list of the generators.

After setting the encoder parameters the file *CCs_M3.p* is called.

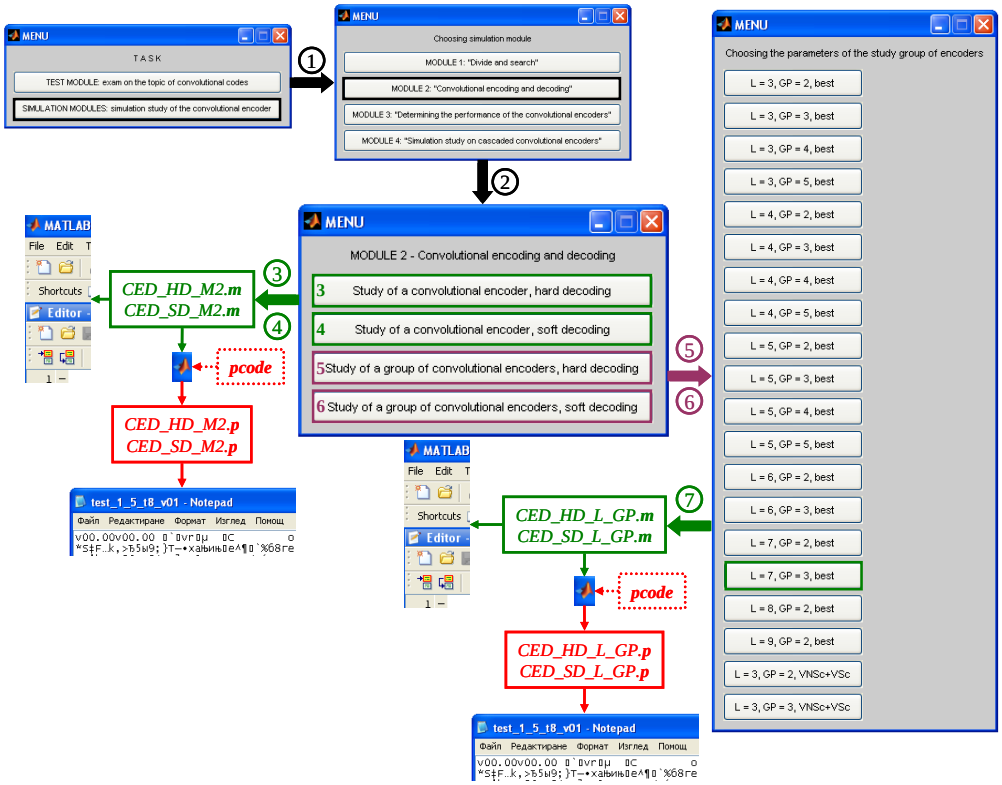

Figure 3. Choosing through a series of menus to work with simulation modules, Module 2

After selecting Module 4 implementing the procedure "simulation study of cascaded convolutional encoders" a series of menus is displayed. The user can choose: 1) a method for modifying the internal generator matrix of the cascade of two convolutional encoders (Method I and Method II); 2) a model of the cascaded encoder (Models 1, 3, 5, 7, 9, 11, 13, 15, 17 in case of Method I, and Models 2, 4, 6, 8, 10, 12, 14, 16, 18 in case of Method II), as particularities of each model with regard to the matrix for modifying the inner generator matrix and the modified generator matrix is displayed in separate graphics windows; 3) the value in the range from 1 to 10 of the parameter *j*, which is involved in the modified generator matrix, and 4) type of study with two possible options: "Study of cascaded convolutional encoder, hard decoding" and "Study of cascaded convolutional encoder, soft decoding." After selecting one of the two options one of the *p*-files *CED_HD_M4.p* or *CED_SD_M4.p* is called. The fourth system module implementing the procedure "simulation study of

cascaded convolutional encoders" allows exploring 180 cascaded encoders as for each of the models, the parameters (constraint length and generators in octal) of the external, internal and cascaded encoder are embedded in the script, and they are not expected to be entered by the user. This decreases the possibility of user mistakes.

In the upper right corner of Figure 1 four interactive learning modules with graphical user interface (*CEDmx.fig*, $x = 1 \ldots 4$) developed with MATLAB and GUIDE (Graphical User Interfaces Development Environment) for the simulation study of convolutional encoders and decoders in the presence of noise are marked. Figure 1 depicts many illustrations (*.png* files) necessary for the operation of the trainer and test modules, and the databases in the form of *mat*-files generated from Module 1 and Module 2 of the software system.

The test module of the system is designed to assess the knowledge and skills of the student, allowing the teacher to form the final mark per exercise or per semester for each student, the assessments are published online in the e-learning course "Coding in Telecommunication Systems" of the University of Ruse.

The test module to test the knowledge on the topic of convolutional codes (Topic 8) contains 32 scripts with names *test_1_5_t8_vXX.m* ($XX = 01 \ldots 32$) for each of the 32 structural models of the convolutional encoders with $L = 3$ and $n = 2$.

After selecting the test module of the system a menu for choosing a group of options (Options: 01 ... 16 or Options: 17 ... 32) and a menu for choosing an option of the Answer Sheet (Option 01 ... Option 16 or Option 17 … Option 32) are displayed. Dividing them into two groups is due to the need for better visualization of the list of options in the Answer Sheet.

After selecting the option of the Answer Sheet the corresponding *p*-file *test_1_5_t8_vXX.p* ($XX = 01 \ldots 32$) is called. A *p*-file (with the extension *.p*) can be generated by *pcode* MATLAB command. The system utilises *p*-files because of the following features: 1. *p*-files are executed faster than the corresponding *m*-files; 2. using *p*-code allows hiding the source code of the programs. It is one of the advantages of the *p*-files as the code for generating the test questions remains hidden from students. This requires either programming independently in MATLAB, or manually resolving the problem by the student using calculator.

3 MACHINE LEARNING TECHNIQUES AND THEIR IMPACT ON CONVOLUTIONAL ENCODERS SIMULATION AND STUDY

In the context of machine learning, the implemented software system may be considered as a self-learning system by memorization. As a result of the operations of Module 1 and Module 2 a set of databases is generated, i.e. the results of the system (conditions of heavy labour-intensive tasks and the resulting decisions) are stored in order to use them for granted if the request comes in to solve an already known problem. Any further processing of the results is not presumed. It turns out that for solving a number of tasks using the stored results leads to significantly improving the system performance (speed, used memory, etc.).

The software system can be considered as a self-learning system through macro-operators. In some cases further processing (aggregation) of stored system performance is carried out. For example in the cases $L = 5$ and $GP = 5$, $L = 7$ and $GP = 3$, $L = 8$ and $GP = 3$, $L = 10$ and $GP = 2$, because of the huge number of combinations of generator polynomials of the convolutional encoders, respectively 28629151, 2048383, 16581375 and 1046529, in running the procedure "divide and search" the generation of databases from separate segments became necessary. For convolutional encoders with two registers with constraint length $L = [3 \;\; 3]$ and number of generator polynomials $GP = 3$ in running the procedure "divide and search" the formation of databases from separate segments became necessary.

The software system can be considered as a self-learning system by specifying the parameters using evaluating functions. The evaluating functions are combinations of values of appropriately chosen set of parameters; each parameter involved in estimating function has a corresponding weight. Such factors can be the initial state of the random integers' generator, the value of the signal-to-noise ratio, in the study of convolutional encoders and decoders in presence of noise by Module 2. In this case one can hardly speak of the application of any weights, at least not in the conventional sense.

The software system can be considered as a self-learning system by advices in which knowledge is acquired by the teacher (textbook, etc.). The relevant

training subsystem transforms this knowledge in a form that is usable by the processing subsystem. In other words, the teacher selects contents, structure and presentation of knowledge that he/she wants to add to the existing knowledge of the system and training subsystem has the task of syntactic transformation of the knowledge obtained from the teacher in a way that is available to the processing (using knowledge) module. All interactive learning modules are provided with information from the theory of digital communication systems, convolutional encoders and decoders, ways to represent the convolutional encoders and applications of the convolutional encoders in the field of telecommunications. This knowledge is created in the form of images by the teacher.

The machine learning techniques and their impact on convolutional encoders simulation and study are presented in Figure 4.

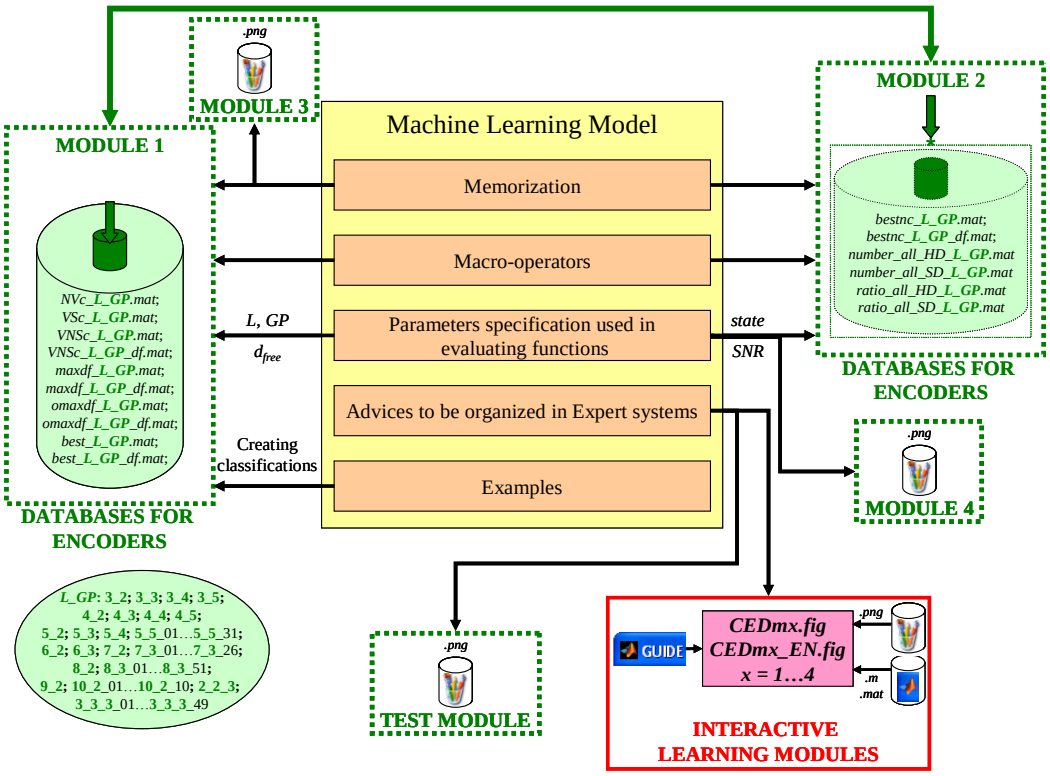

Figure 4. Machine learning techniques and their impact on convolutional encoders simulation and study

4 CONCLUSIONS

In the context of machine learning, the implemented software system may be considered as a self-learning system: 1) by memorization; 2) through macro-operators; 3) by specifying the parameters using evaluating functions; 4) by advices in which knowledge is acquired by the teacher.

As a result of the operations of Module 1 and Module 2 a set of databases is generated, i.e. the results of the system (conditions of heavy labour-intensive tasks and the resulting decisions) are stored in order to use them for granted if the request comes in to solve an already known problem. It turns out that for solving a number of tasks using stored results leads to significantly improving the system performance (speed, used memory, etc.).

ACKNOWLEDGEMENTS

The present paper has been produced with the financial assistance of the European Social Fund under Operational Programme “Human Resources Development”. The contents of this document are the sole responsibility of the University of Ruse and

can under no circumstances be regarded as reflecting the position of the European Union or the Ministry of Education and Science of Republic of Bulgaria. Project № BG051PO001-3.3.06-0008 "Supporting Academic Development of Scientific Personnel in Engineering and Information Science and Technologies".

REFERENCES

Fikes, R., 1971. *Monitored Execution of Robot Plans Produced by STRIPS*, http://www.ai.sri.com/ pubs/ files/tn055-fikes71.pdf.

Samuel, A.L., 2000. *Some studies in machine learning using the game of checkers*. In IBM Journal of Research and Development, Volume 44, Issue 1.2, pp. 206 – 226.

Buchanan, B.G. and Shortliffe, E.H. 1984 *Rule-Based Expert Systems: The MYCIN Experiments of the Stanford Heuristic Programming Project. Reading, MA*: Addison-Wesley, http:// aaai.org/ AITopics/ RuleBasedExpertSystems.

Blahut, R.E., 1983. *Theory and Practice of Error Control Codes.* Addison-Wesley.

TRIFID CIPHER IMPLEMENTATION IN MATLAB FOR LATIN AND CYRILLIC TEXTS

Adriana Borodzhieva
Faculty of Electrical Engineering, Electronics and Automation, Telecommunications Department, University of Ruse, 8 Studentska Street, Ruse, Bulgaria
aborodjieva@ecs.uni-ruse.bg

Tzvetomir Vassilev, Stanislav Kostadinov, and Plamen Manoilov
Faculty of Natural Sciences and Education, Department of Informatics and Information Technologies, University of Ruse, 8 Studentska Street, Ruse, Bulgaria
tvassilev@uni-ruse.bg, sdkostadinov@uni-ruse.bg, pmanoilov@ecs.uni-ruse.bg

Galia Marinova
Telecommunications Faculty, Technical University of Sofia, 8 Kl. Ohridski Blvd., Sofia, Bulgaria
gim@tu-sofia.bg

Keywords: Cryptography, Classical ciphers, Trifid Ciphers, MATLAB.

Abstract: In classical cryptography, the trifid cipher is a cipher invented around 1901 by Felix Delastelle, which extends the concept of the bifid cipher to a third dimension, allowing each symbol to be fractionated into 3 elements instead of two. The trifid turns them into coordinates on a $3 \times 3 \times 3$ cube. As with the bifid, this is then combined with transposition to achieve diffusion. Thus the trifid cipher was the first practical trigraphic substitution. The paper describes the algorithm and MATLAB-based software tool implementing encryption and decryption of Latin and Cyrillic texts using trifid ciphers. The tool will be used in the course "Telecommunication Security" by students of the specialty "Telecommunication Systems" for Bachelor degree at University of Ruse.

1 INTRODUCTION

The development of information and communication technology is the dominant factor for the sustainable development of society. Problems of information security are of fundamental importance not only for society and the state, but for the individual himself. To achieve the required levels of security of the information a highly qualified personnel is increasingly needed. In this regard increased attention is paid to the training of specialists in this field, based on the continuous improvement of the educational process (Sarkisyan, 2011).

This paper presents a software tool, implemented as MATLAB scripts, for the encryption and decryption of texts in English (Latin alphabet) and Bulgarian/Russian (Cyrillic alphabet) using a trifid cipher. The purpose is to illustrate the processes of encryption and decryption. The software tool is designed for the course "Telecommunication security" for undergraduate students in "Telecommunication Systems". It can be used in any other course on cryptographic methods. Initially images appear in separate graphics windows in order to explain the theory. Screen shots of running examples of encryption/decryption of texts in English and Bulgarian/Russian are attached.

2 ENCRYPTING TEXTS IN ENGLISH USING TRIFID CIPHER

A trifid cipher is similar to the bifid cipher, but it does not only record the numbers of the row and column, but also the layer in which the relevant letter is located. Three matrices of dimension 3×3 are used and by specifying a keyword without

repetition, the letters of the word are determined sequentially line by line. After them alphabetically the remaining letters of the alphabet that are not included in the composition of the keyword are added. The matrices contain a total of 27 cells and therefore another character (*dot*) is added (Wikipedia-Trifid cipher, 2014), (Codes and Ciphers, 2014), (Practical cryptography, 2014), (Dickason-Trifid cipher, 2014).

When the script is run, an image is displayed in a separate graphics window (Figure 1) that illustrates the process of encryption/decryption. The matrices contain the letters of the alphabet, arranged in alphabetical order. Below the matrices the plain-text "TRIFID" is written, and below it is the corresponding cipher-text "VAIQRY". Encryption using trifid cipher is carried out as follows. Under each letter of the plain-text the corresponding layer, row and column in which it is located in the matrices are written. Then the numbers of the layer, row and column are read by rows and grouped in triplets; the first digit is taken as a layer, the second – as a row, and the last one – as a column. Each triplet is replaced by the letter, which is located in the matrix at the corresponding coordinates.

The encryption process begins with the selection of a keyword. It is used to create the matrices needed to implement the encryption. The selection is done by menu which contains fourteen keywords. Figure 2 shows the matrices of the keyword CIPHER. The letters in bold are the letters of the keyword. Then the remaining letters of the English alphabet are completed.

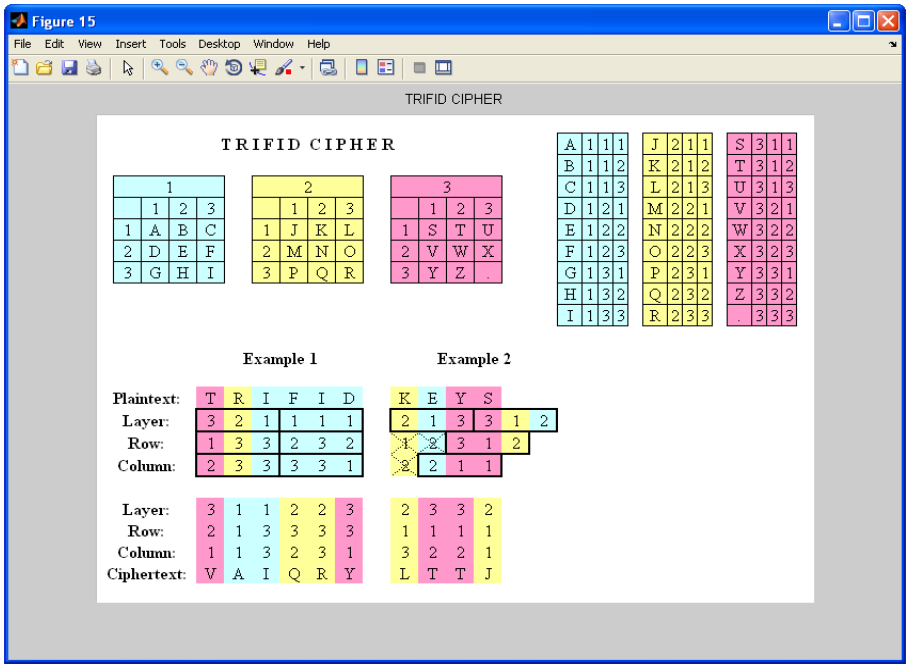

Figure 1. Illustration of encryption/decryption of English text using trifid ciphers

The algorithm for encryption of English texts using trifid cipher implemented in the developed script contains the following steps:

1. Select a keyword to compile the matrices. The generated matrices are stored in the variable *MA*.

2. Enter the plain-text in English from the keyboard with the possibility of spaces between words; the plain-text is stored in the variable *s*.

3. Find the positions of spaces in *s*. These positions are stored in a vector-row *k* (first, *k* = [ ]). This operation is realized using a loop with relation to the variable *i* = 1:*length*(*s*), where *length*(*s*) is the length of the string *s*. Here, if *s*(*i*) = ' ' (space), then *k* = [*k i*].

4. Eliminate spaces in the string *s*. For storing the intermediate results, the variable *str* is used (first, *str* = [' ']). Later the string *s* without spaces is stored in the variable *str* using the following operators: *str* = *strcat*(*str*,*s*(1:*k*(1))), *str* = *strcat*(*str*,*s*((*k*(*i*)+1):(*k*(*i*+1)-1))) for *i* = 1:*length*(*k*)-1, where *k* is the vector-row with the positions of the spaces in the string *s*; *s* = *strcat*(*str*,*s*((*k*(*length*(*k*))+1):*length*(*s*))).

5. Convert the lower case letters, if any, to upper case letters.

6. Encrypt the processed text. For each character, determine the layer *la*, the row *ra* and the column *ca*, which contain the *i*-th character of the string in the matrix *MA* using the operator *find*. Then the following variables are created: *l* = [*l la*]; *r* = [*r ra*]; *c* = [*c ca*]; *v* = [*l r c*]. The encryption of the plain-text is realized for each *i* = 1:3:3**length*(*s*)-2 with the lines: *la_n* = *v*(*i*); *ra_n* = *v*(*i*+1); *ca_n* = *v*(*i*+2); *lc* = [*lc la_n*]; *rc* = [*rc ra_n*]; *cc* = [*cc ca_n*]. Here, *la_n*, *ra_n* and *ca_n* are the coordinates (the layer, the row and the column) of the first symbol in the encrypted text. The encrypted characters are located in these layer, row and column. Then the encrypted text is obtained using the lines:

scr = *strcat*(*scr*,*L*1(*rc*(*i*),*cc*(*i*))), where *lc* = 1;

scr = *strcat*(*scr*,*L*2(*rc*(*i*),*cc*(*i*))), where *lc* = 2;

scr = *strcat*(*scr*,*L*3(*rc*(*i*),*cc*(*i*))), where *lc* = 3;

For storing the intermediate results, the variable *scr* is used.

7. Display the encrypted text stored in the string variable *scr*.

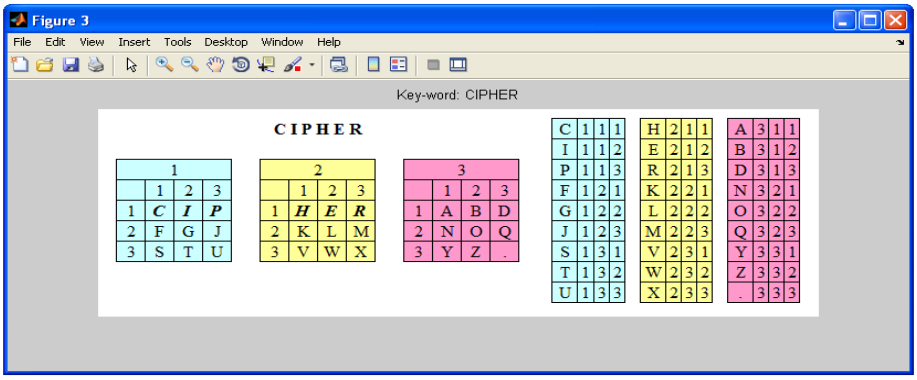

Figure 2. Matrices for the keyword “CIPHER”

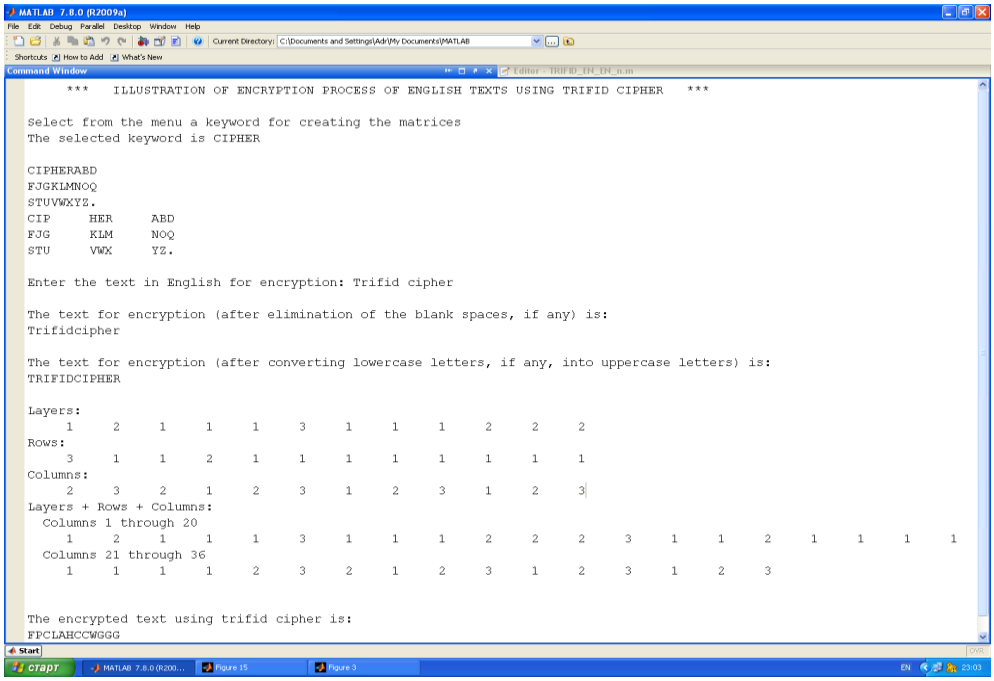

Figure 3. Encryption of English text using trifid cipher Keyword: CIPHER, Plain-text: Trifid cipher; Cipher-text: FPCLAHCCWGGG

Figure 3 illustrates the process of encrypting an English text.

The keyword CIPHER was chosen. The text to encrypt entered by the user is the English text “Trifid cipher”. It was processed according to the algorithm described.

The following results are obtained:

The text for encryption (after elimination of empty spaces) is: Trifidcipher.

The text for encryption (after converting lowercase to uppercase) is: TRIFIDCIPHER.

The encrypted text is: FPCLAHCCWGGG.

3 ENCRYPTING TEXTS IN CYRILLIC (BULGARIAN/RUSSIAN) USING TRIFID CIPHER

3.1 Generation of Matrices for Encryption of Texts in Cyrillic

A research was performed which has shown that the selection of four matrices of size 4 x 4 is more suitable for texts in Cyrillic than three matrices of size 4 x 4 or three matrices of size 4 x 3 (although the cells would be sufficient for fitting the letters of the Bulgarian alphabet).

Option 1: As the Bulgarian alphabet consists of 30 letters, in order to build matrices for the trifid cipher a row (or column) must be added to each matrix.

In an attempt to encrypt the word ШИФЪР (cipher) using a trifid cipher with a matrix to which an additional fourth row was added, based on keyword КРИПТОГРАФИЯ (cryptography), the following results are obtained, Figure 4.

1			
	1	2	3
1	К	Р	И
2	Я	Б	В
3	М	Н	С
4	Ъ	Ь	Ю

2			
	1	2	3
1	П	Т	О
2	Д	Е	Ж
3	У	Х	Ц
4	.	,	-

3			
	1	2	3
1	Г	А	Ф
2	З	Й	Л
3	Ч	Ш	Щ
4	/	!	?

Ш	И	Ф	Ъ	Р
3	1	3	1	1
3	1	1	4	1
2	3	3	1	2
3	1	1	1	3
1	1	1	2	1
3	3	4	3	2
Ш	И	[redacted]	В	А

Figure 4. Matrices with added extra fourth row

Each letter of the plain-text is written with the numbers of layer, row and column in which it is located. Then these numbers are recorded in one row and are grouped in threes, as the first digit corresponds to the number of the layer, the second one – the number of the row, and the third one – the number of the column: 3131131**4**123312. The new sequence of digits shows that a fourth column is required, which in this case is absent. In this situation it is necessary to add an additional fourth column in each of the matrices. As shown in Figure 5 it contains the digits from 1 to 9, together with the symbols ":" and ";". Another option was studied to determine whether the added extra fourth column is sufficient.

1				
	1	2	3	4
1	К	Р	И	0
2	Я	Б	В	1
3	М	Н	С	2
4	Ъ	Ь	Ю	3

2				
	1	2	3	4
1	П	Т	О	4
2	Д	Е	Ж	5
3	У	Х	Ц	6
4	.	,	-	7

3				
	1	2	3	4
1	Г	А	Ф	8
2	З	Й	Л	9
3	Ч	Ш	Щ	:
4	/	!	?	;

Figure 5. Matrices with fourth column extra added

Option 2: The attempt to encrypt the number 2013 with trifid cipher matrix based on the keyword КРИПТОГРАФИЯ (cryptography) yields the result in Figure 6.

The encryption method is the same. In this case, it is obvious that a fourth layer is needed, which in this case is not available.

The above examples demonstrate that the implementation of a trifid cipher for texts in Bulgarian needs four matrices of size 4 x 4, which requires 4 x 4 x 4 = 64 characters. This significantly exceeds the number of letters in the Bulgarian alphabet. Therefore two typical letters “Ы and Э” in Russian, decimal digits, and many other characters were added, which allows to encrypt/decrypt text with different symbols.

2	0	1	3
1	1	1	1
3	1	2	4
4	4	4	4
1	1	2	4
1	3	4	4
1	1	4	4
К	М	7	[redacted]

Figure 6. Application of trifid cipher in 4 rows, 4 columns and 3 layers

3.2 Encrypting Texts in Bulgarian/ Russian Using Trifid Cifer

Figure 7 shows the four matrices of size 4 x 4, filled with the characters of the Cyrillic alphabet without using a keyword.

The matrices contain a total of 64 cells – the number of rows, columns and layers must be the same. This allows adding more characters: punctuation, numbers from 0 to 9, plus, minus, signs for multiplication and division, and Ы, Э, &, ^, ~, (,), %, $, €. In this way the matrices cover all languages using the Cyrillic alphabet for their writing. Under the matrices the plain-text ШИФРОГРАМА (cipher-text) is written. The cipher-text is: "9/ГРФРАА(А".

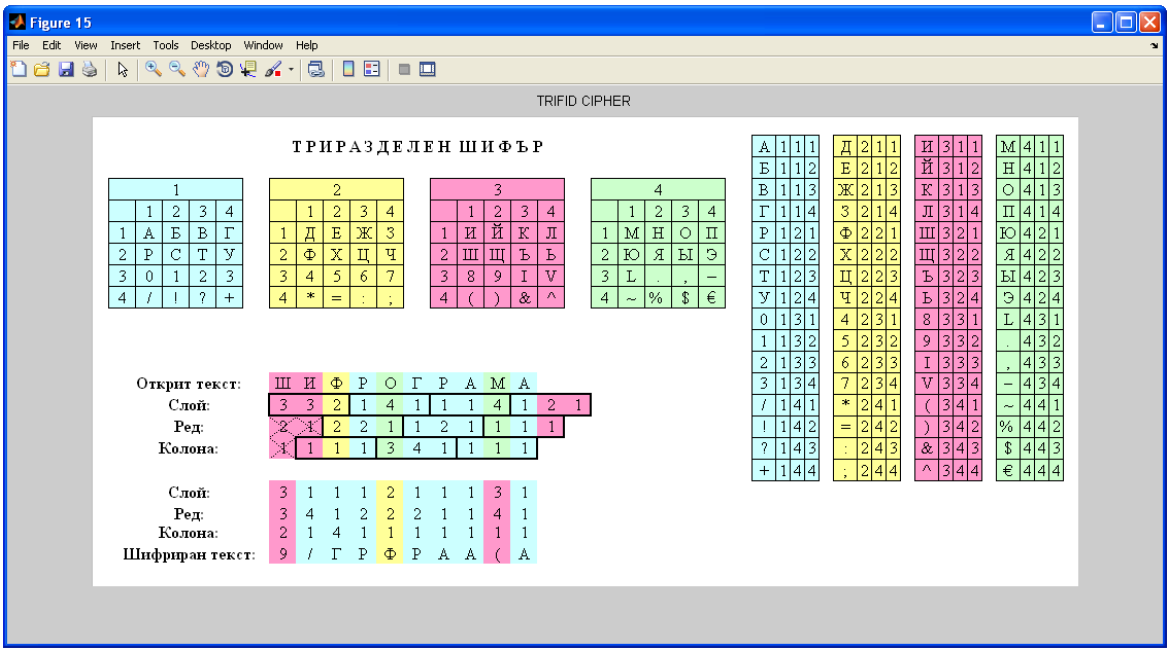

Figure 7. Illustration of encryption/decryption of text of texts in Bulgarian/Russian with no keyword using trifid ciphers

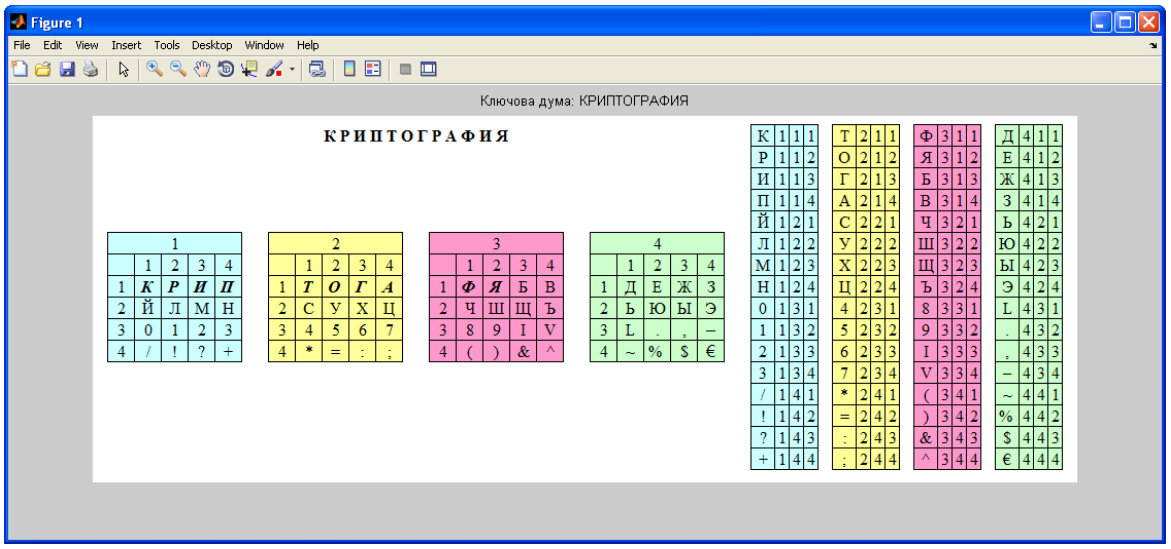

Figure 8. Matrices for encryption of texts in Bulgarian/Russian with keyword КРИПТОГРАФИЯ (cryptography)

The resulting matrices when using a keyword are given in Figure 8. When using a keyword the characters of the keyword are filled in sequentially (row by row) without repetition. Then the remaining letters of the Bulgarian alphabet that do not belong to the keyword are added in alphabetical order.

Figure 9 illustrates the process of encryption of Bulgarian/Russian texts using trifid cipher. The plain-text contains a mathematical expression.

The user enters the plain-text for encryption: 2013 * 3 = 6039.

The encrypted text is КЙС2IVI8*Щ!

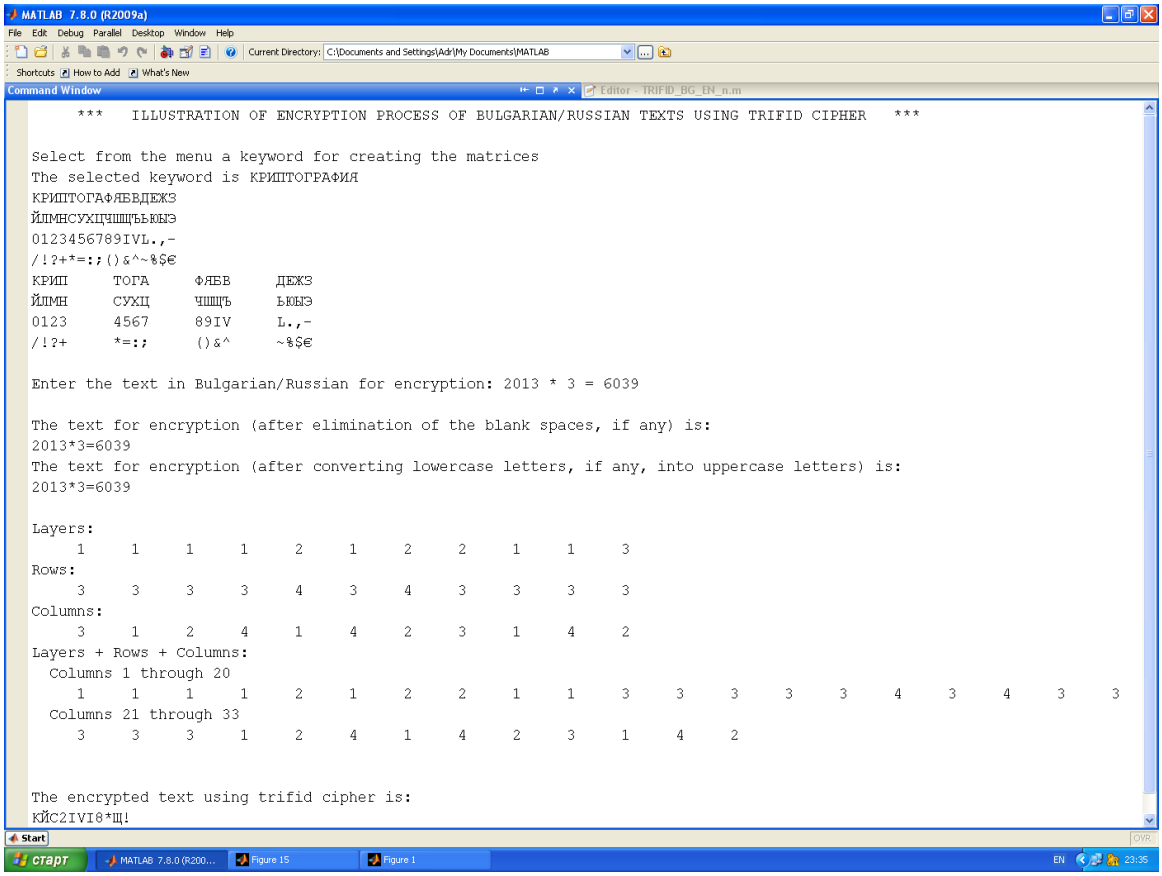

Figure 9. Encryption of Bulgarian/Russian texts using trifid cipher (encryption of a sentence) Keyword: КРИПТОАНАЛИЗ (cryptanalysis), Plain-text: 2013 * 3 = 6039; Cipher-text: КЙС2IVI8*Щ!

4 DECRYPTING ENGLISH AND CYRILLIC TEXTS USING TRIFID CIPHER

The algorithm for decrypting English or Cyrillic texts using trifid cipher implemented in the developed MATLAB script comprises the following steps:

1. Select the keyword from the menu to compile the matrices.
2. Enter the cipher-text from the keyboard with the possibility of blank spaces between the words.
3. Find the positions of spaces.
4. Eliminate spaces.
5. Convert the lower case letters, if any, to upper case letters.
6. Decrypt the processed text.
7. Display the decrypted text.
8. The developed application for decrypting texts allows the user to specify the positions of the empty spaces.

Figure 10 illustrates the process of decrypting English text with the keyword “CIPHER”. The cipher-text is “FPC LAHCC WGGG” with randomly inserted spaces. The figure shows how the spaces between the words have been eliminated. The developed application for decryption of texts allows

the user to specify the position of the spaces between the words. After insertion of spaces the decrypted text becomes: TRIFID CIPHER (Figure 10, the last row).

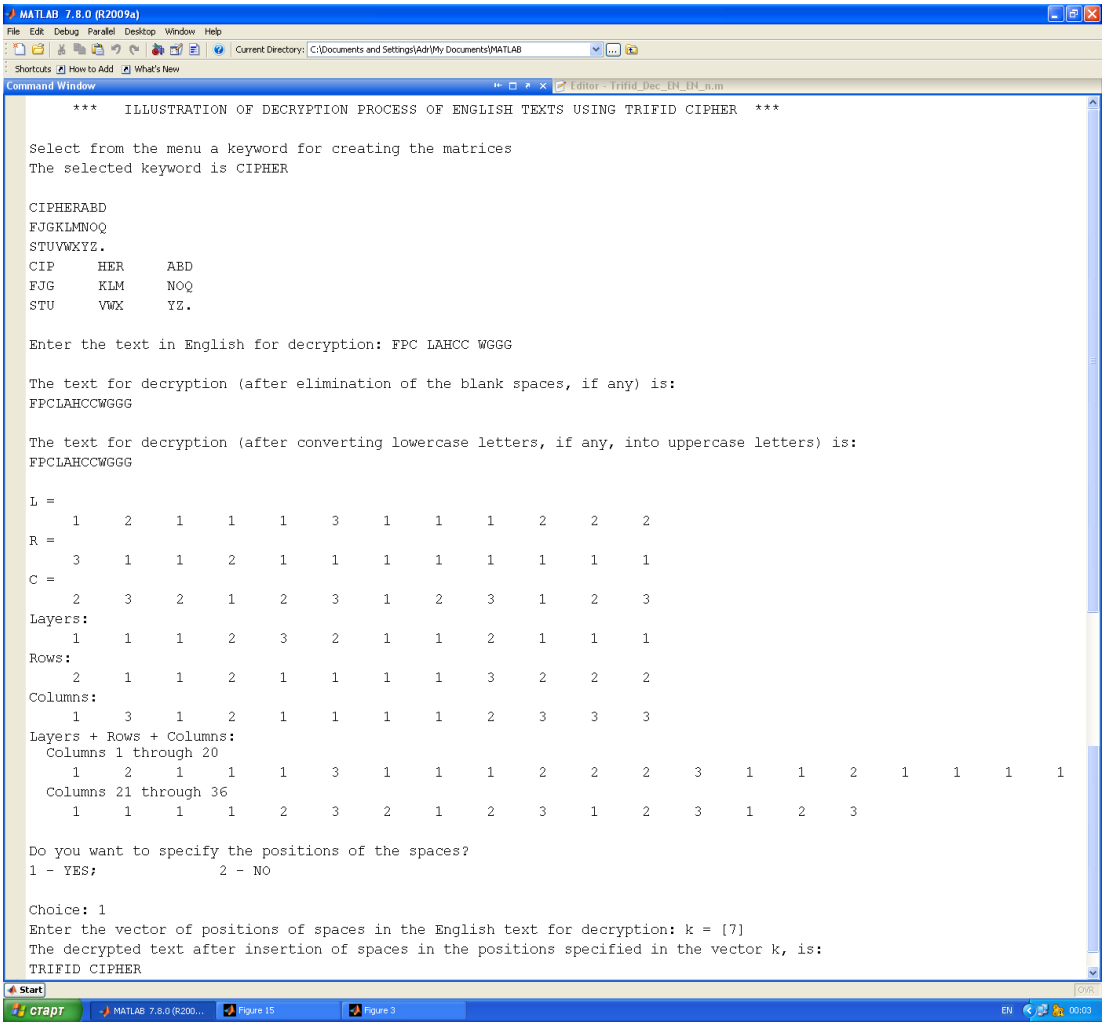

Figure 10. Decryption of English texts using trifid cipher (decrypting more than one word) Keyword: CIPHER, Cipher-text: FPC LAHCC WGGG; Decrypted text: TRIFID CIPHER

5 CONCLUSIONS

The main contribution of this paper is the implementation of a trifid cipher for Cyrillic texts. The following has been achieved:

1. Analysis has been performed and it was proven that when using a trifid cipher the number of layers, rows and columns must be equal.

2. A trifid cipher was implemented for all languages using the Cyrillic alphabet for their writing.

In the future the user interface can be extended.

It will be interesting to implement a trifid cipher for texts including both English and Cyrillic characters. It is possible to do this with 4 matrices of 16 characters each, as the number of characters needed is 26 + 32 = 58, however it will not be possible to encrypt numbers.

Therefore it will be better to implement a trifid cipher for Latin and Cyrillic with five matrices of size 5 x 5, which requires 5 x 5 x 5 = 125 characters.

This significantly exceeds the number of cells. Therefore two typical letters “Ы and Э” in Russian, decimal digits, and many other characters were added, which allows to encrypt/decrypt text with different symbols. Figure 11 shows the five matrices of size 5 x 5, filled with the characters of the Latin and Cyrillic alphabet without using keywords. The matrices contain a total of 125 cells. This allows adding more characters: punctuation, numbers from 0 to 9, plus, minus, signs for multiplication and division, and Ы, Э, &, ^, ~, (,), %, $, €. In this way the matrices cover all languages using the Latin and Cyrillic alphabet. Some Greek symbols used in Mathematics and Electrical Engineering are inserted into these matrices.

1

	1	2	3	4	5
1	А	Б	В	Г	Д
2	Щ	Ъ	Ь	Ю	Я
3	I	J	K	L	M
4	(	)	[	]	{
5	⊥	§	±	¯	

2

	1	2	3	4	5
1	Е	Ж	З	И	Й
2	Ы	Э	0	1	2
3	N	O	P	Q	R
4	}	<	>	≤	≥
5	∞	÷	⇒	Δ	Σ

3

	1	2	3	4	5
1	К	Л	М	Н	О
2	3	4	5	6	7
3	S	T	U	V	W
4	%	&	:	;	"
5	Ω	α	β	γ	δ

4

	1	2	3	4	5
1	П	Р	С	Т	У
2	8	9	A	B	C
3	X	Y	Z	+	–
4	!	?	@	_	°
5	λ	μ	φ	π	ρ

5

	1	2	3	4	5
1	Ф	Х	Ц	Ч	Ш
2	D	E	F	G	H
3	*	/	^	.	,
4	⊕	∀	≅	≡	~
5	σ	ω	∈	∉	∂

Figure 11. Five matrices of size 5 x 5, filled with the characters of the Latin and Cyrillic alphabet, punctuation, Greek symbols and symbols used for mathematical expressions

ACKNOWLEDGEMENTS

The present paper has been produced with the financial assistance of the European Social Fund under Operational Programme “Human Resources Development”. The contents of this document are the sole responsibility of the University of Ruse and can under no circumstances be regarded as reflecting the position of the European Union or the Ministry of Education and Science of Republic of Bulgaria. Project № BG051PO001-3.3.06-0008 “Supporting Academic Development of Scientific Personnel in Engineering and Information Science and Technologies”.

REFERENCES

Sarkisyan, A. Training of Bulgarian graduates in Information Security, "Dialogue", vol. 3, 2011 (in Bulgarian).

Wikipedia. Trifid cipher. Visited 2014. http://en.wikipedia.org/wiki/Trifid_cipher

Codes and Ciphers :: Trifid Cipher. Visited 2014. http://www.braingle.com/brainteasers/codes/trifid.php

Practical cryptography. Trifid Cipher. Visited 2014. http://practicalcryptography.com/ciphers/trifid-cipher/

Trifid Cipher. Visited 2014. http://www.dickason.com/caching/OHMIKYtrifid.html

Author Index

Author Index

Proceedings of ISRSSP 2014
Fourth International Symposium on Radio Systems and Space Plasma
ISBN: 978-619-90124-2-0
http://www.isrssp.org